# Deformation Behaviour of TiNi Shape Memory Alloy under Tensile and Compressive Loads

by

Meisam Shahirnia

Submitted in partial fulfillment of the requirements

for the degree of Master of Applied Science

at

Dalhousie University

Halifax, Nova Scotia

June 2011

# DALHOUSIE UNIVERSITY

DEPARTMENT OF PROCESS ENGINEERING AND APPLIED SCIENCE

The undersigned hereby certify that they have read and recommend to the Faculty of Graduate Studies for acceptance a thesis entitled “Deformation Behaviour of TiNi Shape Memory Alloy under Tensile and Compressive Loads” by Meisam Shahirnia in partial fulfillment of the requirements for the degree of Master of Applied Science.

Dated: 17/06/2011

Supervisor: _____

Readers: _____

_____

# DALHOUSIE UNIVERSITY

DATE: 17/06/2011

**AUTHOR:** Meisam Shahirnia

**TITLE:** Deformation Behaviour of TiNi Shape Memory Alloy under Tensile and Compressive Loads

**DEPARTMENT OR SCHOOL:** Department of Process Engineering and Applied Science

**DEGREE:** MASc **CONVOCATION:** October **YEAR:** 2011



_____

Meisam Shahirnia

I dedicated this thesis to

my parents and my sister. Without their patience, understanding, support, and most of all love, the completion of this work would not have been possible.

Table of Contents

*List of Tables*.....*vii*

*List of Figures*..... *viii*

*Acknowledgements*.....*xii*

*Abstract*..... *xiii*

*List of Abbreviations and Symbol Used*.....*xiv*

*CHAPTER 1 INTRODUCTION*.....*1*

Overview and Objectives.....*1*

*CHAPTER 2 LITERATURE REVIEW*.....*3*

2.1 TiNi Shape Memory Alloys.....3

2.2 Phase Diagram of TiNi Alloys.....4

2.3 Phases and Precipitation in TiNi Alloys.....5

2.3.1 Austenite..... 6

2.3.2 Martensite..... 6

2.3.3 R-Phase..... 7

2.3.4 Precipitates..... 8

2.4 Transformation in TiNi Alloys.....9

2.4.1 Martensitic Phase Transformation Temperatures..... 11

2.4.2 Determination of Transformation Temperatures..... 12

2.4.3 Effects of Aging Treatment on Transformation Temperatures..... 15

2.5 Deformation Behaviour of TiNi Alloys.....17

2.5.1 Shape Memory Effect..... 18

2.5.2 Superelastic or Pseudo-Elastic Effect..... 21

2.5.3 Stress- Strain Curves as a Function of Operating Temperature..... 22

2.6 Factors Affecting TiNi Properties.....26

2.6.1 Strain Rate..... 26

2.6.2 Material History..... 29

2.6.3 Cold Work..... 30

2.7 Indentation Behaviour of TiNi Shape Memory Alloys ..... 31
2.7.1 Sink-in and Pile-up Phenomena in Indentation ..... 34
*CHAPTER 3 EXPERIMENTAL METHODS ..... 37*
3.1 Tensile Tests ..... 37
3.1.1 Materials ..... 37
3.1.2 Differential scanning calorimetry ..... 38
3.1.3 Tensile Tests Conditions ..... 38
3.2 Indentation Tests ..... 40
3.2.1 Materials ..... 40
3.2.2 X-Ray Diffraction ..... 41
3.2.3 Optical Microscopy ..... 42
3.2.4 Indentation Tests Conditions ..... 42
*CHAPTER 4 RESULTS AND DISCUSSION ..... 46*
4.1 Tensile Tests ..... 46
4.1.1 Materials Assessment ..... 46
4.1.2 Stress – Strain Curves ..... 48
4.1.3 Simultaneous Heating and Loading during Tensile Tests ..... 55
4.2 Indentation Tests ..... 63
4.2.1 Materials Assessment ..... 63
4.2.2 Spherical Indenter ..... 66
4.2.3 Sharp Indenter ..... 80
*CHAPTER 5 CONCLUSIONS ..... 92*
*References ..... 95*
*Appendix A: Raw Data ..... 103*

## List of Tables

Table 3.1 - Chemical composition of superelastic and shape memory TiNi (wt%) ..... 37

Table 3.2 - Chemicalcompositions of superelastic TiNi indentation specimens (wt. %) ..... 40

Table 3.3 - Indentation tests conditions ..... 45

Table 4.1 - Transformation temperatures of TiNi tensile specimens ..... 48

Table 4.2 - Mechanical properties of superelastic TiNi alloy ..... 49

Table 4.3 - Mechanical properties of shape memory TiNi alloy ..... 52

Table 4.4 - Transformation temperatures of superelastic TiNi indentation ..... 64

## List of Figures

Figure 2.1 - Phase diagram of TiNi ..... 5

Figure 2.2 - Crystal structure of TiNi B2 cubic unit cell [25] ..... 6

Figure 2.3 - Crystal structure of TiNi B19', monoclinic unit cell [24]..... 7

Figure 2.4 -Crystal structure of TiNi R-phase trigonal unit cell [26] ..... 8

Figure 2.5 - TTT diagram of Ti -52 % Ni [24] ..... 9

Figure 2.6 -Three martensitic transformation paths in TiNi alloys [24]..... 10

Figure 2.7 - Physical properties versus temperature for martensitic transformation [33] 11

Figure 2.8 - Electrical resistance changes during phase transformation in Ti-50.1%Ni, aging at 673K for 1hr after solution treatment in 273k [17]. ..... 12

Figure 2.9 - Determination of the transformation temperatures from DSC diagram [36].....14

Figure 2.10 - Illustration of the formation of the R-phase peak in a DSC diagram.....14

Figure 2.11 - TiNi phase diagram [24] ..... 16

Figure 2.12 - Effect of aging time on transformation temperatures of TiNi alloys [24] .. 17

Figure 2.13 - Forward and reverse transformations in TiNi without mechanical loading [1]..... 18

Figure 2.15 - Schematic of the shape memory effect in TiNi alloy [1] ..... 19

Figure 2.14 - Schematic of the detwinning process under stress [1] ..... 19

Figure 2.16 - Forward and reverse transformation under applied mechanical load [1].... 21

Figure 2.17 - Schematic of the superelastic effect in TiNi alloy [1]..... 22

Figure 2.18 - Shape memory and superelasticity regions in stress vs. temperature diagram [24]..... 23

Figure 2.19 - Stress-strain curves of TiNi alloy at different operating temperature ..... 24

Figure 2.20 - (a) Stress-strain curve in superelastic regime, (b) temperature-strain curve in shape memory regime [1] ..... 25

Figure 2.21 - Engineering stress-strain curves of Ni-rich TiNi alloy at different strain rates at ambient temperature [43]. ..... 27

Figure 2.22 - Stress-strain curves of TiNi shape memory alloy at different strain rates and temperatures under compression and tension, a)-196 °C, b) 0°C, c) 200°C, d) 400 °C [44] ..... 29

Figure 2.23- The enclosed area to load vs. depth curve for calculating $W_t$ and $W_{rc}$[76].. 33

Figure 2.24 - The contact area of the spherical indenter and the specimen surface [79].. 35

Figure 2.25 - Cross-sectional view of the indent during heating at different temperatures [80] ..... 36

Figure 3.1 - Miniature tensile tester ..... 39

Figure 3.2 - Bruker D8 Advance XRD system ..... 41

Figure 3.3 - XRD diffractometer ..... 42

Figure 3.4 - (a) Universal Micro-Tribometer, (b) chamber, load sensor and indenter ..... 44

Figure 4.1 - DSC spectrogram of (a) superelastic and (b) shape memory TiNi ..... 47

Figure 4.2 - Stress-strain curves at three different temperatures for superelastic TiNi .... 49

Figure 4.3 - Stress-strain curves at three different temperatures for shape memory TiNi ..... 51

Figure 4.4 - Cyclic stress – strain curves of (a) superelastic and (b) shape memory TiNi alloy..... 53

Figure 4.5 - Transformation stress as a function of temperature curve of superelastic TiNi alloy..... 54

Figure 4.6 - Effect of heating superelastic sample in the plateau stress region ..... 55

Figure 4.7 - In-situ stress-strain curve of superelastic TiNi interrupted by heating/cooling periods ..... 56

Figure 4.8 - Optical microscopy images of the microstructural evolution of superelastic TiNi during tensile testing while subjected to heating and cooling periods. ..... 57

Figure 4.9 - Nucleation of different martensite bands in random regions at a 45$^{o}$ angle from the tensile axis ..... 60

Figure 4.10 - In-situ stress-strain curve of shape memory TiNi interrupted by heating/cooling periods ..... 61

Figure 4.11 - Optical microscopy images of microstructural evolution of shape memory TiNi during tensile testing while subjected to heating and cooling periods. ..... 62

Figure 4.12 - In-situ stress-strain curve of brass interrupted by heating/cooling periods ..... 63

Figure 4.13 - DSC spectrogram of superelastic TiNi indentation sample ..... 64

Figure 4.14 - XRD pattern of superelastic TiNi ..... 65

Figure 4.15 - Microstructure of as-received superelastic TiNi ..... 66

Figure 4.16 - Loading - unloading curves of superelastic TiNi under maximum load of 40 N, various temperature and load application of (a) 1N.min$^{-1}$, (b) 10 N.min$^{-1}$ ..... 68

Figure 4.17 - Loading - unloading curves of superelastic TiNi under maximum load of 60 N, various temperature and load application of (a) 1N.min$^{-1}$ ..... 69

Figure 4.18 - Loading - unloading curves of superelastic TiNi under maximum load of 80 N, various temperature and load application of (a) 1N.min$^{-1}$ and (b) 20 N.min$^{-1}$ ..... 71

Figure 4.19 - Loading - unloading curves of superelastic TiNi under maximum load of 80 N, various temperature and load application of (a) 10N.min$^{-1}$and (b) 20 N.min$^{-1}$ ..... 72

Figure 4.20 - Max load vs. max depth of indentation tests at low strain rate (loading rate of 1 N.min$^{-1}$) ..... 73

Figure 4.21 - Max load vs. max depth of indentation tests at medium strain rate (load rate of 10 N.min$^{-1}$) ..... 75

Figure 4.22 - Max load vs. max depth of indentation tests at high strain rate (load rate of 20 N.min$^{-1}$) ..... 75

Figure 4.23 - Max load vs. max depth diagram of superelastic TiNi at room temperature with different strain rates ..... 76

Figure 4.24 - Indentation tests results of AISI 304 steel at room temperature and different strain rates ..... 77

Figure 4.25 - Residual strain after unloading cycle, different strain rates, room temperature AISI 304 steel ..... 78

Figure 4.26 - Stress-strain curve from indentation tests at 25 $^{o}$C for superelastic TiNi ... 80

Figure 4.27 - (a) - Loading and unloading cycle of superelastic TiNi after indentation test under sharp indenter ..... 81

Figure 4.28 - Loading - unloading curves of superelastic TiNi under maximum load of 40 N, various temperatures and load application of (a) 1N.min$^{-1}$, (b) 10 N.min$^{-1}$ ..... 84

Figure 4.29 - Loading - unloading curves of superelastic TiNi under maximum load of 60 N, various temperatures and load application of (a) 1N.min$^{-1}$ ..... 85

Figure 4.30 - Loading - unloading curves of superelastic TiNi under maximum load of 80 N, various temperatures and load application of (a) 1N.min$^{-1}$ and (b)10 N.min$^{-1}$ ..... 87

Figure 4.31 - Loading - unloading curves of superelastic TiNi under maximum load of 100 N, various temperatures and load application of (a) 1 N.min$^{-1}$ ..... 88

Figure 4.32 - Max load vs. max depth, sharp indenter, (a) low strain rate (1N.min$^{-1}$) ..... 90

# Acknowledgements

The author would like to acknowledge the guidance, words of encouragement and unwavering support offered by Dr. Zoheir Farhat throughout the entirety of this project.

In addition, the author would like to thank the Natural Sciences and Engineering Research Council of Canada (NSERC) for its financial contributions. The efforts of Dr. George Jarjoura and Dr. Rob Jamieson are also greatly appreciated, as are the camaraderie and support of the materials engineering group at Dalhousie University, including Bradley Collier, Md. Aminul Islam and Aboulwahab Ibrahim, and the excellent technical advice and contributions offered by Mr. Dean Grijm and Mrs. Patricia Scallion.

Finally, the author would like to acknowledge the support of his family and friends, who have always been there for him throughout his academic career.

# Abstract

TiNi shape memory alloys (SMAs) have been extensively used in various applications. The great interest in TiNi alloys is due to its unique shape memory and superelasticity effects, along with its superior wear and dent resistance. Shape memory and superelastic effects are due to a reversible martensitic transformation that can be induced either thermally or mechanically. In this study, indentation tests at different temperatures, loads and strain rates have been performed on superelastic TiNi alloy. Deformation characteristics of superelastic TiNi under indentation have been compared to AISI 304 steel as a conventional material. Also, in-situ optical microscopy tests with interrupted heating have been employed in order to gain an insight into the coupled deformation and reversible martensitic transformation behaviour of TiNi SMAs under tensile loads. An understanding of the impacts of strain rate and temperature on the deformation behaviour of TiNi SMAs under localized compressive loads has been proposed.

# List of Abbreviations and Symbols Used

| **Symbols** | **Description** |
|---|---|
| SMA | Shape memory alloy |
| AISI | American iron and steel institute |
| SE | Superelasticity |
| SME | Shape memory effect |
| MEMS | Micro electromechanical systems |
| $A_s$ | Austenite start transformation temperature |
| $A_f$ | Austenite finish transformation temperature |
| $M_s$ | Martensite start transformation temperature |
| $M_f$ | Martensite finish transformation temperature |
| $R_s$ | R-phase start transformation temperature |
| $R_f$ | R-phase finish transformation temperature |
| $M^t$ | Twinned martensite |
| $M^d$ | Detwinned martensite |
| TTT | Time – temperature – transformation |
| DSC | Differential scanning calorimetry |
| $\sigma_s$ | Detwinning start stress |
| $\sigma_f$ | Detwinning finish stress |
| SIM | Stress induced martensite |
| $\sigma^{Ms}$ | Forward transformation start stress |
| $\sigma^{Mf}$ | Forward transformation finish stress |
| $\sigma^{As}$ | Reverse transformation start stress |
| $\sigma^{Af}$ | Reverse transformation finish stress |

| | |
|---|---|
| $M_d$ | Superelasticity limit temperature |
| $E_A$ | Austenite Young's module |
| $E_M$ | Martensite Young's module |
| SDE | Strength differential effect |
| $W_{rc}$ | Recoverable deformation energy |
| $W_t$ | Total deformation energy |
| $\eta$ | Recoverable energy / total deformation energy |
| L | Load |
| D | Depth |
| $h$ | Generated depth |
| $h_c$ | Specimen surface |
| XRD | X-ray diffraction |
| PDF | Powder diffraction file |
| ICDD | International centre for diffraction data |
| $F_z$ | Calibrated normal load |
| C | Indentation depth |
| UMT | Universal micro-tribometer |
| $\varepsilon_e$ | Recoverable strain |
| P | Compressive load of indentation |
| $\pi a^2$ | Contact area between indenter and the specimen |
| $a$ | Contact radius |
| $R^*$ | Effective radius of the specimen and indenter system |
| $R_s$ | Radius of the sample |
| $R_i$ | Radius of the indenter |

# CHAPTER 1 INTRODUCTION

## Overview and Objectives

Shape memory alloys (SMAs) as a distinctive class of metallic materials have been widely studied due to their unique characteristics, such as superelasticity and shape memory effect (SME). The applications of SMAs have covered a wide range of industries, namely, aerospace, automotive, biomedical, and oil exploration [1]. Numerous kinds of SMAs have been discovered in recent years; for instance, Fe-based alloys, TiNi, MnCu, CuAlNi, CuCd and CuZnAl have been reported to demonstrate superelastic and shape memory characteristics. Among all these SMAs, TiNi is found to exhibit the best mechanical properties and superior shape memory effect.

Superelastic TiNi alloy is becoming increasingly popular because of its unique properties, i.e. high strength, high damping capacity, excellent wear resistant and good corrosion resistance in addition to its excellent shape memory effect. It has been recently found that superelastic TiNi alloy has better tribological performance than many conventional wear resistant materials. The high wear resistance of TiNi alloy is attributable to a unique phenomenon, known as superelasticity or "pseudo-elasticity", resulting from a reversible martensitic transformation. Superelastic TiNi is currently being used in biomedical devices (such as artificial bone joints and orthodontic surgical tools) and micro electromechanical systems (MEMS) for its excellent wear resistance. Recently there has been an interest in using superelastic TiNi in bearings due to its high dent resistance during high impact.

Unlike conventional materials, superelastic TiNi undergoes a larger elastic recovery after deformation. That is, when a force is applied, the austenite phase (B2) transforms to pre-martensitic phase (R-phase) and then to a martensitic phase (B19'), accompanied by large deformation. As the load is removed, superelastic recovery as high as 10% takes place, which contributes significantly to dent and wear resistance.

Unfortunately, only limited fundamental research work on the deformation characteristics of TiNi alloys, especially under localized compressive load, has been reported in the open literatures. The objective of the present investigation is to carry out a comprehensive investigation on the effects of temperature and strain rate on deformation behaviour of TiNi SMAs under tensile and indentation loading. The study attempts to relate the deformation behaviour of TiNi SMAs to microstructural evolution during loading.

In order to achieve the objectives of this work, superelastic and shape memory TiNi alloys were prepared and investigated through a series of tensile and indentation tests at different temperatures and strain rates. Microstructural evolution during tensile testing was monitored and related to the deformation behaviour of TiNi SMAs.

The organizational outline of this thesis is as follows. A review of pertinent up to date background information on TiNi shape memory alloys, phase diagram and phase structures of TiNi, reversible martensitic transformation, superelastic and shape memory effects are provided in Chapter 2. Materials and experimental methods used to achieve the research objectives are outlined in detail in Chapter 3. Experimental results and relevant discussions are given in Chapter 4. Conclusions of this research and recommendations for future work are summarized in Chapter 5.

# CHAPTER 2 LITERATURE REVIEW

The extensive literature review in this chapter offers a comprehensive presentation of theories, fundamentals and mechanisms relevant to this study. Following a brief introduction of TiNi shape memory alloys, sections 2.2 and 2.3 will present phase diagrams and crystal structures of these alloys, while in section 2.4, reversible martensitic phase transformation will be reviewed. In the subsequent sections of the chapter, a general review of the deformation behaviour of TiNi alloys under tensile and indentation loads will be investigated and discussed.

## 2.1 TiNi Shape Memory Alloys

TiNi shape memory alloy was discovered by Buehler and his coworkers during an investigation into heat shielding materials. As the alloy was discovered in the Naval Ordnance Laboratory (NOL), the term "NiTiNOL" was given to it. NiTiNOL contains shape recovery properties that other conventional materials do not have, and so the term shape memory effect (SME) was coined to describe these properties [1].

Among all shape memory alloys, TiNi alloys have been the most widely used in various commercial and industrial applications due to their unique properties such as SME and superelasticity. The superelasticity and shape memory effect of TiNi are due to a reversible thermo-elastic martensitic transformation, where both stress and temperature have considerable effects on the martensitic transformation [2-5]. The martensitic transformation is also quite sensitive to the timing and sequence of thermo-mechanical loading cycles. Hence, many researchers have focused on the effects of the thermo-mechanical history of SMAs in order to elucidate the mechanism by which these phenomena take place [6-8].

In addition, their superior properties in wear [9,10] and corrosion resistance [11], mechanical properties, fatigue and ductility make TiNi alloys popular in various industries. Their high ductility and high mechanical damping have also attracted considerable attention in numerous applications [1,12-16]. The relatively low anisotropy

in the elastic behaviour of TiNi (especially at lower temperatures) and the easy transition of twin boundaries are the reasons for their high ductility and high mechanical damping, respectively. More recently, it has been found that, due to their pseudo-elasticity, TiNi SMAs have good tribological behaviour and superior wear resistance compared to other conventional wear-resistance materials such as steel and Ni- and Co-based alloys [17,18].

TiNi SMAs are widely used in various industries and environments such as automotive industries, energy conversion systems, electrical cable connectors, air conditioning vents, valves, etc. As well, several uses for TiNi alloys have been developed in biomedical applications due to their good biocompatibility, while the superior wear resistance of TiNi SMAs has led to the development of applications in micro electromechanical systems [19].

## 2.2 Phase Diagram of TiNi Alloys

The shape memory effect and superelasticity of TiNi has been observed in the equiatomic composition in the central region of the phase diagram, bounded by $TiNi_3$ and $Ti_2Ni$ phases. This region was first observed at high temperatures by Laves and Wallbaum [20]. Decomposition of TiNi into $TiNi_3$ and $Ti_2Ni$ was reported by Duwez and Taylor [21] at 650 ℃ and 800℃. According to the comprehensive investigations of Poole and Hume-Rothery [22], the solubility limit at high temperatures (above 900℃) was discovered. They observed a very steep boundary of Ti-rich close to 50% Ni; however, the solubility limit of Ni-rich dropped significantly upon lowering the temperature. They also verified the eutectoid decomposition of TiNi into $TiNi_3$ and $Ti_2Ni$, which had been previously reported by Duwez and Taylor. Moreover, the reversible transformation of TiNi into a phase called "$\pi$-phase" at lower temperatures (in which atomic diffusion can be prevented) was first discovered by Purdy and Parr in 1961 [23]. While this was the first observation of reversible martensitic transformation, the term "martensitic" was not used by this research team.

Over the course of three decades, numerous phase diagrams were established by investigators, with few common characteristics. One characteristic is the almost vertical boundary of the TiNi phase on the Ti-rich side, and the other is that the TiNi boundary on Ni-rich area dropped significantly with reducing the temperature. Eventually, a reliable phase diagram of a TiNi alloy was developed, as shown in Figure 2.1 [24].

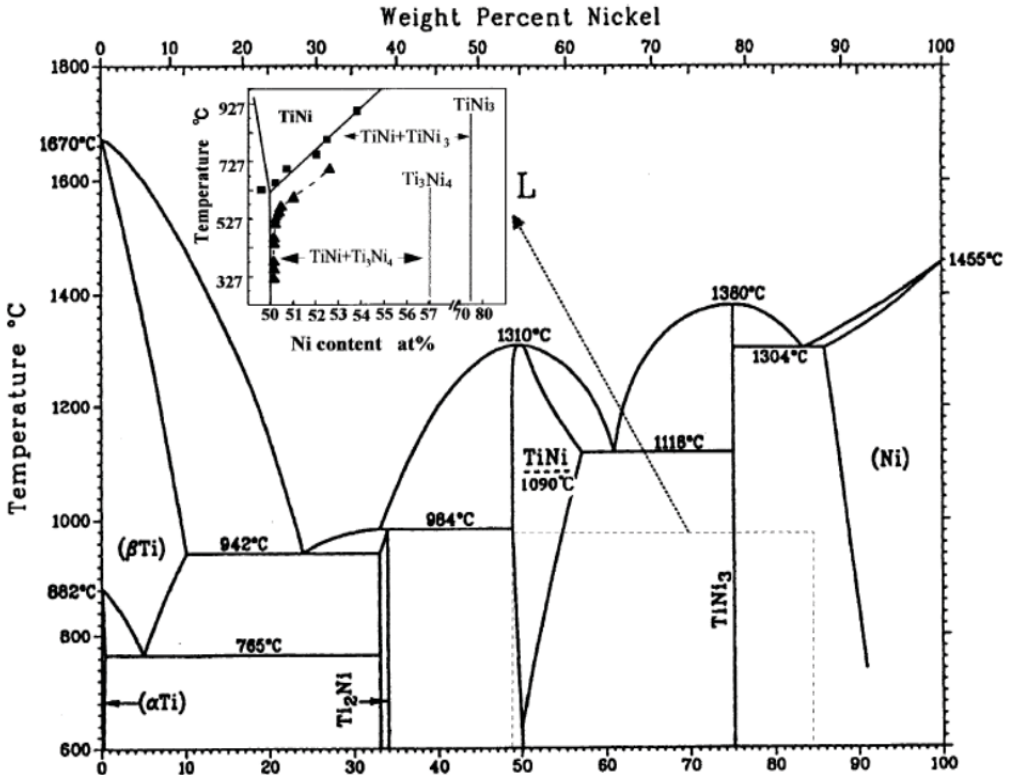


**Figure 2.1 - Phase diagram of TiNi**

## 2.3 Phases and Precipitation in TiNi Alloys

Austenite, martensite and R-phase are three different phases of TiNi which can be present under different conditions. Because all of the unique characteristics of TiNi alloys arise from the transformations between phases, a brief review of each phase and precipitations is given below.

### 2.3.1 Austenite

As shown in Figure 2.2, the austenite (parent phase) crystal structure is cubic ($B_2$ based on CsC1 structure), with a lattice constant of 0.3015 nm at room temperature. Austenite is a high temperature phase compared to martensite. This phase plays a vital role in superelastic and shape memory effects due to its essential role in the martensitic transformation [24].

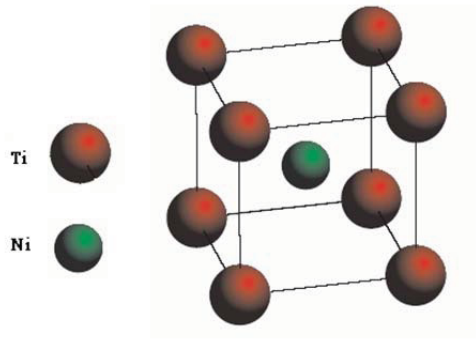


**Figure 2.2 - Crystal structure of TiNi B2 cubic unit cell [25]**

### 2.3.2 Martensite

When solution-treated austenite is plunged from a high temperature to below the martensite start temperature ($M_s$), a martensite phase (B19□) with a monoclinic crystal structure forms. B19' is a more stable martensite phase compared to an intermediate martensite phase (B19) with orthorhombic crystal structure, the latter of which forms under specific conditions prior to B19□ [24].

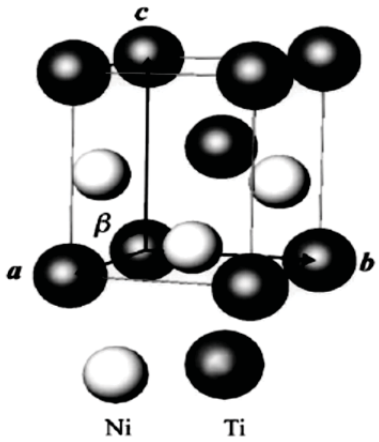


**Figure 2.3 - Crystal structure of TiNi B19', monoclinic unit cell [24]**

When martensite forms, different regions within crystals may have different orientation called variants. Martensite can be grouped into two categories according to their crystal variants. The first type is the twinned martensite ($M^t$), which forms by a mixture of "self-accommodated" variants. The second type is the detwinned martensite ($M^d$), where different variants are reoriented into one dominant variant by an external factor [1].

### 2.3.3 R-Phase

The R-phase is an intermediate phase which forms during martensitic transformation before the formation of B19□ (stable martensite phase) under specific conditions. This transformation is accompanied by a marked increase in the electrical resistance of TiNi alloy; hence, this attribute can be used to determine the transformation temperature of the R-phase based on changes in electrical resistance. The transition of $B_2$ to the R-phase is similar to a martensitic transformation, with the shape memory behaviour of TiNi alloys being observable after R-phase transformation. As shown in Figure 2.4, the R-phase has a trigonal crystal structure [26].

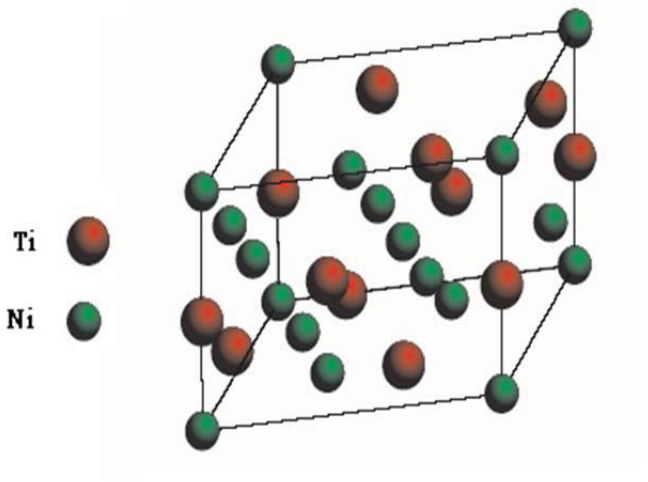


**Figure 2.4 - Crystal structure of TiNi R-phase trigonal unit cell [26]**

### 2.3.4 Precipitates

According to the Ti-Ni phase diagram, different precipitates such as $Ti_2Ni$, $TiNi_3$, $Ti_2Ni_3$ and $Ti_3Ni_4$ may form under different temperatures and compositions. These precipitations can be achieved by different aging times and temperatures. A brief review of the precipitates' crystal structures is given below.

**A. $Ti_2Ni$:** it has a cubic crystal structure with a lattice constant of 1.132 nm; its unit cell contains 96 atoms. Oxides in TiNi alloys exhibit the structure of $Ti_4Ni_2O$, which is very similar to the $Ti_2Ni$ structure [27].

**B. $TiNi_3$:** its crystal structure is hexagonal with lattice parameters of a = 0.51010 nm and c = 0.83068 nm [28].

**C. $Ti_2Ni_3$:** it has two distinctive structures at different temperatures; the crystal structure at high temperatures is tetragonal (at 373 K with lattice parameters of a = 0.3095 and c = 1.3585 nm), and the stable crystal structure at lower temperatures is orthorhombic (at 298 K with lattice parameters of a = 0.3095 nm, b = 0.4398 nm, c = 1.3544 nm) [27].

**D. $Ti_3Ni_4$**: The crystal structure of $Ti_3Ni_4$ is rhombohedral and is composed of six titanium and eight nickel atoms. The lattice parameters of the rhombohedral structure are a = 0.6704 and $\alpha = 113.85^{o}$ [27].

According to the time – temperature – transformation (TTT) diagram of Ti – 52 at. % Ni (Figure 2.5), $Ti_3Ni_4$ is the stable phase at lower aging temperatures, while of higher temperature and prolonging aging time, $Ti_3Ni_4$ changes to $Ti_2Ni_3$. Moreover, according to Figure 2.5, the upper limit of $Ti_3Ni_4$ in the Ni-rich TiNi alloy is 680 . $TiNi_3$ is the equilibrium phase at higher aging temperatures and longer aging time [24].

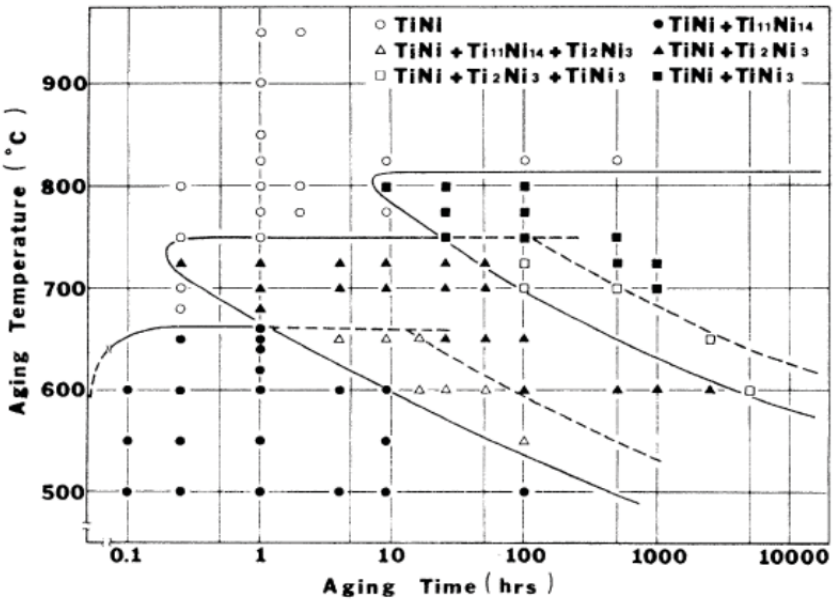


**Figure 2.5 - TTT diagram of Ti -52 % Ni [24]**

## 2.4 Transformation in TiNi Alloys

The transformation from the parent phase (austenite) to martensite can be completed during cooling in three distinctive paths, as shown in Figure 2.6. The first of these is the transformation where martensite (B19□) directly forms from the parent phase, austenite ($B_2$), as pertaining to the cooling of solution-treated TiNi.

In the second path, martensite forms indirectly under certain conditions, in at least two or more stages, which is called multi-stage transformation (MST). In this path, B19 will form as an intermediate phase; this occurs when some Ni atoms are replaced by Cu atoms ($TiNi_{50-x}Cu_x$, x = 10 -30).

The third path occurs under various conditions: first, austenite converts to the R-phase, after which this intermediate phase (R-phase) transforms to the stable martensite (B19') phase.

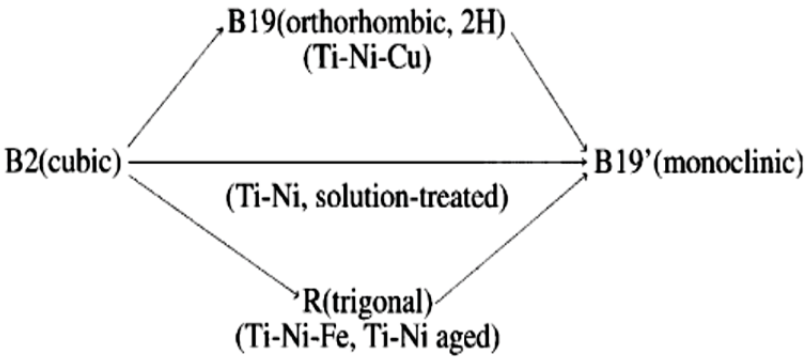


**Figure 2.6 - Three martensitic transformation paths in TiNi alloys [24]**

The conditions that lead to the formation of the R-phase are as follows [24, 29-31]:

1. The presence of a third alloy element such as Fe or Al in the composition of TiNi SMA.

2. The presence of stress field due to an appropriate dislocation structure from thermo-mechanical process or heat treatment.

3. Annealing and cold work of TiNi alloy.

4. Formation of $Ti_3Ni_4$ precipitates by appropriate aging treatments in Ni-rich (nickel contents exceeding 50.5%) TiNi alloy which can induce an internal stress field [32].

Dislocations and $Ti_3Ni_4$ precipitates can prevent the generation of high strain during transformations. Hence, the R-phase transformation, which requires only a relatively low transformation strain in comparison to direct martensitic transformation, will occur when there are $Ti_3Ni_4$ precipitations in the microstructure of the TiNi alloys.

### 2.4.1 Martensitic Phase Transformation Temperatures

$M_s$, $M_f$, $A_s$ and $A_f$ are four temperatures associated with martensitic transformation. $M_s$ and $M_f$ are denoted as martensite start and finish transformation temperatures, and $A_s$ and $A_f$ are referred to as austenite start and finish transformation temperatures. According to Figure 2.7, martensite transformation is accompanied by a specific temperature hysteresis; temperature hysteresis represents the difference between transformation temperatures during heating and cooling and varies from one alloy to another. Hysteresis is usually between 20°C and 40°C. From a microscopic viewpoint, temperature hysteresis is attributed to friction at the atomic level resulting from moving twinned martensite boundaries [33].

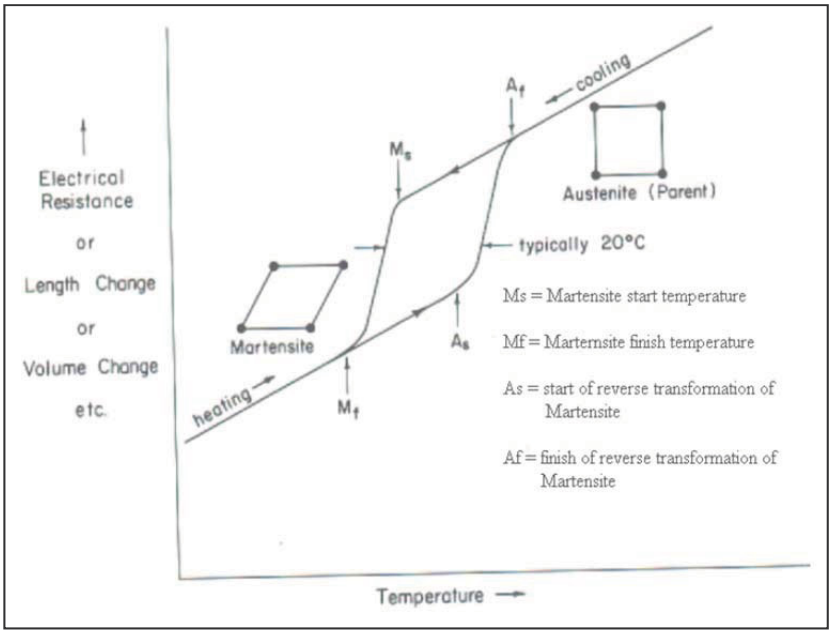


**Figure 2.7 - Physical properties versus temperature for martensitic transformation [33]**

### 2.4.2 Determination of Transformation Temperatures

One of the most essential steps in the characterization of TiNi shape memory alloys is the determination of transformation temperatures due to their impact on the presence of shape memory and superelastic effects.

The measurement of electrical resistance offers one of the oldest methods to determine transformation temperatures in TiNi alloys. In this method, the changing electrical resistance upon heating and cooling is studied. As shown in Figure 2.8, the electrical resistance of TiNi SMAs increases when the R-phase is formed. Upon starting the martensite formation at $M_s$, the electrical resistance begins to drop.

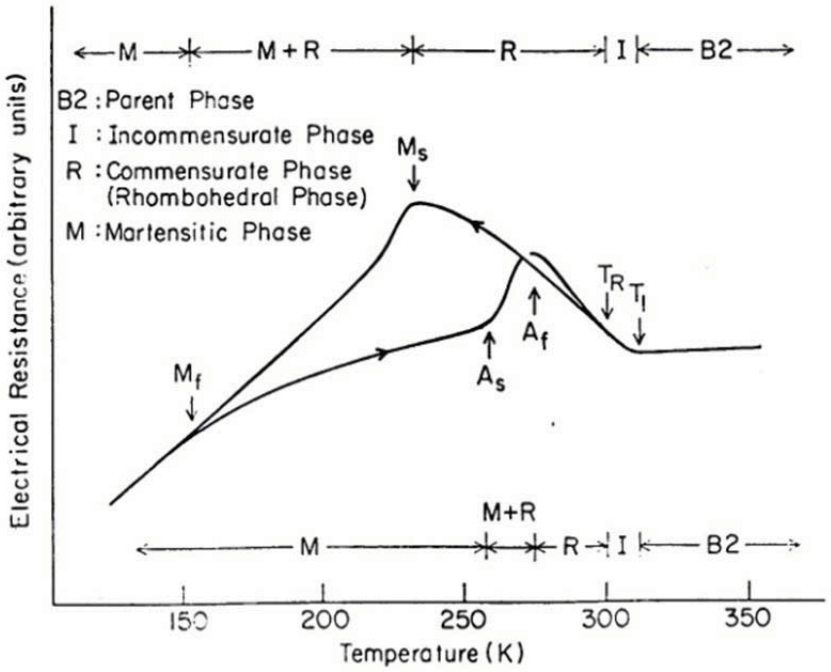


**Figure 2.8 - Electrical resistance changes during phase transformation in Ti-50.1%Ni, aging at 673K for 1hr after solution treatment in 273k [17].**

Differential scanning calorimetry (DSC) is a very useful method to determine phase transformations in metals and is thus widely used in identifying thermo-elastic martensitic transformations in shape memory alloys [35]. In the DSC method, both the

studied sample and a standard specimen are exposed to a constant heating rate; during heating, the heat flow between the two specimens will be continuously recorded. Energy absorption due to phase transformation in the studied sample will lead to a peak in the heating cycle. This endothermic peak demonstrates the transformation of austenite to martensite. Accordingly, energy released during the cooling cycle will lead to anexothermic peak in the transition of martensite to austenite [36]. As can be seen in Figure 2.9, the meeting point of the tangents in each endothermic and exothermic peaks with base line are representative of austenitic and martensitic transformation temperatures, respectively.

In multi-stage transformations in which the R-phase or B19 are formed as an intermediate phase, more than one peak occurs in the DSC diagram. For instance, in Figure 2.10, the R-phase is formed before the completion of the martensitic transformation in the cooling path and prior to the austenitic transformation in the heating cycle.

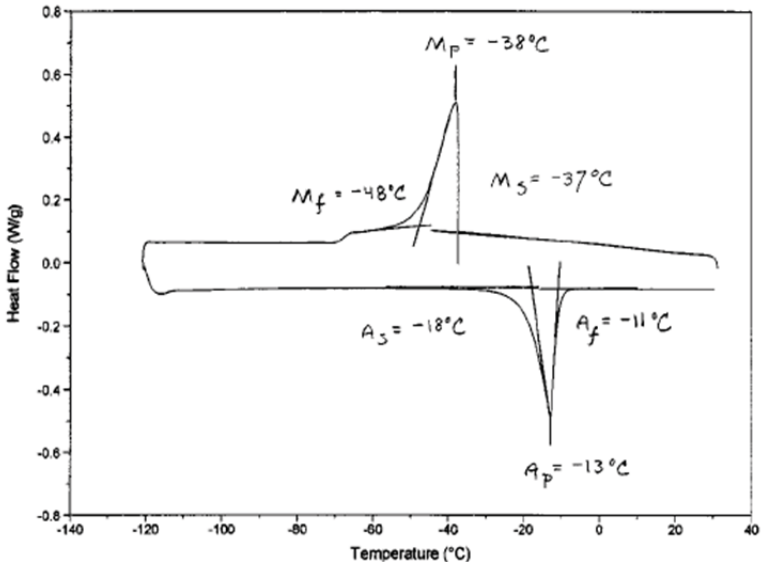


**2.10 - Determination of the transformation temperatures from DSC diagram [36]**

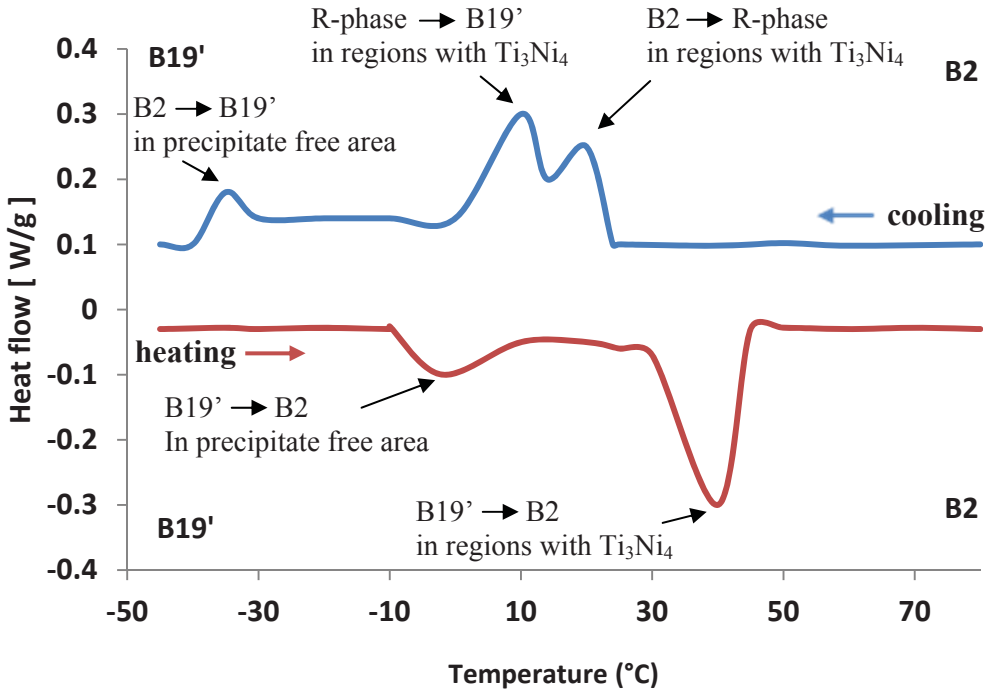


**2.9 - Illustration of the formation of the R-phase peak in a DSC diagram**

### 2.4.3 Effects of Aging Treatment on Transformation Temperatures

As discussed previously, transformation temperatures can be altered significantly by minute changes in TiNi composition or by adding different elements. However, achieving the appropriate transformation temperatures and desired properties of TiNi SMAs by adapting the composition can be very difficult due to the materials' high sensitivity to composition. Control of the transformation temperature can be also achieved by altering the aging treatment in Ni-rich TiNi alloys. Research has shown that the time span of aging treatments in each aging temperature has no effect on the transformation temperatures, a fact that is attributed to the equilibrium of TiNi and $Ti_3Ni_4$ phases. Changing the aging temperature can alter the composition of austenite in the TiNi matrix and thus the martensite and R-phase start temperatures will change. The Ni content of the TiNi matrix is reduced by decreasing the aging temperature; as a result, the transformation temperatures increase, and vice versa.

However, $M_s$ is also influenced by $Ti_3Ni_4$ precipitate's characteristics such as, density and size. Thus, the number of alternating heating/cooling cycles can change the martensite start transformation temperature due to its effect on the precipitates characteristics.

The main key of this phenomenon is the equilibrium of the TiNi and $Ti_3Ni_4$ phase, which is not stable; $TiNi_3$ is another precipitate which is more stable than $Ti_3Ni_4$. Nevertheless, $Ti_3Ni_4$ is relatively stable in normal aging treatments where the aging temperature is below 600 ℃. $Ti_3Ni_4$ is the only precipitate that has been observed in the above aging conditions. Figure 2.11 illustrates a part of a phase diagram of TiNi in which the equilibrium between TiNi and $Ti_3Ni_4$ is shown.

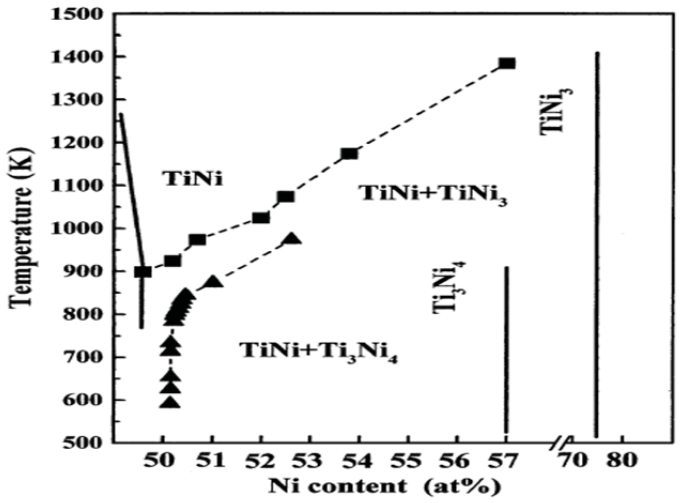


**Figure 2.11 - TiNi phase diagram [24]**

According to the phase diagram, upon forming $Ti_3Ni_4$, the Ni content of the metal matrix will decrease. R-phase and martensite start transformation temperatures are enhanced by decreasing the Ni content of TiNi alloys. Hence, the transformation temperatures will increase continuously during the aging treatment until the TiNi composition reaches the equilibrium state. At the equilibrium state, the transformation temperatures remain constant. The key here is that the constant transformation temperature at the equilibrium state is independent of the initial composition. As can be seen in Figure 2.12, two different compositions of TiNi SMAs have the same transformation temperatures after certain aging time. As can be seen in Figure 2.12, $R_s$ temperature is nearly constant from the start time of aging, while $M_s$ increases over the aging time until finally reaching a constant value after a long time interval.

$Ti_3Ni_4$ precipitates resist deformation and consequently hinder transformations in the TiNi SMAs. Upon increasing the aging time, the density and size of $Ti_3Ni_4$ precipitates are gradually increased. The transformation of austenite to the R-phase is accompanied by a small deformation, while converting the R-phase to martensite creates a much larger deformation. Accordingly, the $B_2$ to R-phase transformation is almost independent of aging time, while the martensite formation, which is accompanied by a large deformation, is significantly influenced by the size and density of $Ti_3Ni_4$ precipitations and is thus dependent upon aging time [24].

Therefore, aging emerges as a practical method for controlling transformation temperatures. This can be accomplished by different aging treatment conditions such as aging temperature and aging time, independent of the TiNi alloy composition.

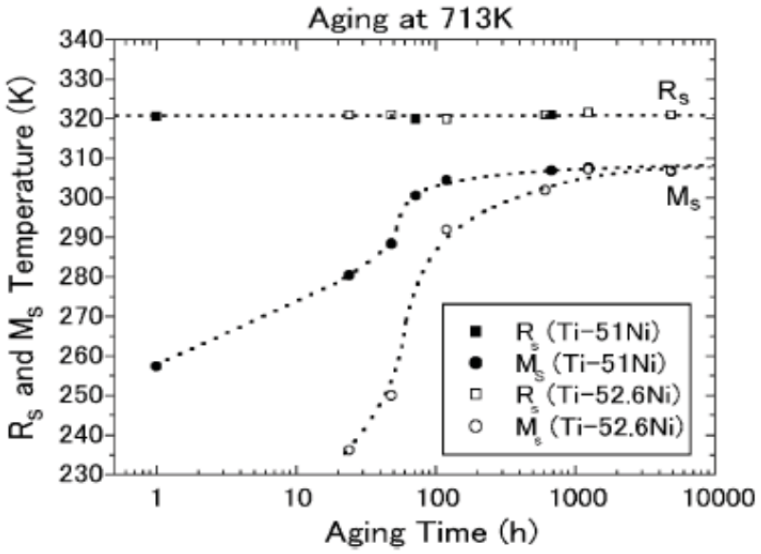


**Figure 2.12 - Effect of aging time on transformation temperatures of TiNi alloys [24]**

## 2.5 Deformation Behaviour of TiNi Alloys

In order to understand the unique properties of SMAs that derives from its unique deformation behaviour, phase transformations between the parent phase (austenite) and the product phase (martensite) must be reviewed.

When a TiNi alloy is cooled from the austenite phase to a temperature below $M_f$ without applying any external stress, twinned martensite forms. As mentioned previously, martensite has a monoclinic crystal structure with low geometrical symmetry. Hence, martensite can form in different variants while austenite has just one variant. Upon forming martensite, these variants accommodate themselves (self-accommodation martensite) to form twinned martensite.

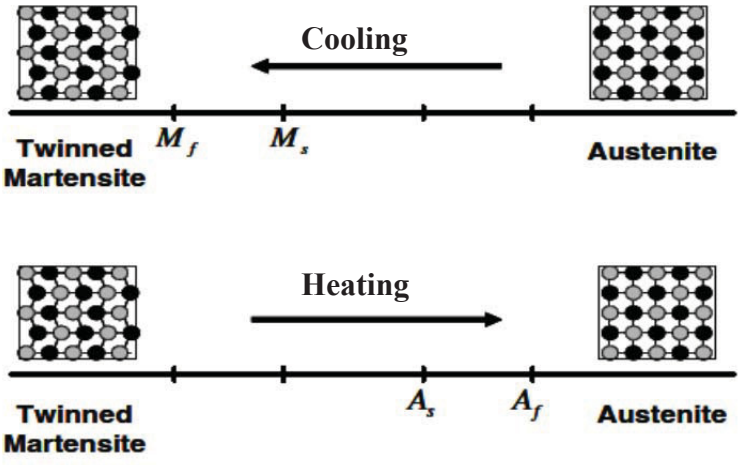


**Figure 2.13 - Forward and reverse transformations in TiNi without mechanical loading [1]**

In this manner, each variant of a variant couple accommodates the strain of other variants. Thus, the macroscopic shape changes are negligible in this transition [24,37] which is termed *forward transformation. Reverse transformation* occurs when martensite is heated to a temperature above $A_f$, at which point austenite will form from martensite. In this transition, average macroscopic shape changes are likewise negligible. Figure 2.13 shows the schematic of these transformations [24].

### 2.5.1 Shape Memory Effect

If a mechanical load is applied to twinned martensite, it converts to detwinned martensite due to the reorientation of variants. This process will make macroscopic shape changes which remain after unloading. Figure 2.14 shows the detwinning process in a stress-temperature diagram.

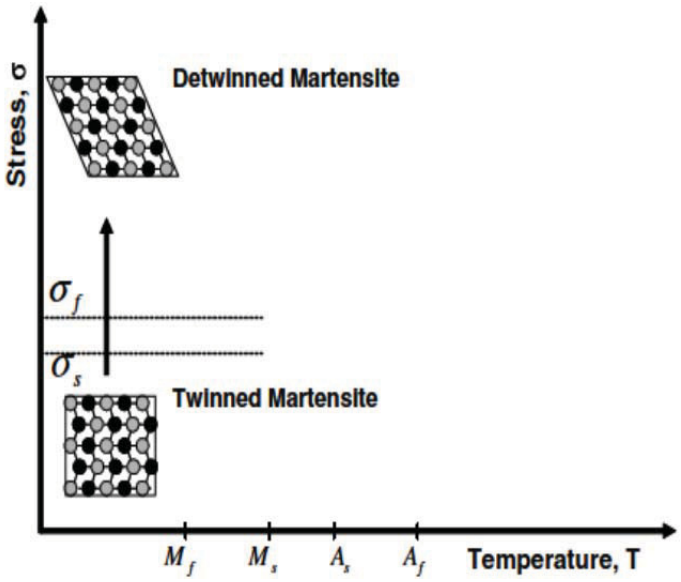


**Figure 2.14 - Schematic of the detwinning process under stress [1]**

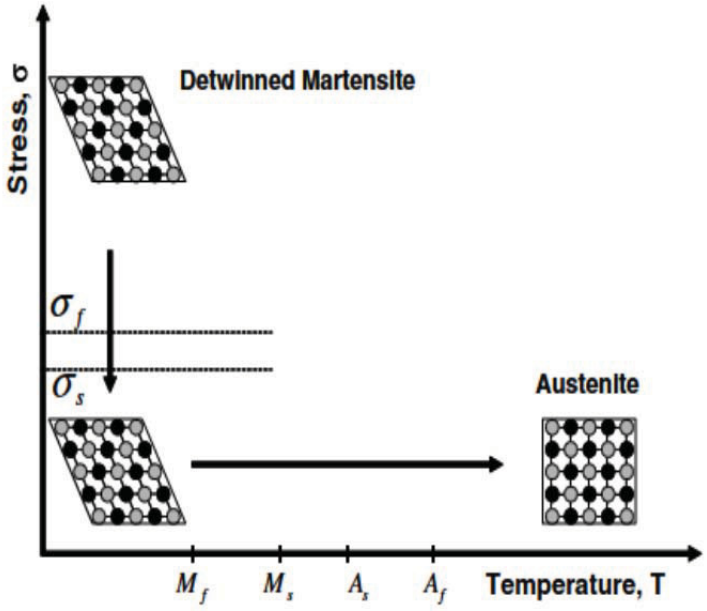


**Figure 2.15 - Schematic of the shape memory effect in TiNi alloy [1]**

Upon heating the detwinned martensite to a temperature above $A_f$, a reverse transformation will occur and martensite will transform back to austenite. During this transformation, the macroscopic shape deformation will completely recover (see Figure 2.15).

Cooling austenite to a temperature below $M_f$ forms twinned martensite, and no macroscopic shape changes would be observed. The cycle described above is the shape memory effect (SME). The minimum stress needed to start the detwinning process is the detwinning start stress ($\sigma_s$); at the detwinning finish stress ($\sigma_f$), the detwinning process is complete.

Applying stress, whether tensile or compressive, has a direct impact on transformation temperatures. As can be seen in Figure 2.16, by increasing the amount of applied stress, transformation temperatures will increase. Therefore, there is a positive slope in the stress-temperature diagram for each transformation temperature line. The new transformation temperatures (with the presence of external stress) are termed $M_s^\sigma, M_f^\sigma, A_s^\sigma, A_f^\sigma$ .

Cooling austenite under an applied mechanical load above $\sigma_s$ leads directly to the formation of detwinned martensite, accompanied by macroscopic shape change. Subsequent heating above $A_f$ leads to the occurrence of reverse transformation as well as full deformation recovery (see Figure 2.16).

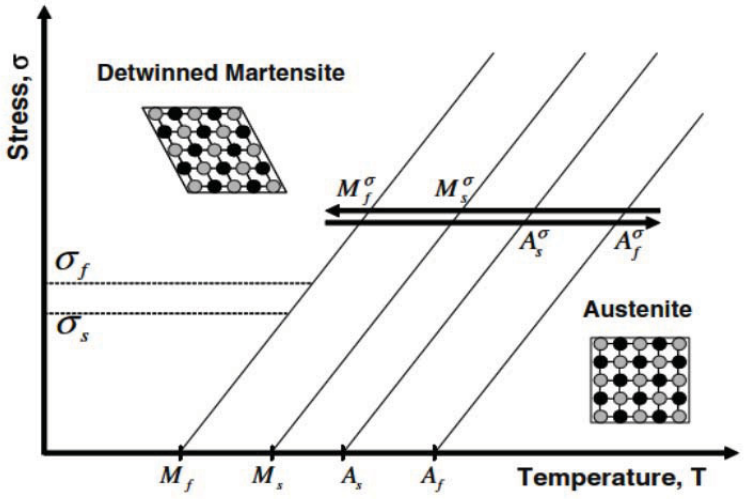


**Figure 2.16 - Forward and reverse transformation under applied mechanical load [1]**

### 2.5.2 Superelastic or Pseudo-Elastic Effect

Martensite forms in a shear-like transformation without diffusion; thus, stress can aid in martensite transitions. Indeed, sufficient amounts of stress can produce martensite even in temperatures above $M_s$, no martensite can form by cooling [24].

Stress-induced martensite (SIM) is the term applied to martensite, which forms directly from the parent phase (austenite) by applying sufficiently high stress of a constant temperature. The stress levels at which the forward transformation starts and finishes are termed $\sigma^{Ms}$ and $\sigma^{Mf}$, respectively. After unloading, the reverse transformation starts at $\sigma^{As}$ and ends at $\sigma^{Af}$. The generated strain will fully recover if the temperature is kept above $A_f$; however, if the temperature falls between $M_s$ and $A_f$, only a portion of the total strain will recover. This phenomenon is called superelastic or pseudo-elastic behaviour in shape memory alloys. Figure 2.17 illustrates the load path for the superelastic effect in SMAs [1].

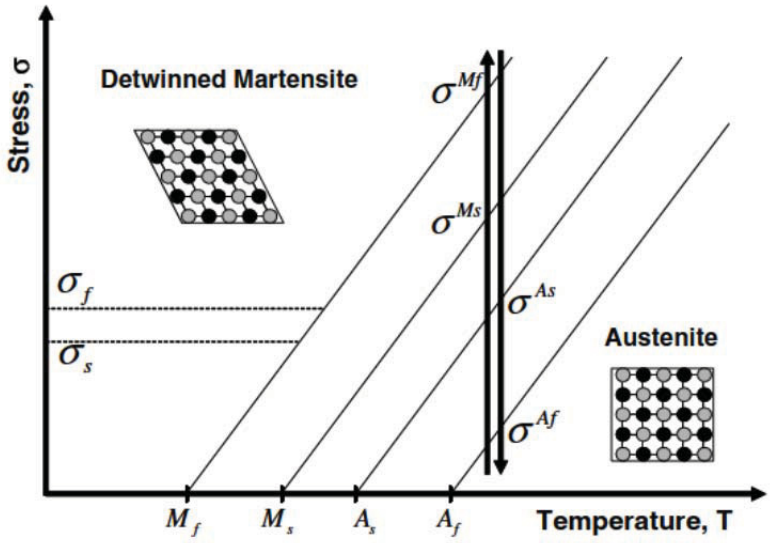


**Figure 2.17 - Schematic of the superelastic effect in TiNi alloy [1]**

### 2.5.3 Stress- Strain Curves as a Function of Operating Temperature

The deformation behaviour of TiNi alloys is strongly dependent upon temperature. As both the shape memory effect and superelasticity can occur in the same specimen, the differentiating factor is the specimen's temperature. The deformation can be divided into four mechanisms, as illustrated below.

**1. T >$M_d$:** As explained previously, martensite can form by one of two ways. The first way is by cooling it from the parent phase (austenite) to a temperature below $M_f$, which is called temperature-induced martensite. The second way is by through the application of an external force in a specific temperature range. The stress-induced martensitic transformation cannot occur at a temperature region above $M_d$; instead, the austenite will deform plastically by slip because, above $M_d$ the stress required for slip is lower than that required for an austenite-to-martensite transition. Hence, at a temperature above $M_d$, the generated strain is irreversible; TiNi behaves like a conventional material and no superelastic effect is observed (see Figure 2.18).

In Figure 2.19, the first diagram shows the deformation behaviour of austenite in TiNi at a temperature above $M_d$. It exhibits normal behaviour of a conventional austenitic phase. The curve is composed of an elastic region and a fairly short plastic deformation.

**2. $A_f < T < M_d$:** In this curve (Figure 2.19), the initial part shows the normal elastic behaviour of austenite. Under certain stress (i.e., transformation stress), austenite is converted to martensite (plateau region). This stress-plateau corresponds to the formation of stress-induced martensite. If the specimen is unloaded at the end of the pseudo-elastic plateau, the generated strain will fully recover, as shown by the dotted line. This behaviour is called the superelastic or pseudo-elastic effect. However, if loading continues beyond the transformation stress, work hardening of martensite takes place followed by fracture.

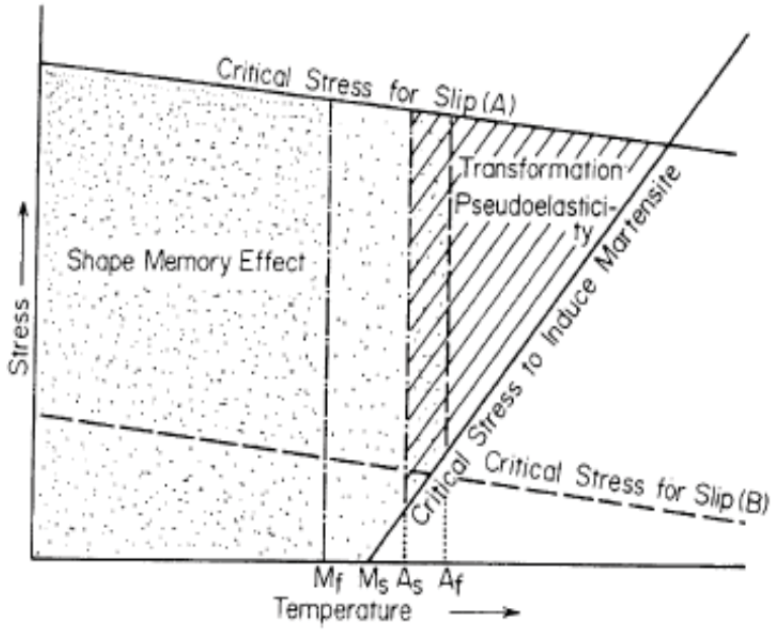


**Figure 2.18 - Shape memory and superelasticity regions in stress vs. temperature diagram [24]**

**3. $M_s < T < R_f < A_s$ :** At first, a preliminary yield occurs $Y_R$ (the R-phase yield stress). In the second stage of the curve (plateau), the strain will not fully recover by unloading.

**4. T <$M_f$:** Twinned martensite is the stable phase at temperatures below $M_f$. In Figure 2.19 (4), the first stage shows the elastic deformation of twinned martensite. At the plateau stress, twinned martensite will reorient its variants to one dominant variant under the applied stress, at which detwinned martensite forms. In this temperature region full recovery upon unloading will not occur unless the specimen is heated to temperature above $A_s$.

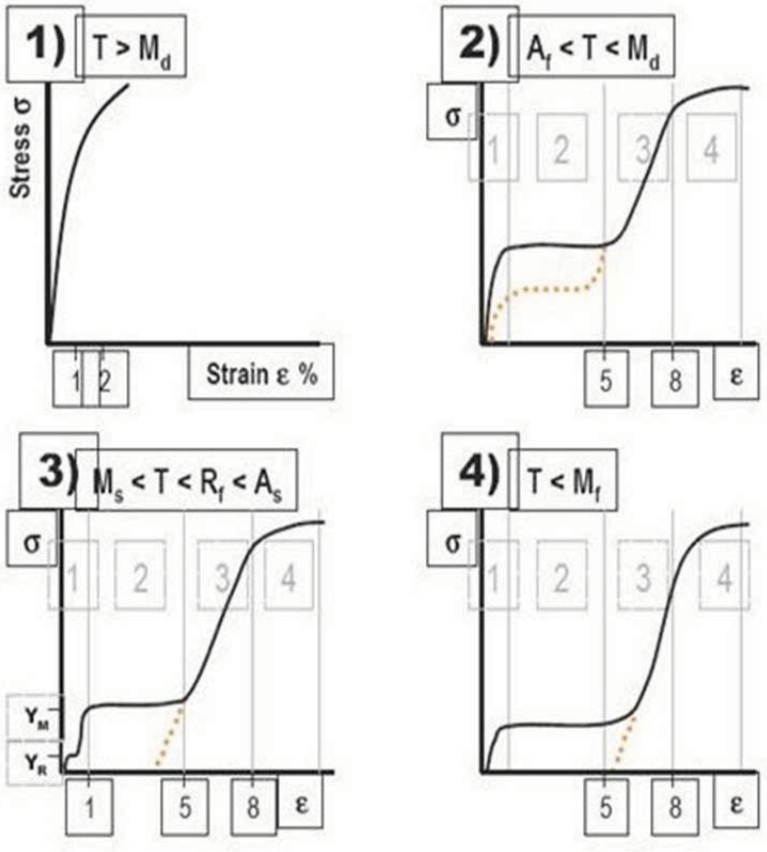


**Figure 2.19 - Stress-strain curves of TiNi alloy at different operating temperature**

The elastic stiffness of austenite and martensite in a superelastic regime can be described by the austenite Young's module ($E_A$) for before the plateau stress, and by a martensite Young's module ($E_M$) after the plateau stress (see Figure 2.20; note that the material isotropy is assumed in both cases).

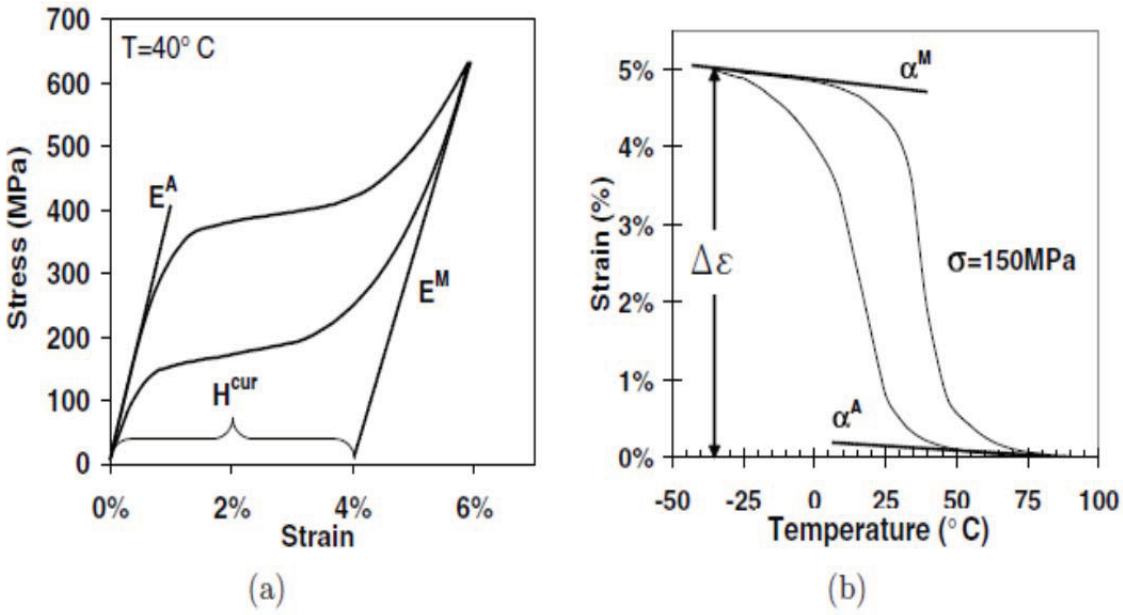


**Figure 2.20 - (a) Stress-strain curve in superelastic regime, (b) temperature-strain curve in shape memory regime [1]**

The application of shape memory alloys in actuators involves heating under constant applied stress. Figure 2.20 (b) illustrates strain vs. temperature curve under constant load. The thermo-elastic effect in the temperature region above $A_f$ and below $M_f$ (i.e., outside the transformation temperature region) which are nearly linear parts of this plot, are attributed to the thermal expansion of the SMA, similar to conventional materials. In Figure 2.20 (b), the slopes of stress vs. temperature curve, indicated by $\alpha^A$ and $\alpha^M$, represent the thermal expansion coefficients for austenite and martensite phases, respectively.

## 2.6 Factors Affecting TiNi Properties

### 2.6.1 Strain Rate

It has been shown in several studies that varying the strain rate in loading and unloading tests can have substantial effects on the mechanical behaviour of shape memory alloys. For instance, increasing the strain rate leads to shortening the plateau and raising the stress-strain curve in tensile loading [40, 41]. Also, it has been shown that the differences between compression and tension characteristics of TiNi alloys are influenced by strain rate and temperature [42].

Some investigations have been conducted to study the interaction between parameters such as stress, temperature, deformation and strain rate as well as the effects of strain rate on stress-induced martensite transformation (transformation stress) and superelasticity behaviours. The studies show that TiNi is very sensitive to strain rate. The quasi-static and dynamic deformation in tensile and compression tests (Figure 2.21) has been employed [43] to investigate the impact of strain rate on stress-induced and thermal-induced martensite transformation. Figure 2.21 shows the engineering stress-strain curves resulting from compression and tension tests of Ni-rich TiNi with both low strain rate (quasi-static, 0.001/s) and high strain rate (dynamic, 1200/s) in ambient temperatures (above the $A_f$). The smaller strain recovery after unloading and higher transformation stress can be seen in compression test curves.

The stress-strain curves for TiNi alloy are asymmetric in tension and compression situations, an asymmetry termed by Plietsch and Ehrlich [44] as the strength differential effect (SDE). Several hypotheses have been proposed for mechanisms responsible for SDE in TiNi shape memory alloys. According to Orge' as and Favier [45] the asymmetry in deformation behaviour between tension and compression is attributable to the inherent characteristics of stress-induced martensite transformation.

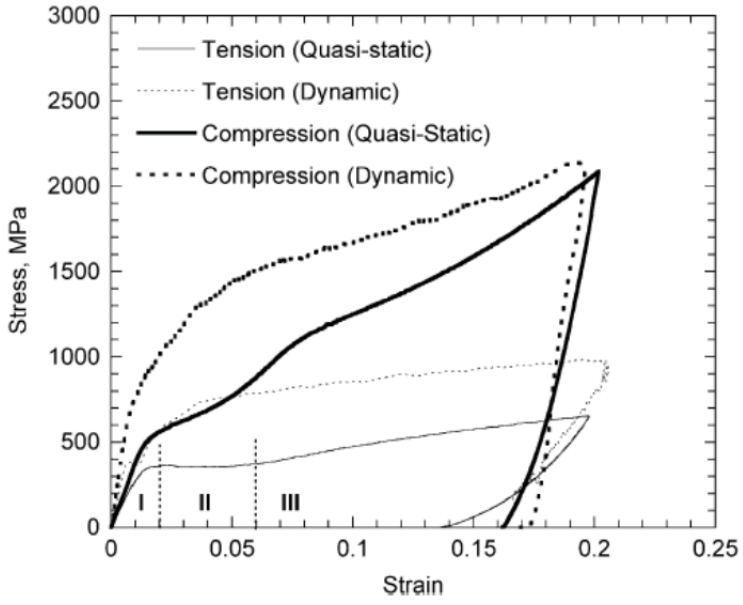


**Figure 2.21 - Engineering stress-strain curves of Ni-rich TiNi alloy at different strain rates at ambient temperature [43].**

This asymmetry has been studied in TiNi single crystal as well as polycrystalline TiNi [44] and it has been observed that the value of SIM transformation strain in tension for a TiNi single crystal double in compressive. They suggested that different variants of martensite which form selectively during SIM transformation can cause the SDE in superelastic regime in TiNi alloys. As can be seen in Figure 2.22, there is no significant stress plateau in the high strain rate in compression, while in the tension test, a slight plateau can be observed.

While the strength of typical metals and alloys decreases with increasing temperature, it is more complicated for SMAs in the superelastic temperature region (between $A_f$ and $M_d$) due to SIM transformation. Upon increasing temperature during a high strain rate compression test, the stress level decreases for strains above 3%, while for initial deformation (less than 3%), stress increases at high temperatures.

In contrast, increasing temperature in a high strain rate tensile test has no simple or direct correlation between temperature increment and stress level. Figure 2.22 illustrates the stress-strain curves at different temperatures and strain rates in order to compare asymmetry between tension and compression tests. Figure 2.22 (a) is at -196 °C (SMA regime) and the temperature increment between each curve is 200 °C. It can be understood from all curves that, upon increasing temperature, the asymmetry between compression and tension conditions decreases in both quasi-static and dynamic situations. The minimum asymmetry corresponds to 400 °C in low strains (<5%); also, the decrease of asymmetry is more considerable at high strain rates.

The transformation of austenite into martensite is an exothermic transformation, while the transformation of martensite into austenite is endothermic. The heat generation or absorption during the transformations can cause changes in specimen temperature within a test. These phenomena can restrict the applied stress rate during testing of an SMA. Using controlled stress rate is more vital during superelastic testing because this test is often conducted in constant temperatures. Upon loading, the heat generated by forward transformation can raise specimen temperature if the applied stress rate is high. In contrast, in low strain rates (quasi-static state), the generated heat can be removed or dissipated by convective and conductive processes, and thus specimen temperature changes are negligible. Specimen temperature will be reduced during unloading (reverse transformation) in high stress rates due to heat absorption [1].

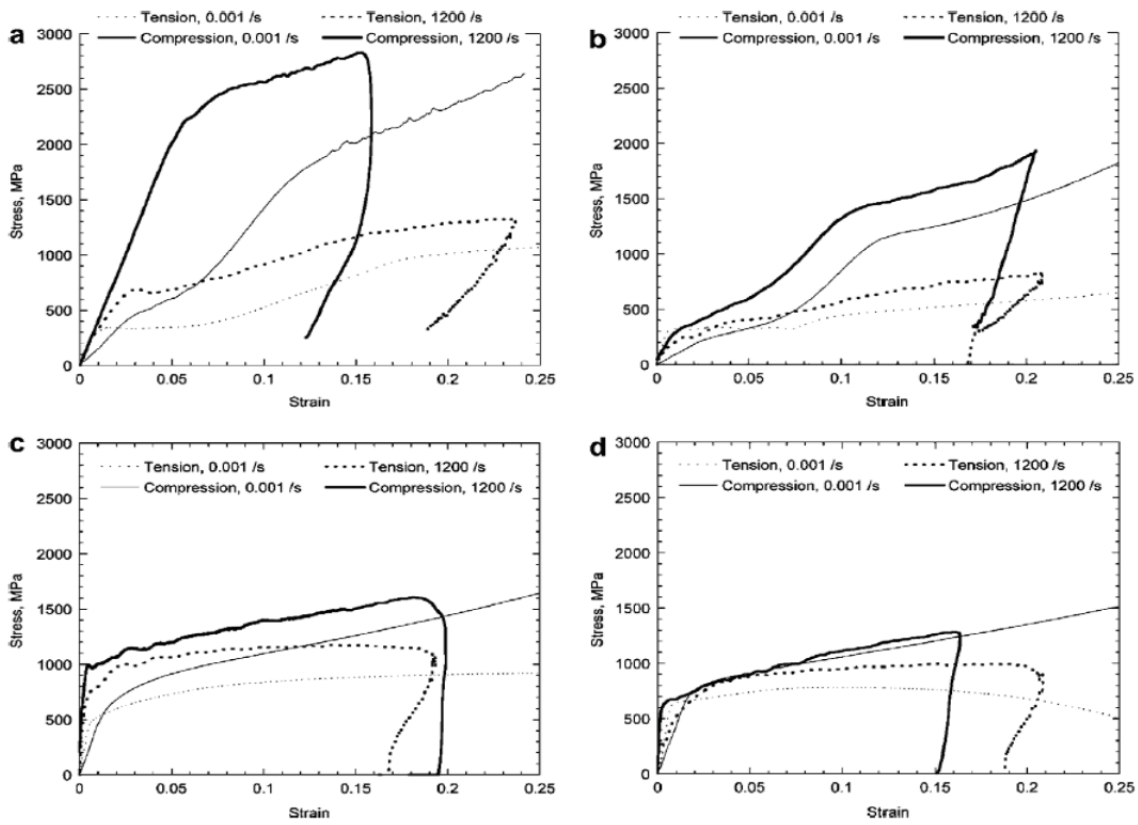


**Figure 2.22 - Stress-strain curves of TiNi shape memory alloy at different strain rates and temperatures under compression and tension, a)-196 °C, b) 0°C, c) 200°C, d) 400 °C [44]**

### 2.6.2 Material History

Similar to other materials, parameters pertaining to the history of material (e.g., heat treatments, cold work, etc.) have a direct impact on shape memory alloys behaviour. However, SMAs are more sensitive to their prior history compared to other materials due to their specific behaviour and microstructural changes. These parameters and their effects are vital for appropriate material selection as well as designing suitable experimental tests.

Wires and plates are subjected to substantial cold working or hot working during their fabrication processes. Consequently, the material will suffer from changes in internal stress, microstructure, shape and size of precipitates due to this substantial permanent deformation [1].

The amount of plastic deformation can change the phase transformation and shape memory effect of TiNi shape memory alloys. If plastic deformation increases, phase transformation and SME can deteriorate, resulting in the formation of defects in the materials structure and impeding martensite nucleation and growth [47].

The thermo-mechanical behaviour of SMA is very sensitive to prior heat treatments due to substantial changes in the microstructure. While full anneal heat treatment deteriorates the superelastic effect in SMAs, adequate precipitates are required for the superelasticity effect in SMAs and should be formed by particular heat treatments such as aging [1].

### 2.6.3 Cold Work

Properties of TiNi SMAs such as strength, recoverable strain and hardness can be significantly influenced by material processing. The fabrication process used for producing TiNi wires is accompanied by large plastic deformation and cold work. For instance, multiple drawing and rolling procedures are performed in fabricating TiNi alloy wires, and this creates a high amount of cold work [59].

Cold work can increase dislocation concentrations in the matrix and enhance TiNi strength while decreasing recoverable strain [60,61]. Increasing dislocation concentrations also increases material hardness in both austenite and martensite states. Hence, hardness increases upon increasing the amount of cold work [62, 63].

It has been demonstrated that by increasing cold work, shape memory recovery deteriorates and stress plateau shortens; also, the plateau can disappear at higher cold work percentages [64]. However, subsequent annealing treatment can recover the stress plateau. The increase of strength and decrease of ductility are other influences of cold work that have been reported by Lin and Wu [64].

Anisotropic shape memory behaviour is yet another effect of cold working. For instance, after cold rolling, TiNi SMAs show the shape memory effect in the rolling direction, but there is no shape memory effect in the transverse direction.

It has been demonstrated by Mitwally et al. [60] that, by increasing the amount of cold work, the volume fraction of martensite will increase and thus tensile strength and hardness will also increase. Due to the formation of irreversible martensite, the superelastic plateau will vanish at higher cold work percentages, as will ductility and the shape memory effect. On the other hand, annealing can enhance the austenite volume fraction as, upon recrystallization and grain growth at specific annealing temperature, superelasticity and hardness are increased [60].

Miller and Laguudas [59] studied the effects of different magnitudes of cold work (10 % - 40%) and subsequent annealing. They found that the amount of cold work and the annealing temperature can have a significant impact on thermally-induced transformation hardening and transformation strain. They also found that higher amounts of cold work enhance the required stress for plastic strain corresponding to the transformation, thereby, subsequently decreasing the total generated plastic strain during a loading cycle.

## 2.7 Indentation Behaviour of TiNi Shape Memory Alloys

While bulk properties and the behaviour of TiNi SMAs have been studied extensively, microscopic research into shape memory effect and superelastic behaviour of SMAs under contact loading conditions is limited. However, much experimental evidence indicates that TiNi SMAs exhibit a noticeable asymmetry in their tension and compression characteristics, such as, high stress plateau under tensile loads and no flat plateau under compression [65-67].

Due to increasing applications of TiNi SMAs in micro-electro-mechanical-systems (MEMS) as well as biomedical and surface engineering applications, micro and nano-indentation tests have been widely used to investigate the mechanical properties of TiNi SMAs [68-70], under compressive loads.

Grummon and Cheng [71, 72] conducted an investigation into the shape memory effect and superelastic behaviour of shape memory alloys, in particular TiNi alloys, by using micro- and nano-indentation techniques.

The stress distribution in an indentation test is very different from that in simple tension or compression tests and is non-uniform. Moreover, the complexity of the stress field under micro- and nano-indentation tests alters both the materials response and the deformation mechanisms [73].

Stress magnitude and distribution are strongly dependent on indenter shape. Indenter geometry can be either spherical, which has a length scale (ball radius R), or sharply pyramidal (such as Vickers' indenter). If it is assumed that there is no imperfection in the sharp pyramid indenter tip, it thus has no length scale [71]. The stress is higher and more complicated under a sharp indenter and also leads to unpreventable slip-plasticity in the material. Dislocations that are produced due to slip-plasticity can deteriorate shape memory effect [74]. For example, the maximum strain recovery is only 45% when a Berkovich indenter has been used [74] while, the generated strain can be fully recovered under a spherical indenter.

The stress distribution is the main reason for differences between the amounts of superelastic strain recovery. In a sharp pyramidal indenter, the stress is highest at the tip of the indenter, and thus plastic deformation will occur as soon as contact is made between the indenter and the specimen surface. Therefore, high deformation will occur in the specimen due to dislocation movements, with this strain exceeding the recoverable strain by superelasticity. In contrast, stress distribution under a spherical indenter is such that the maximum stress and maximum strain are less than that induced by a sharp pyramidal indenter. Accordingly, under low stress, stress-induced martensite can form and complete strain recovery would be expected [71, 75].

Superelastic effect under indentation can be evaluated by energy consumption [76]. The main parameters in this approach are recoverable deformation energy ($W_{rc}$) and the ratio of recoverable energy to the total deformation energy ($\eta$) during loading and unloading cycles.

The magnitude of the total deformation energy ($W_t$) and $W_{rc}$ can be calculated by measuring the area enclosing the load vs. depth curve in the loading and unloading parts, respectively. These areas can be calculated by the following equations, as shown in Figure 2.23.

Where L is load and D is depth, $D_{max}$ is the maximum depth in the final load and $D_r$ is the residual strain (depth) after unloading.

High values of $W_{rc}$ and η are attributed to pseudo-elastic behaviour in the material. As such, there is less damage after unloading because the pseudo-elastic material can absorb more compressive energy. In contrast, conventional materials have a nearly vertical unloading curve, which represents lower $W_{rc}$ and η; because of this, they would suffer more plastic deformation (damage) during indentation [76, 77].

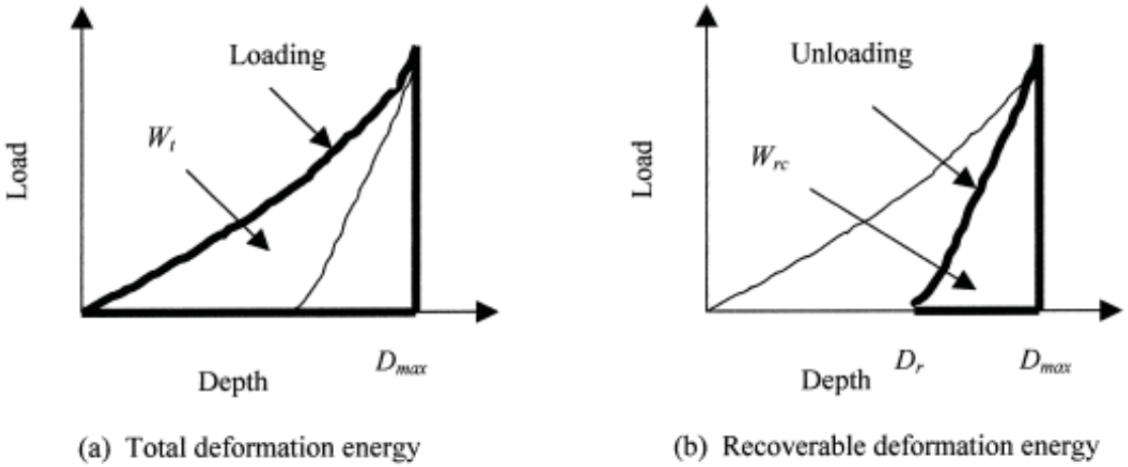


**Figure 2.23- The enclosed area to load vs. depth curve for calculating $W_t$ and $W_{rc}$[76]**

Other parameter affecting the deformation behaviour of superelastic TiNi in indentation tests is test temperature. The effects of temperature on superelasticity have been studied by Zhang et al. [78]. The superelastic effect in TiNi thin films has been observed at approximately 100 K above $A_f$ in an indentation test. However, in uniaxial tension and compression tests, superelasticity can be seen at about 40 K above $A_f$ [78]. On the other hand, the indentation test was performed for both Ti-rich and Ni-rich TiNi SMAs at temperatures below $A_f$, during which superelasticity was not observed in either specimen.

Also, the recovery ratio is medium in temperatures between $M_s$ and $A_f$ and it is attributed to the presence of an R-phase in the specimen, which does not have any considerable superelasticity or shape memory effect. The highest recovery ratio was observed in temperature ranges between $A_f$ and $A_f$ + 100k. By increasing the temperature, the critical stress for slip in austenite would decrease. Thus, in a specific combination of stress and temperature, the slip in austenite will start and plastic deformation of austenite will be the dominant deformation mechanism. This phenomenon can deteriorate superelastic effect, thus, the recovery ratio, at higher temperatures.

### 2.7.1 Sink-in and Pile-up Phenomena in Indentation

Since the Young's modulus of the diamond spherical indenter is much higher than the Young's modulus of TiNi SMAs, it can be assumed that the diamond tip of the indenter is rigid due to its negligible deformation during indentation. Figure 2.24 illustrates the contact area between indenter and the surface of the specimen; the $a_c$ in this figure is the radius of the contact area. Upon loading, the indenter moves into the specimen surface; the generated depth ($h$) is the amount of displacement of the indenter. This amount is not the same as the distance between the indent depth and the specimen surface *($h_c$)*. Here, two different phenomena can occur: pile-up and sink-in. If $h$ is larger than $h_c$, the surface specimen in the vicinity of the indenter goes down, which is called a 'sink-in'; a 'pile-up' occurs when $h$ is smaller than $h_c$, as depicted in Figure 2.24.

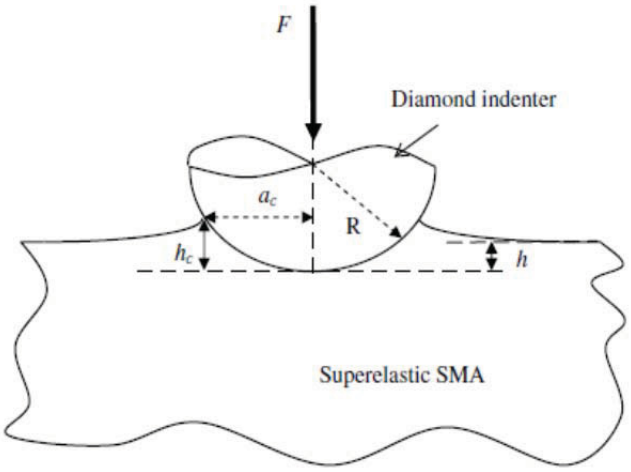


**Figure 2.24 - The contact area of the spherical indenter and the specimen surface [79]**

Regarding the temperature dependence of phase transformation in TiNi shape memory alloys, sink-in usually occurs at lower temperatures and pile-up at higher temperatures [79]. The occurrence of pile-ups or sink-ins is attributed to strain hardening of the specimen. In higher temperatures (where the deformation of TiNi SMAs is associated with phase transformation), the magnitude of strain hardening is negligible, while there is significant strain hardening at lower temperatures (where the reorientation of martensite occurs) [80]. Huang et al. [80] performed indentation tests with sharp indenters at low temperatures (i.e. the shape memory effect regime). They observed that maximum indentation depth decreases when temperatures increase. Moreover, they discovered that the surface mode after indentation in the shape memory regime is sink-in but then became pile-up after heating. Figure 2.25 illustrates the cross-sectional view of the indent while being heated at different temperatures. The amount of sink-in and pile-up is influenced by the strain hardening and yield stress [79].

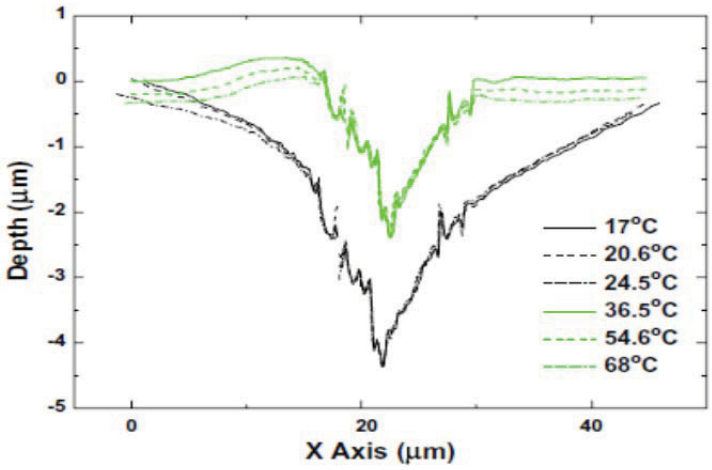


**Figure 2.25 - Cross-sectional view of the indent during heating at different temperatures [80]**

Unfortunately, only limited fundamental research work on the deformation characteristics of TiNi alloys under localized compressive load has been reported in the open literatures. Also, since superelastic TiNi is a potential candidate for bearings and gears applications, there is in dire need of finding out the effects of temperature and loading rate on deformation behaviour of TiNi SMAs under indentation loading. Furthermore, there is no comprehensive investigation on the microstructural evolution of TiNi alloy during simultaneous heating and loading, and implications of heating TiNi shape memory alloys in real life applications. Hence, a complete study of deformation behavior of both superelastic and shape memory TiNi alloys under tensile load at different temperatures is needed.

# CHAPTER 3 EXPERIMENTAL METHODS

The different methods used in the research to analyze samples and collect data are highlighted in this chapter. In section 3.1, a description of the materials used for tensile tests is provided, along with the preparation steps performed on the received materials prior to testing. Also, the differential scanning calorimetry (DSC) method used to characterize the transformation temperatures of the samples is described. Tensile test conditions are provided at the end of the section. Microstructural techniques, in particular, metallography and x-ray diffraction are outlined in section 3.2. Section 3.2 also describes the indentation techniques.

## 3.1 Tensile Tests

In order to establish an understanding of the temperature-dependent deformation behaviour of shape memory and superelastic TiNi alloys, tensile tests were performed at three different temperatures.

### 3.1.1 Materials

Thin sheets of shape memory and superelastic TiNi with a thickness of 0.1 mm were obtained from Johnson Mattey Inc. The as-received TiNi alloy sheets were hot rolled, flat annealed and grit blasted at source. The chemical compositions (weight %) of the as-received alloys are given in Table 3.1. The transformation temperatures are very sensitive to changes in composition. For example, the nickel content of the superelastic alloy is only 1 % higher than the shape memory alloy; this resulted in an almost 80 °C rise in the austenite start temperature.

**Table 3.1 - Chemical composition of superelastic and shape memory TiNi (wt%)**

| Elements | Ti | Ni | C | O | Total all others |
|---|---|---|---|---|---|
| **Superelastic** | 43.85 | 55.87 | <0.05 | <0.05 | <0.20 |
| **Shape memory** | 44.85 | 54.87 | <0.05 | <0.05 | <0.20 |

### 3.1.2 Differential scanning calorimetry

Differential scanning calorimetry (DSC) tests were conducted in order to determine the transformation temperatures of both shape memory and superelastic alloys. DSC was performed using a Universal V.4.3A TA Instruments Q200 Differential Scanning Calorimeter. The shape memory sample was held isothermally at -50 °C for 2 minutes and then heated to 120 °C at a rate of 10 °C/min. The temperature scan range for superelastic specimen was -100 °C to 50 °C.

Measurements were performed under a helium atmosphere using the liquid nitrogen cooling accessory as a cooling unit. The cell was calibrated with an indium standard reference material (melting point 156.6°C and an enthalpy of 28.71 J/g) prior to samples being run. Dipentyl ammonium chloride as a second temperature reference was also used; this has a known transition of -29.31°C.

### 3.1.3 Tensile Tests Conditions

Tensile specimens were cut into the standard bowtie shape with dimensions of 115mm × 3mm × 0.1mm and a gage length of 73 mm using laser machining. Tensile tests were performed using a miniature tensile tester from Pasco Inc. (Figure 3.1) at a strain rate of 4.5 mm/min. Tests were conducted at three different temperatures for both superelastic and shape memory samples, namely: 0 °C, 25 °C and 85°C. Various transformations will occur at these temperatures in both superelastic and shape memory TiNi which can alter the deformation behaviour of TiNi alloys. For 0 °C, the tensile test was performed while the specimen was immersed in ice. For the 85°C, the specimen was heated using a dryer during the tensile test. Temperatures during tests were monitored using Omega thermocouple.

Young's modulus, transformation stress (plateau stress), and elastic strain at all three different temperatures were calculated from the stress-strain curves. The Young's modulus was determined by measuring the slope of linear portion of the stress -strain curves with an accuracy of more than 95%.

### 3.1.3.1 In-Situ Tensile Tests

For a direct observation of the TiNi SMA microstructure evolution while heating/cooling during loading, the tensile tester was mounted on an optical microscope stage. TiNi specimens were ground using 320, 400 and 600 grit SiC abrasive papers and then finely polished using 9, 3 and 1 μm diamond paste. The effects of heating and cooling the specimens (during tensile loading) in the plateau region from room temperature to 85 °C were observed.

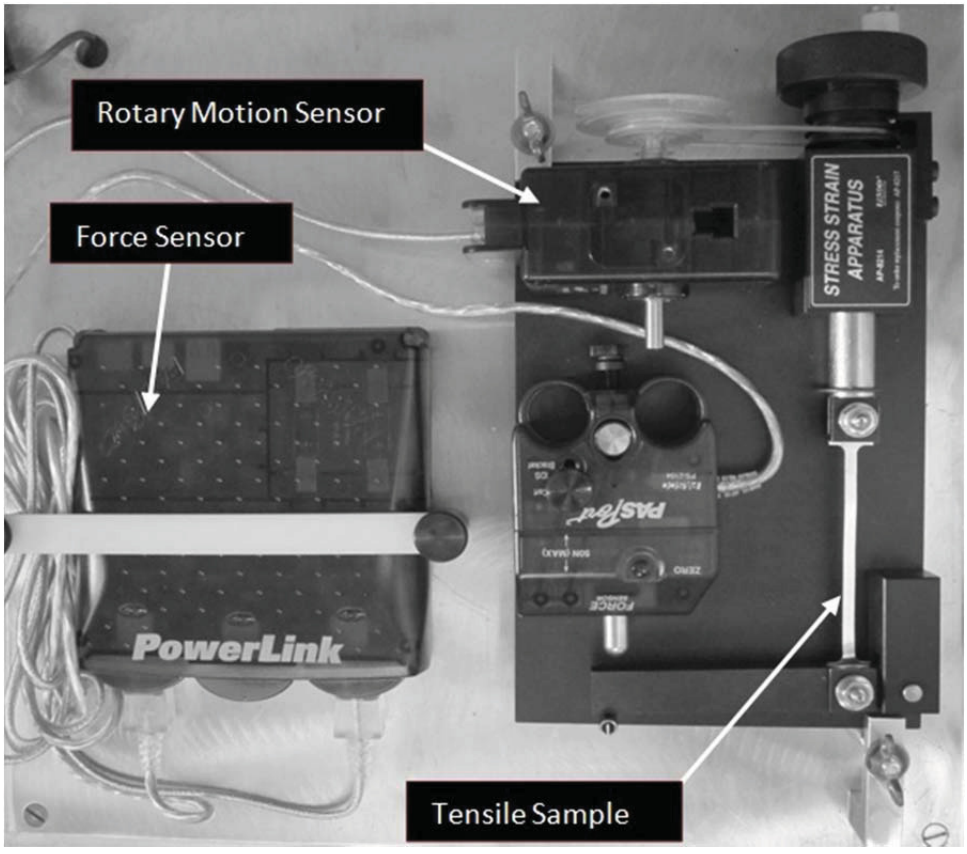


**Figure 3.1 - Miniature tensile tester**

## 3.2 Indentation Tests

In order to establish an understanding of the effects of temperature and strain rate under dynamic compressive loads on the deformation of superelastic TiNi alloy, indentation tests were performed at various temperatures and load application rates using spherical and sharp indenters.

### 3.2.1 Materials

Superelastic TiNi shape memory alloy sheets with a dimension of 47 mm × 47 mm × 1 mm and an austenite start temperature ($A_s$) of -10 °C were obtained from SAES Smart Materials Inc. The sheets were hot rolled, annealed and grit blas. The nominal composition of these superelastic sheets was determined using a Perkin Elmer Optima 7300 ICP-OES chemical analyzer, and is given in Table 3.2.

**Table 3.2 - Chemical compositions of superelastic TiNi indentation specimens (wt. %)**

| Elements | Ti | Ni | Si | Na |
|---|---|---|---|---|
| Wt.% | 43.8134 | 55.1729 | 0.3003 | 0.1662 |

In order to compare the deformation behaviour of superelastic TiNi with other conventional materials, AISI 304 stainless steel plates with dimensions of 50 mm ×50 mm × 2 mm were obtained and tested.

The transformation temperatures of superelastic indentation samples were determined by conducting differential scanning calorimetry tests on a representative sample with the approximate weight of 32.6 mg. The test procedure was similar to that of tensile test samples. The superelastic sample was held isothermally at -100 °C for 2 minutes and then heated to 100 °C at a rate of 10 °C/min.

### 3.2.2 X-Ray Diffraction

An x-ray diffraction (XRD) test was performed to identify phases present in TiNi samples. The XRD test was performed at room temperature using a high speed BrukerD8 Advance XRD machine employing Cu radiation with a tube current of 40 mA and tube voltage of 40 kV. The scanning angle range (2θ) was between 20° and 140° with a step size of 0.05°. Figure 3.2 shows the Bruker D8 Advance XRD system and Figure 3.3 depicts the Cu tube and the high speed LynxEyeTM detector.

Bruker's EVA software was used to analyse the diffraction patterns and match to similar diffraction patterns in the international centre for diffraction data (ICDD) powder diffraction file (PDF) database.

**Figure 3.2 - Bruker D8 Advance XRD system**

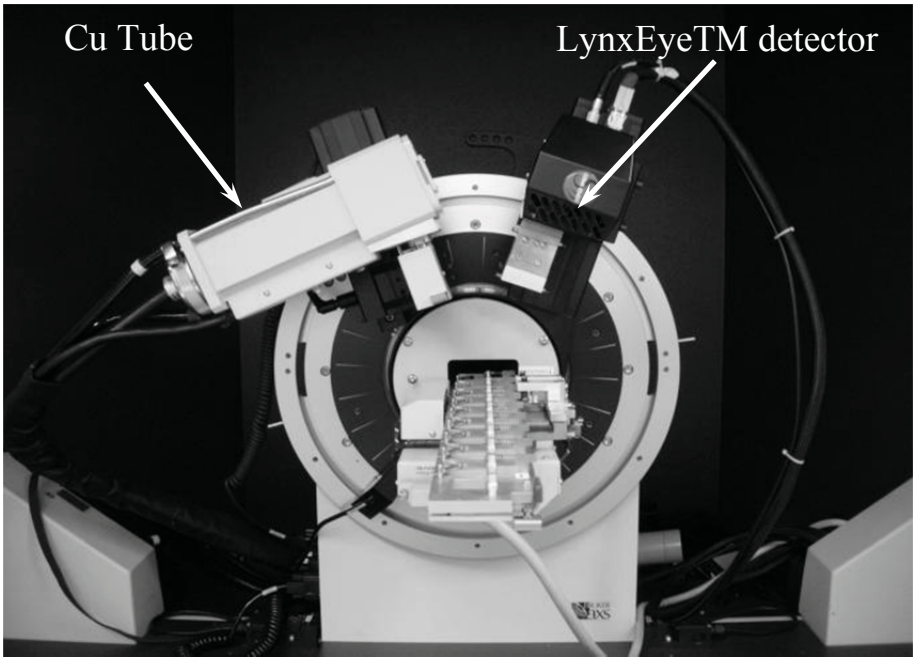


**Figure 3.3 - XRD diffractometer**

### 3.2.3 Optical Microscopy

In order to investigate the microstructure of as-received TiNi, an indentation sample was ground using 400 and 600 grit SiC abrasive paper and polished using a 9, 3 and 1 μm diamond suspension. The polished specimen was then etched using 10 ml HF, 25 ml $HNO_3$ and 100 ml $H_2O$.

Microstructural images were captured using Unitron Optical Microscope equipped with a Micro Metrics digital camera, and the images were analysed using Micrometrics SE Premium image analyser software.

### 3.2.4 Indentation Tests Conditions

All indentation tests were performed using a Universal Micro-Tribometer (UMT) (manufactured by CETR, USA). Figure 3.4 (a) depicts the complete tribometer system and Figure 3.4 (b) illustrates a closer image of the sample chamber, load sensor and indenter.

The calibrated normal load (Fz) and indentation depth (C) were measured and continuously recorded using a data acquisition system. Prior to the indentation tests, all specimens were prepared and polished using 400 grit SiC abrasive paper to ensure smooth and oxide-free surfaces.

In order to maintain a constant downward loading rate, the load was applied using a motor attached to a 100 N load sensor that can measure the normal load with an accuracy of 0.01 N. The tester also allowed depth monitoring of indentations (C) during the test with an accuracy of 0.01 μm.

Both spherical and sharp indenters were employed for the indentation tests. A tungsten carbide ball indenter with a diameter of 6.3 mm and a hardness of HRA 92 was used as a spherical indenter. As a sharp indenter, a pyramidal diamond indenter was used. Both sharp and spherical indenter holders were directly attached to a suspension system, which itself is directly attached to a 100 N load sensor.

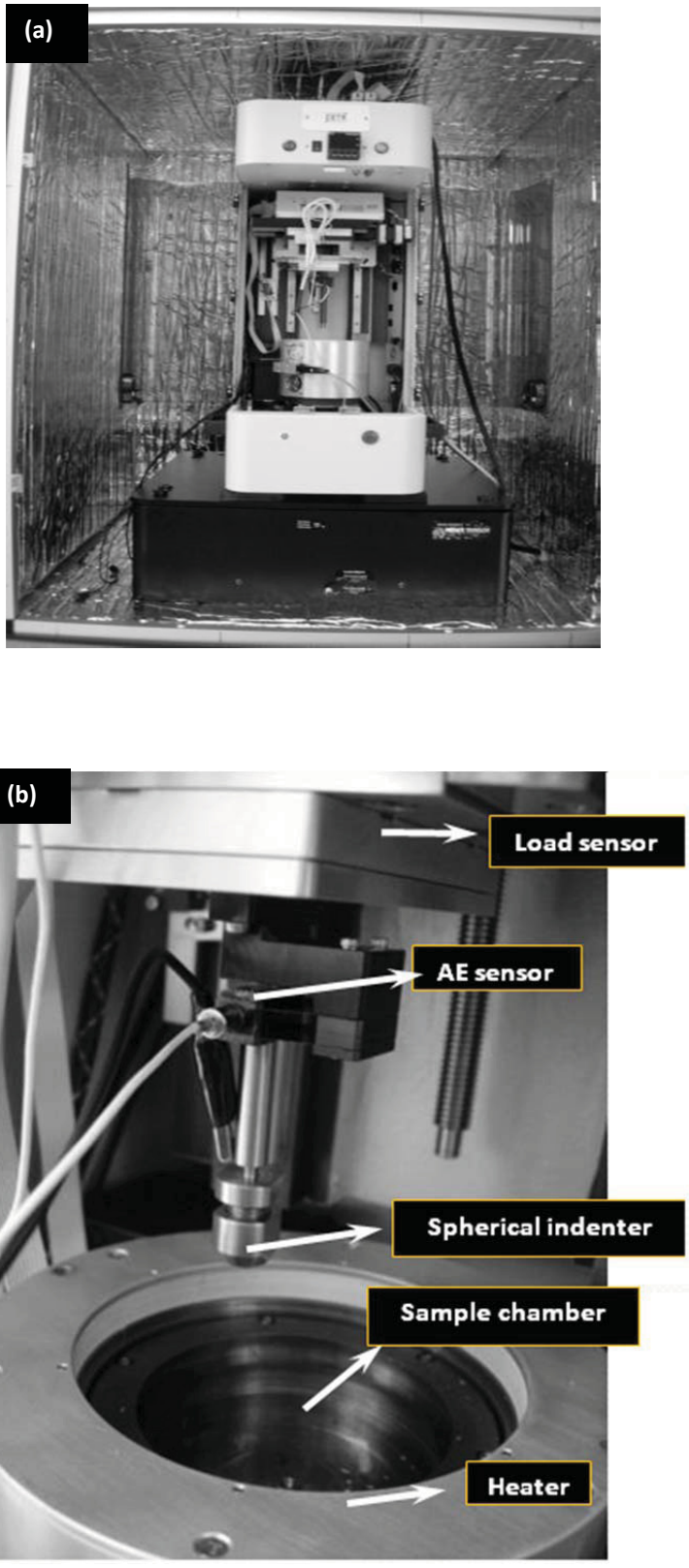


**Figure 3.4 - (a) Universal Micro-Tribometer, (b) chamber, load sensor and indenter**

To investigate the effects of load, temperature and strain rate, different testing conditions were selected for the indentation tests. Tests were performed at four different temperatures, 25, 60, 100 and 150 ℃ . Upon increasing the temperature to 60 and 100 $^{o}$C, various phenomena such as increase in the transformation stress can happen, and these phenomena can alter the deformation characteristics of superelastic TiNi under indentation. Also, it is expected that 150 $^{o}$C is above $M_d$ and hence no superelasticity would exist in this temperature region.

In this scenario, three different strain rates were chosen to ascertain the effects of strain rates on the deformation behaviour of superelastic TiNi under localized compressive loads. Three different loading rates leading to different strain rates were used for the indentation tests; the loading rates included were 1, 10 and 20 N.min$^{-1}$. All tests were conducted using maximum loads of 20, 40, 60, 80 and 100 N. Normal force and depth were recorded and saved every 0.5 seconds using the UMT software.

In order to compare the indentation behaviour of superelastic TiNi with other conventional materials, AISI 304 steel was also tested at room temperature, with slow, medium and high strain rates with both sharp and spherical indenter and using maximum loads, similar to superelastic TiNi.

Each indentation test was repeated at least three times in order to assure reproducibility of data. Table 3.3 provides a summary of indentation tests conditions.

**Table 3.3 - Indentation tests conditions**

| Sample | Temperature ($^{o}$C) | Max Load (N) | Loading Rate (N.min$^{-1}$) | Indenter Tip |
|---|---|---|---|---|
| superelastic TiNi | 25, 60, 100, 150 | 20, 40, 60,80,100 | 1, 10, 20 | Spherical, Sharp |
| 304 Steel | RT | | | |

# CHAPTER 4 RESULTS AND DISCUSSION

## 4.1 Tensile Tests

### 4.1.1 Materials Assessment

The transformation temperatures of both shape memory and superelastic TiNi samples without any external forces can be obtained from DSC results. In order to make sure the accuracy of DSC results, the test was performed twice on tensile samples. The results were quite similar, and the representative of DSC spectrograms is given in Figure 4.1. The intersection points between the curve tangents of endothermic and exothermic peak and the base line represent austenitic and martensitic transformation temperatures, respectively. Transformation temperatures are extrapolated from Figure 4.1 and given in Table 4.1.

The superelastic TiNi specimen shows two endothermic peaks near -5 and 7°C in the heating cycle, corresponding to the R-phase and austenite transformation temperatures, respectively. The austenite start temperature is about 4 °C while the austenite finish temperature is about 10 °C. As well, two exothermic spikes near 4 and −22°C appear in the cooling cycle. They represent the R-phase and martensite transformation temperatures, respectively. The R-phase is an intermediate phase with trigonal crystal structure which forms during martensitic transformation, before the formation of the martensite phase. For the shape memory alloy, there is an endothermic peak around 84°C in the heating cycle and an exothermic peak around 48°C in the cooling cycle, corresponding to austenite and martensite formation temperatures, respectively.

Shape memory TiNi alloy showed one endothermic peak in the heating cycle, with an enthalpy of 30 J/ g, and two exothermic peaks in the cooling cycle, with their enthalpies adding up to just under 30 J/g. The discrepancy between cooling and heating cycles might be due to the peaks not being completely resolved.

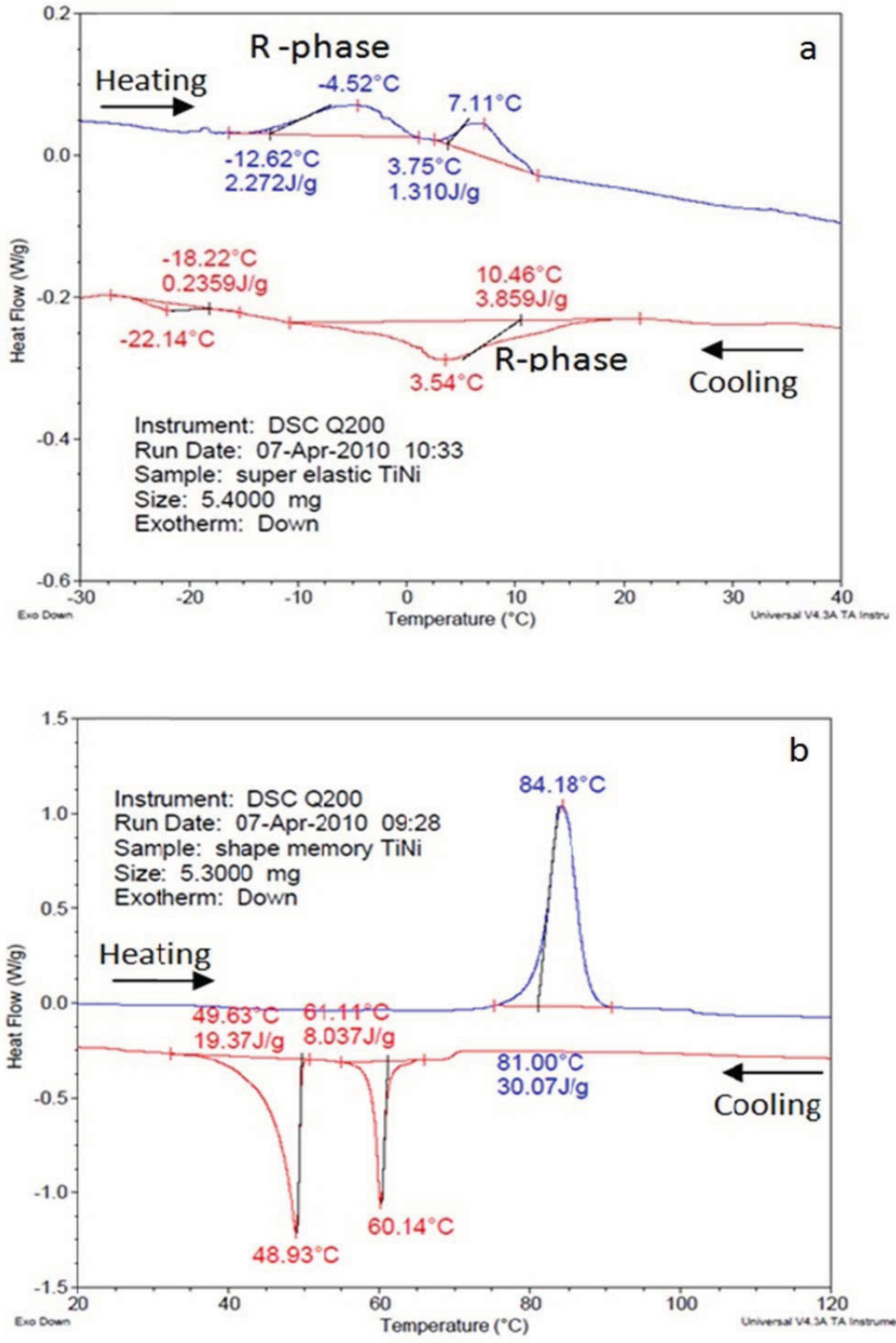


**Figure 4.1 - DSC spectrogram of (a) superelastic and (b) shape memory TiNi**

**Table 4.1 - Transformation temperatures of TiNi tensile specimens**

| Temperature (°C) / Materials | $M_f$ | $M_s$ | $A_s$ | $A_f$ |
|---|---|---|---|---|
| Superelastic TiNi | -24.5 | -18.22 | 3.75 | 11.5 |
| Shape memory TiNi | 45.65 | 48.93 | 81 | 86 |

### 4.1.2 Stress – Strain Curves

The stress-strain curves for superelastic TiNi specimens are illustrated in Figure 4.2. The curves exhibit a typical superelastic behaviour, i.e., a linear austenite elastic deformation, followed by a large recoverable deformation as a result of phase transition from austenite to martensite and martensite detwinning (plateau region in Figure 4.2). At the end of the plateau region, the detwinned martensite enters into an elastic/plastic deformation mode similar to conventional metals. Due to the superelasticity effect, a large amount of deformation can be recovered during unloading. Any unrecoverable deformation is a result of martensite plastic deformation.

As clearly depicted in Figure 4.2 the stress-strain behaviour of superelastic TiNi is strongly influenced by testing temperature, the error in testing temperature is ± 2 $^{o}$C. Upon heating, the required stress for the transformation of austenite to stress-induced martensite (SIM) increases. For example, the austenite-to-martensite transformation stress ($\sigma_{A\rightarrow M}$) increases from 250 MPa to 808 MPa as the testing temperature increases from 0 to 85 °C, as seen in Figure 4.2 and Table 4.2.

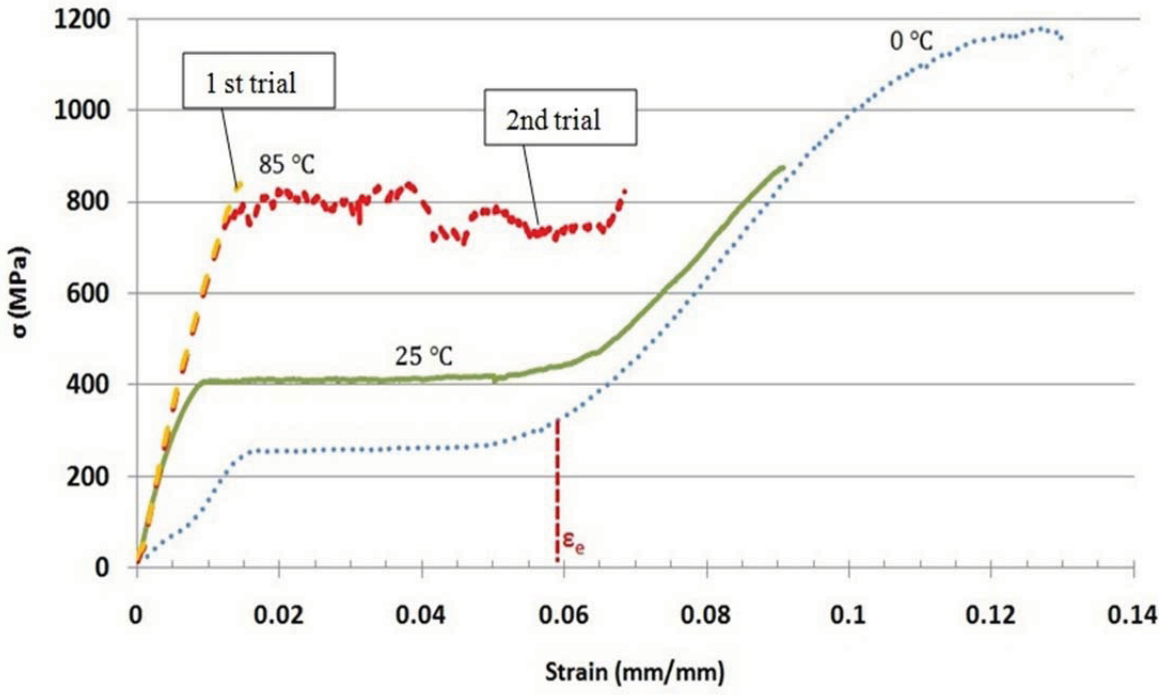


**Figure 4.2 - Stress-strain curves at three different temperatures for superelastic TiNi**

On the other hand, the elastic modulus of austenite ($E_A$) and the amount of recoverable strain ($\varepsilon_e$) do not exhibit any significant change with an increase in testing temperature (Table 4.2).

**Table 4.2 - Mechanical properties of superelastic TiNi alloy**

| Temperature ($^oC$) | $E_A$ (GPa) | $\sigma_{A \rightarrow M}$ (MPa) | $\varepsilon_e$(%) |
|---|---|---|---|
| 0 | 2 regions* | 256 | 5.5 |
| 25 | 66 | 410 | 5.5 |
| 85 | 69 | 808 | 6.0 |

*First region, $E_R$=18 GPa and second region $E_A$=25 GPa (combination of A and R-phase).

The tensile test at 85 °C for superelastic TiNi was repeated twice. In the first trial, the material reached its final fracture before entering into the plateau region. When the test was repeated in the second trial, the material showed a typical plateau region associated with superelasticity. It is believed that 85 °C testing temperature is within the temperature range where superelasticity is no longer operative ($M_d$). In the first trial ($T>M_d$), the TiNi behaved like conventional material and failed when the stress reached the failure stress of austenite. It is well established that, at a temperature above $M_d$, the austenite-to-martensite transformation will not take place. Instead, the austenite will deform plastically by slip because, above $M_d$ the stress required for slip is lower than that required for the austenite-to-martensite transition. Hence, at a temperature above $M_d$, TiNi behaves like conventional material and no superelastic effect is observed.

Furthermore, the stress-strain curve for superelastic TiNi generated at 0 °C clearly shows two initial linear regions in the elastic portion of the diagram. It is believed that the first section corresponds to the elastic deformation of the R-phase while the second section represents the elastic deformation of the austenite. As evident from the DSC data in Figure 4.1(a), the R-phase is present in the temperature range -10 to 10 °C. Therefore, it is expected that some R-phase would be present in the microstructure at 0 °C. This explains the presence of the double elastic regions in the superelastic TiNi tested at 0 °C (Figure 4.2 and Table 4.2). Table 4.2 gives the elastic moduli for both the R- and austenite phases. The measured elastic modulus of austenite is lower than that measured at 25 and 85 °C. This might be due to the contribution of the R-phase to the overall elastic deformation.

Although the shape of the stress-strain curves of shape memory TiNi (Figure 4.3) are similar to those of superelalastic TiNi (Figure 4.2), the deformation mechanisms are different in each case. Stress-strain curves for shape memory TiNi begin with a linear elastic deformation of twinned martensite, followed by a detwinning process accompanied by a large deformation at the “plateau” stress. The elastic deformation of martensite can be recovered upon unloading. However, deformation due to detwinning cannot be recovered during unloading, and thus heating would be required to induce recovery (shape memory effect).

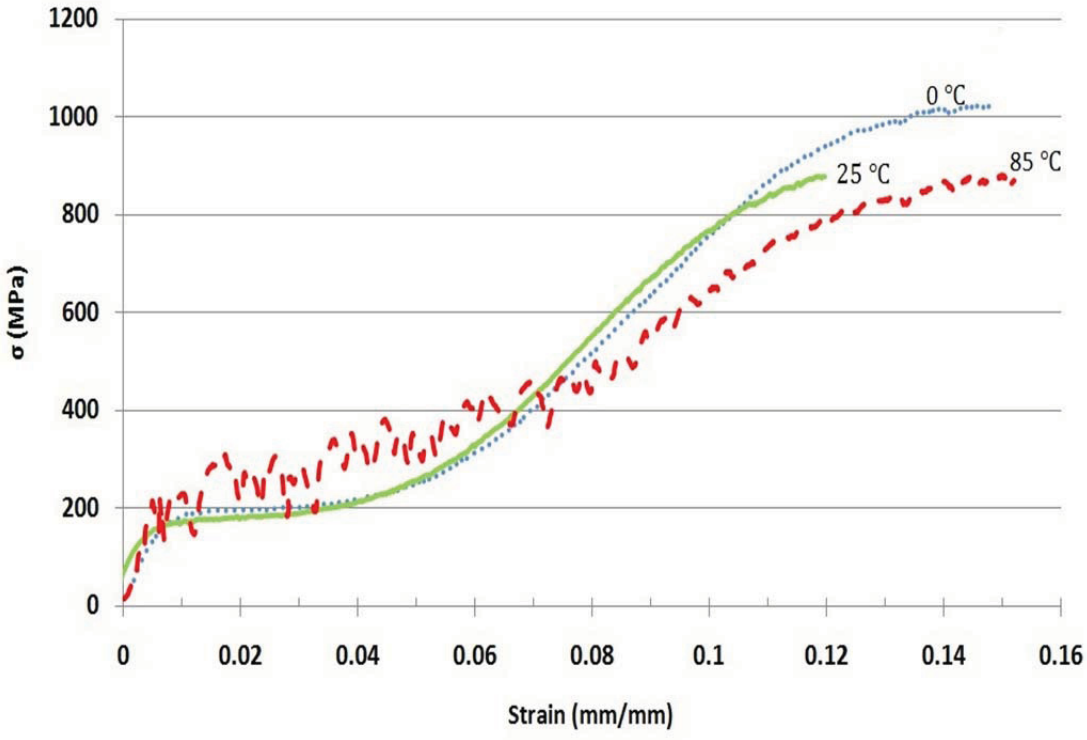


**Figure 4.3 - Stress-strain curves at three different temperatures for shape memory TiNi**

Table 4.3 gives elastic moduli ($E_M$), martensite detwinning stress ( ) and recoverable strain (ε) upon heating. The tensile properties for shape memory TiNi did not seem to significantly change with testing temperatures in the range 0-25 °C. However, at a testing temperature of 85 °C, it appears that both the elastic modulus and detwinning stress increased by 50% compared to a specimen tested at 0 °C. The elastic modulus for the 0 to 25 °C is believed to be that of martensite. At 85 °C, the material is expected to consist of both martensite and some austenite phase because the testing temperature is above $A_s$, as depicted in the DSC data (Fig. 4.1(b)). Therefore, the rise in the elastic modulus at 85 °C might be the result of the austenite phase contribution.

**Table 4.3 - Mechanical properties of shape memory TiNi alloy**

| Temperature ($^oC$) | $E_M$ (GPa) | $\sigma_{M(T) \rightarrow M(DT)}$ (MPa) | ε(%) |
|---|---|---|---|
| **0** | 23 | 200 | 4.5 |
| **25** | 21 | 187 | 4.5 |
| **85** | 32* | 300 | 5.5 |

*Combination of austenite and martensite.

#### 4.1.2.1 Cyclic Tensile Tests

Cyclic tensile tests have been performed for both shape memory and superelastic TiNi samples at room temperature. Recoverable strain and reverse transformation stress for superelastic specimens can be calculated from the cyclic stress-strain curves. In order to generate the stress vs. temperature curve of superelastic TiNi, the stress induced martensite-to-austenite transformation stress at room temperature must first be determined.

Cyclic stress-strain curves of superelastic and shape memory TiNi alloys are illustrated in Figure 4.4 (a) and 4.4 (b), respectively. According to Figure 4.4 (a), the generated strain is fully recovered after the second unloading cycle. The superelastic sample test was carried out for 3 cycles and the specimen unloaded within the stress plateau region. Due to superelastic effect, the entire elongation completely recovered its original shape during the first and second cycles; however, at the 3$^{rd}$ cycle the specimen fractured. It is observed from Figure 4.4 (a) that $\sigma_{A \rightarrow M}$drops from 415 MPa in first cycle to 370 MPa in second cycle; this is followed by a drop to 360 MPa in third cycle. Furthermore, the reverse transformation stress $\sigma_{M \rightarrow A}$ drops from 180 MPa in the first cycle to 170 MPa in the second cycle.

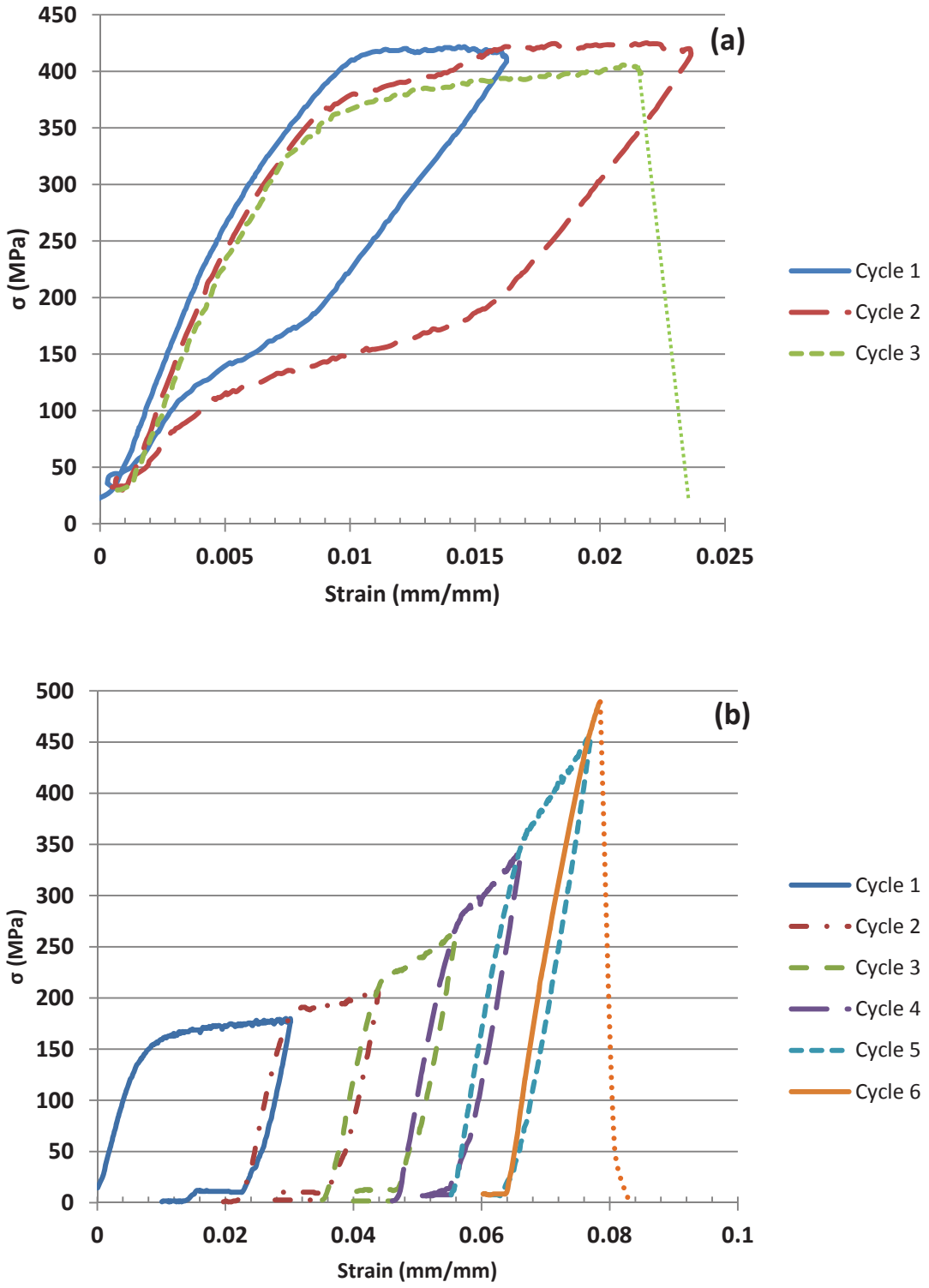


**Figure 4.4 - Cyclic stress – strain curves of (a) superelastic and (b) shape memory TiNi alloy**

The reduction in the plateau stress with number of cycles is due to the formation of small amounts of localized slip during cyclic loading which facilitates the austenite-to-martensite transformation; it leads to lower plateau stress in the stress-strain curve [89-91]. This can impose implication in dynamic mechanical systems as the expected transition stress changes with cycles of operation. Conversely, the generated strain did not recover after unloading the shape memory TiNi sample (Figure 4.4 (b)). Nevertheless, its elongation was recovered by heating.

Based on data collected from Figure 4.4 and the data obtained from DSC tests (Table 4.1) (transformation temperatures at zero external load) for superelastic TiNi, Figure 4.5 was constructed. The figure shows the reversible martensitic transformation temperatures at different stress levels. According to this diagram, the transformation stress increases with increasing temperatures due to an increase in the transformation energy barrier [92]. This diagram is consistent with well-established literature [1].

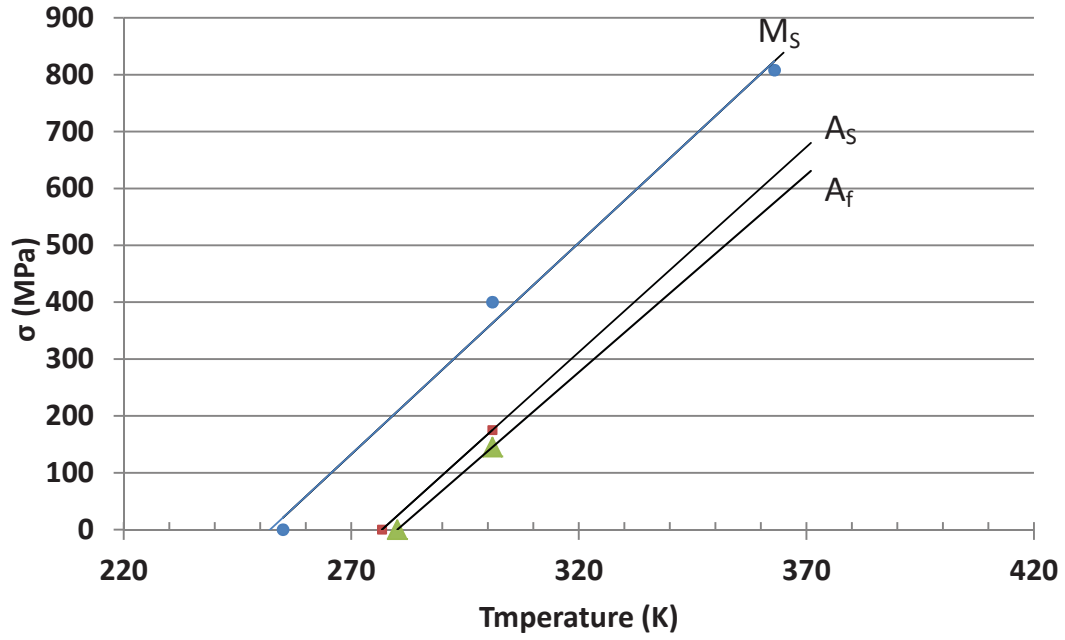


**Figure 4.5 - Transformation stress as a function of temperature curve of superelastic TiNi alloy**

### 4.1.3 Simultaneous Heating and Loading during Tensile Tests

#### 4.1.3.1 Superelastic TiNi

In order to assess the effect of increasing temperature during loading, the superelastic TiNi specimen was heated to approximately 85 ℃ in the plateau region. Figure 4.6 illustrates the related stress-strain curve, where a sudden increase in the stress level followed by early fracture was observed. The curve reflects the high sensitivity of the mechanical properties of superelastic TiNi to changes in working temperature. In order to explain this sudden rise in stress, in-situ experiments were carried out as described below.

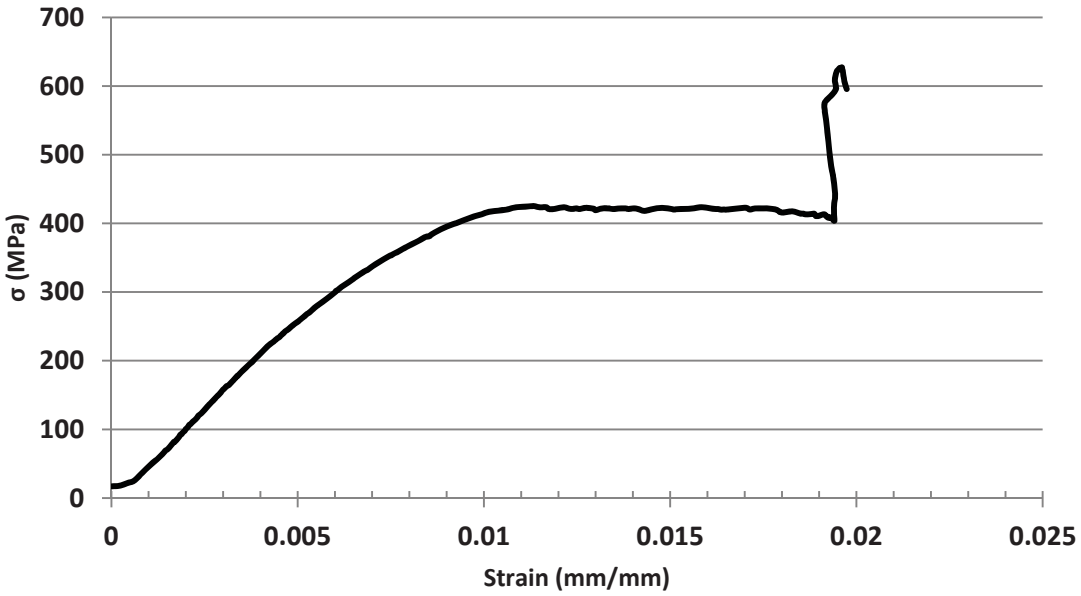


**Figure 4.6 - Effect of heating superelastic sample in the plateau stress region**

In-situ tests under an optical microscope were carried out to observe microstructural and mechanical properties evolutions during simultaneous loading and heating in the plateau region of the stress-strain diagram. During the tests, the specimen was subjected to short heating intervals within the plateau region of the curve. The heating temperature was selected at 85 °C to induce martensite-to-austenite transformation. The stress-strain curve and the microstructural features of superelastic sample are given in Figures 4.7 and 4.8.

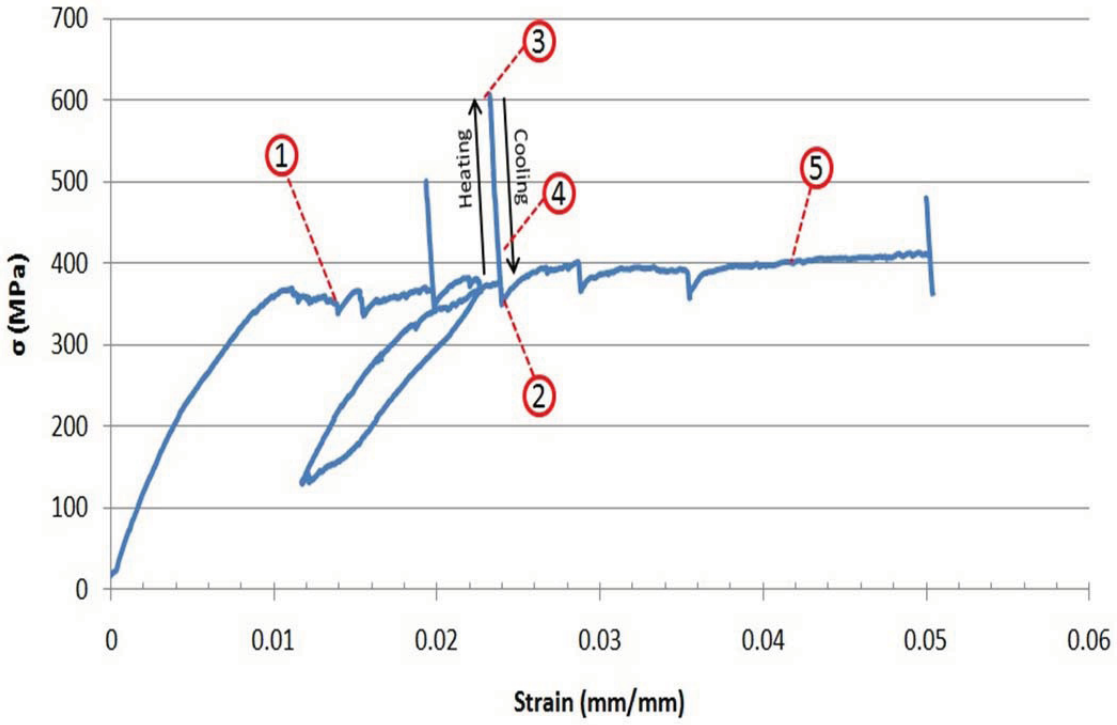


**Figure 4.7 - In-situ stress-strain curve of superelastic TiNi interrupted by heating/cooling periods**

The point on the stress-strain diagram labelled "1" is at the beginning of the austenite-to-martensite transformation. The micrograph labelled "1" in Figure 4.8 corresponds to the microstructure at point "1" and reveals the austenite phase. It was noticed that the stress-induced martensite nucleated at random locations in the gage section of the tensile sample and subsequently grew to cover the whole section. At point "2" on the stress strain curve, however, the microstructure consists of both austenite and martensite, as seen in the micrograph labelled "2" in Figure 4.8. Here, the martensitic phase has nucleated within the austenite phase and formed bands at 45° angles from the tensile axis. Furthermore, the martensite phase shows a rough topography as compared to the austenite phase. Note that, in Figure 4.8, "A" and "M" refer to austenite and martensite phases, respectively.

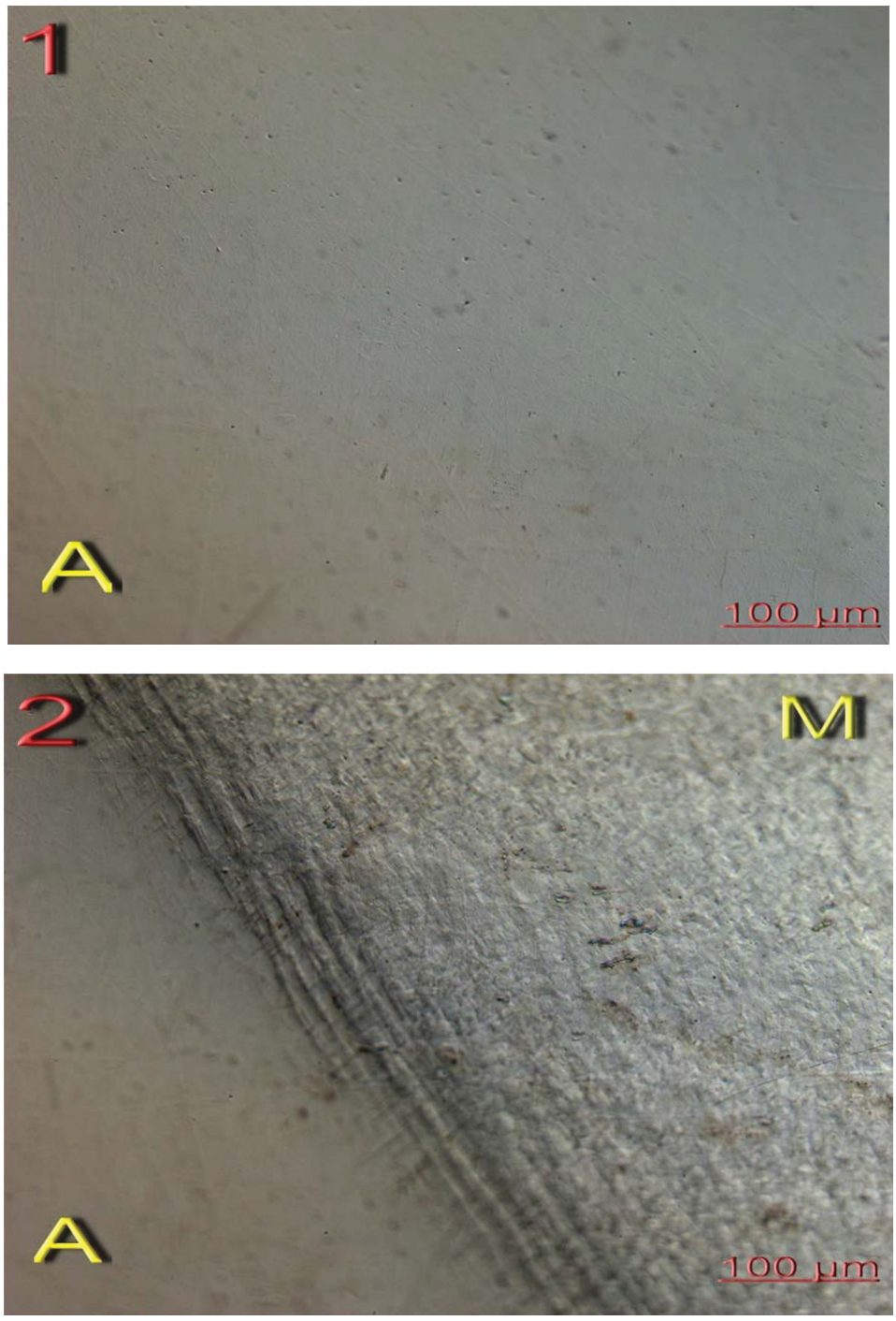


**Figure 4.8 - Optical microscopy images of the microstructural evolution of superelastic TiNi during tensile testing while subjected to heating and cooling periods.**

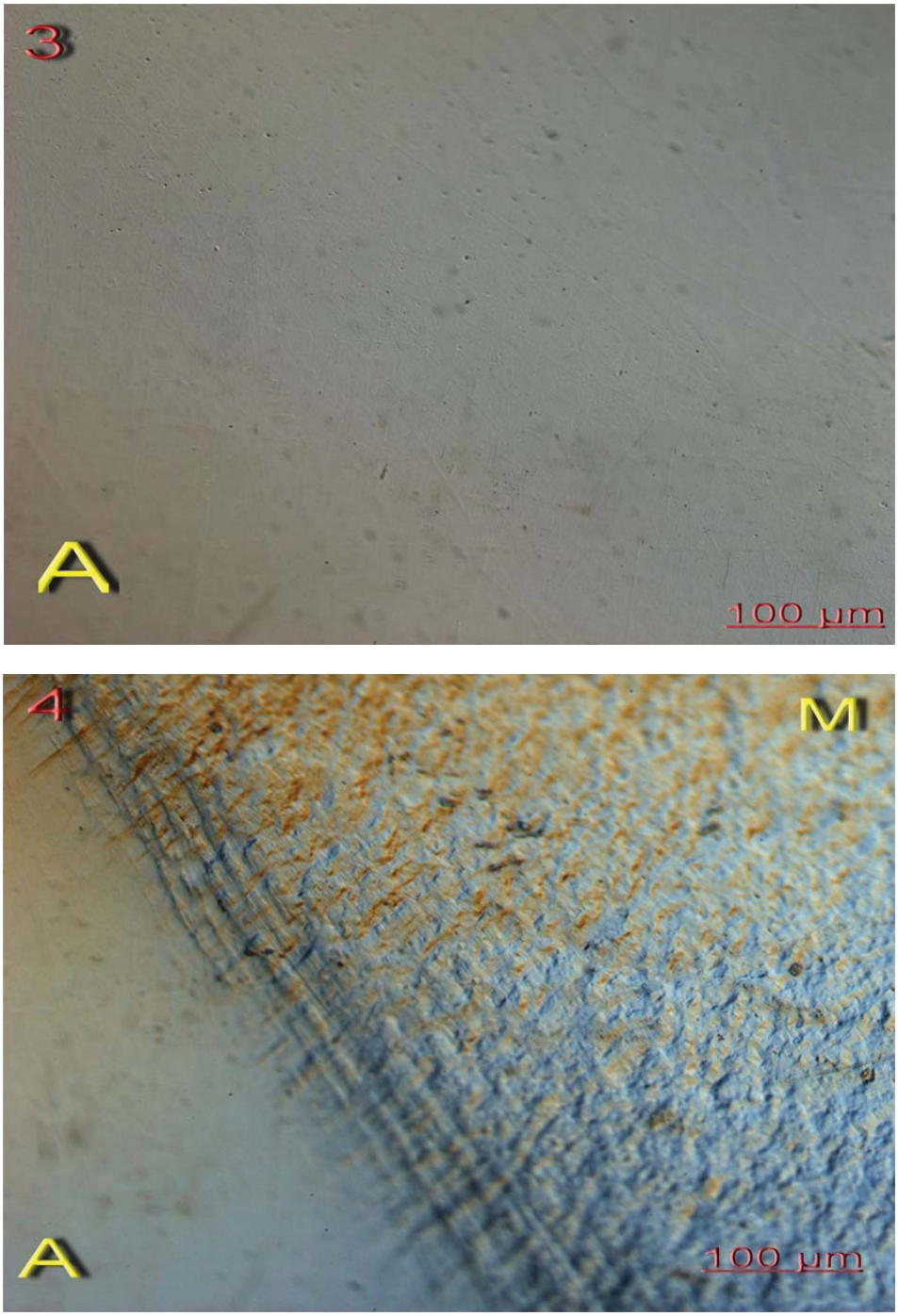


**Figure 4.8 - Continued, optical microscopy images of the microstructural evolution of superelastic TiNi during tensile testing while subjected to heating and cooling periods.**

When the specimen was heated to 85 °C, a sudden increase in the stress level was observed. At the same time, the martensite in the microstructure was transformed to austenite (Figure 4.8 “3”). Since the stress needed to stretch austenite at this strain is higher than that of martensite, and since the specimen was constrained in the tensile tester (i.e., specimen was prevented from contracting), the transformation was accompanied by a rapid increase in stress. Then, as the specimen was cooled to room temperature, the stress decreased to its pre-heating level and the microstructure transformed back to martensite, as shown in micrograph “4” in Figure 4.8. The heating/cooling cycle can be seen in Figure 4.7 and 4.8, labelled as “2”, “3” and “4”. This observation has substantial implications for real-life situations, as overheating to above the martensite-to-austenite transformation temperature may lead to a sudden increase in stress levels and thus could potentially result in total failure of the superelastic TiNi component.

Figure 4.9 shows how the stress-induced martensite nucleates at random locations in the gage section of the tensile sample during loading, and how different martensite bands expand until the whole sample becomes martensitic at the end of stress plateau (point 5 in Figure 4.7)

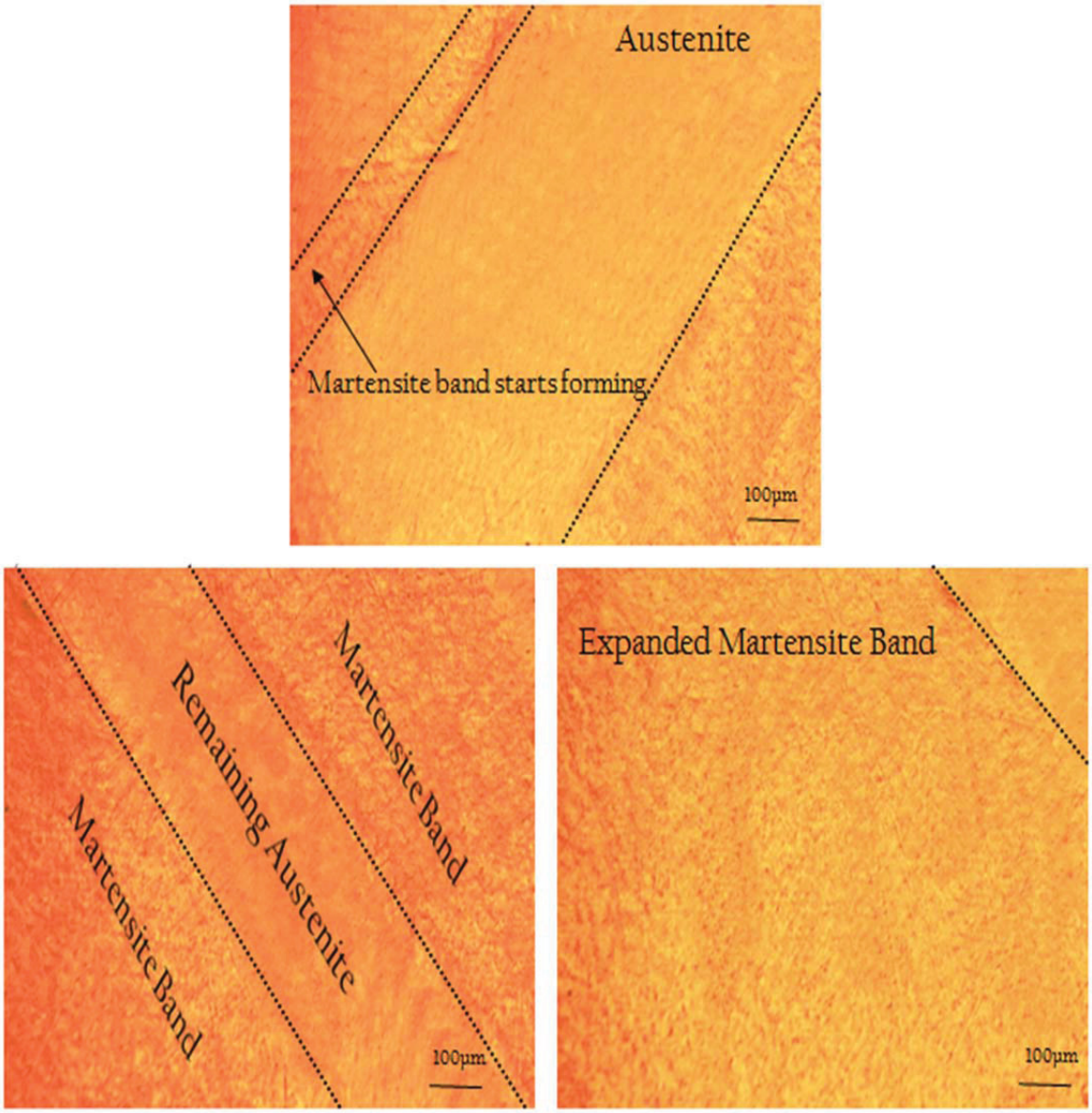


**Figure 4.9 - Nucleation of different martensite bands in random regions at a 45° angle from the tensile axis**

#### 4.1.3.2 Shape Memory

According to the DSC results, the austenite start temperature ($A_s$) for the shape memory sample (at zero load) is about 84 °C, and this temperature increases when the sample is under tension (Figure 4.5). Hence, by heating the shape memory alloy during tensile testing to about 85 °C, no transformation would be expected to take place. As evident in Figure 4.10, heating the shape memory TiNi specimen during tensile testing, in the

plateau region, leads to a sudden but slight drop in the stress level. This is attributed to softening and thermal expansion of the specimen. Micrograph "1" in Figure 4.11 shows twinned martensite at the early stages of detwinning. Upon further stretching of the specimen, the topography of the surface becomes rougher as a result of detwinning (Figure 4.11 "2"). When the specimen was heated at point "3", the stress level suddenly dropped but no change in the microstructure was observed.

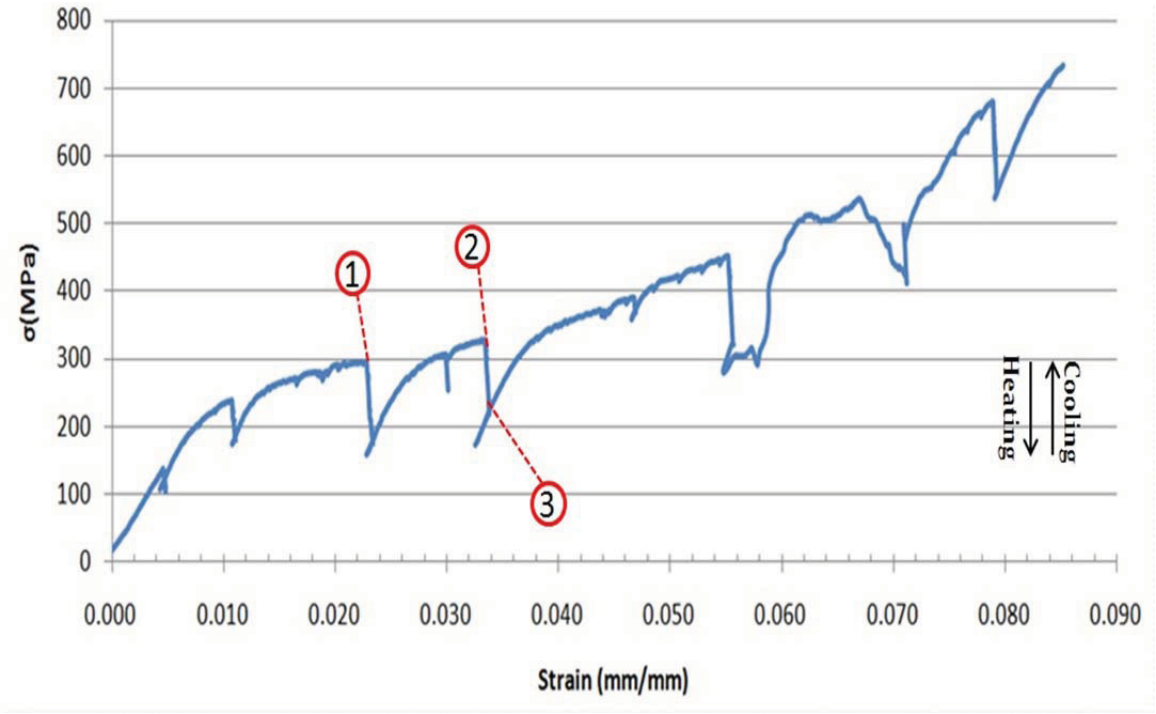


**Figure 4.10 - In-situ stress-strain curve of shape memory TiNi interrupted by heating/cooling periods**

In order to ensure that the decrease in stress level due to heating of the sample during the tensile test is not a result of phase transformation in a TiNi alloy, a similar tensile test was performed on brass. The stress level was reduced when the material was subjected to heating (Figure 4.12), confirming that softening and thermal expansion are responsible for stress level reduction (similar to shape memory TiNi sample, Figure 4.10).

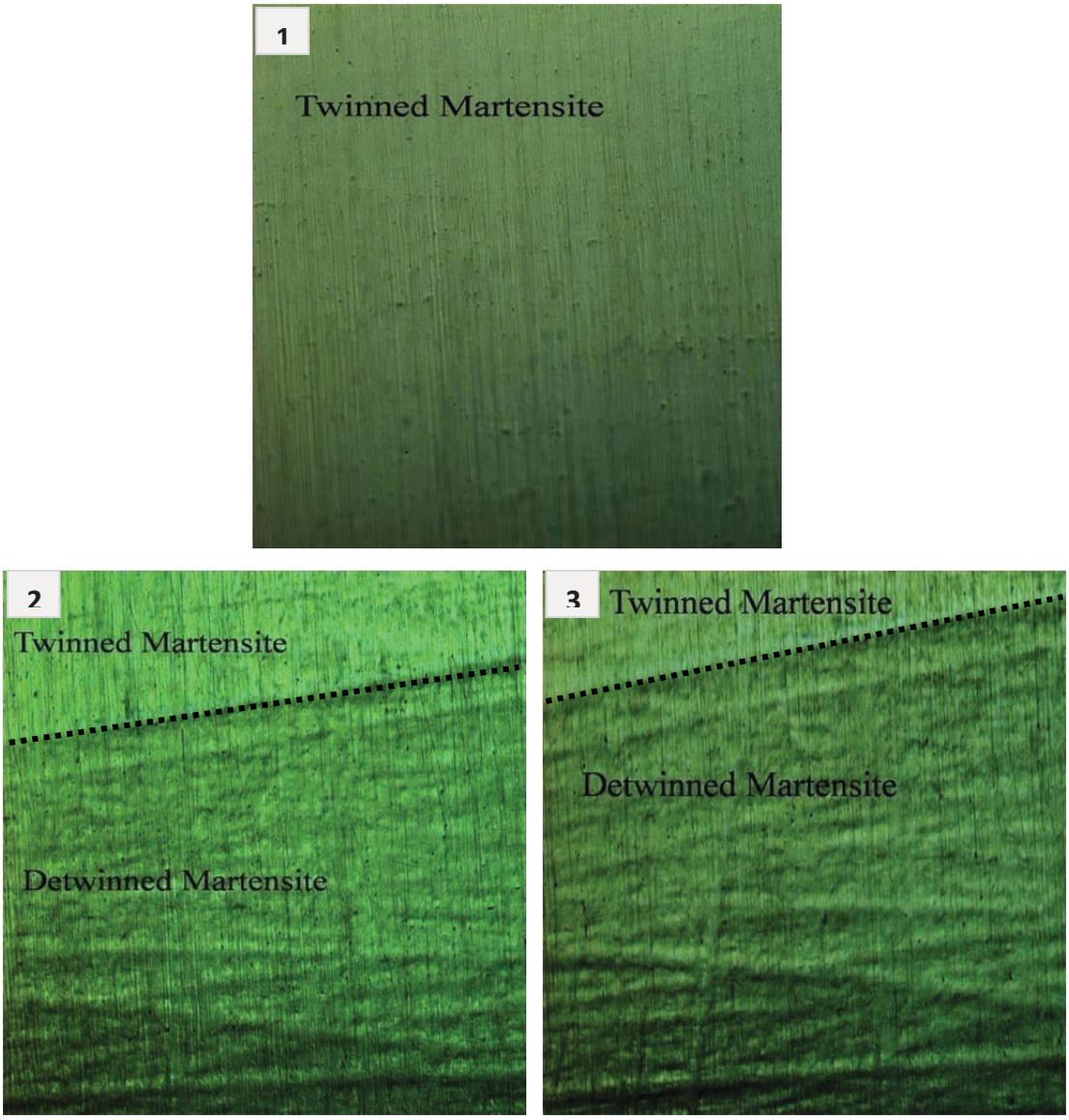


**Figure 4.11 - Optical microscopy images of microstructural evolution of shape memory TiNi during tensile testing while subjected to heating and cooling periods.**

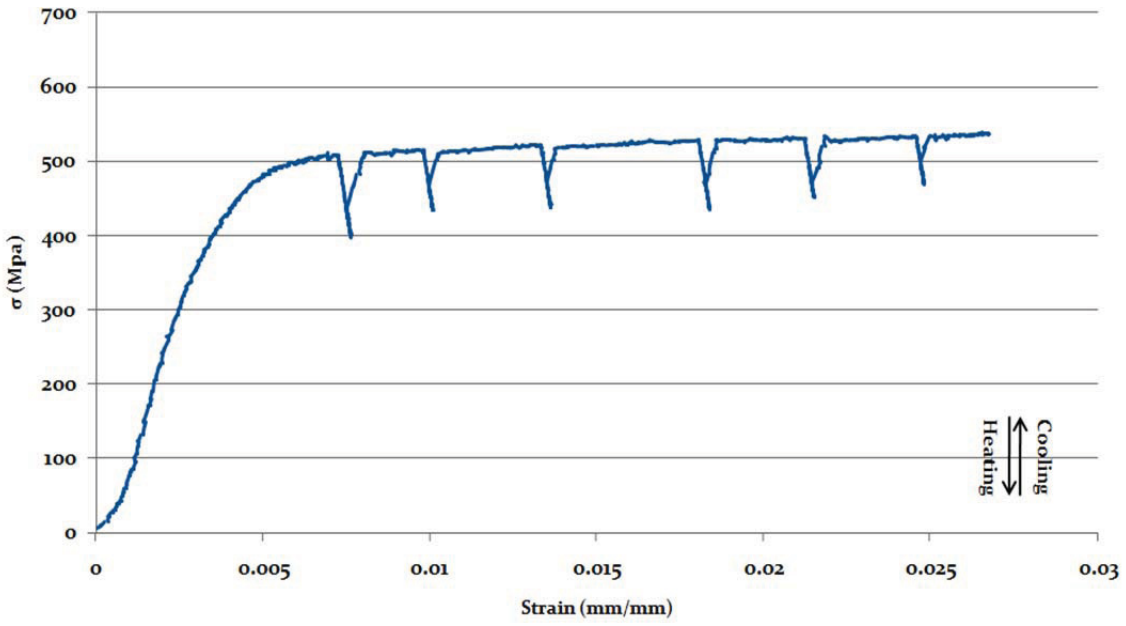


**Figure 4.12 - In-situ stress-strain curve of brass interrupted by heating/cooling periods**

## 4.2 Indentation Tests

### 4.2.1 Materials Assessment

The transformation temperatures of superelastic indentation sample were determined by conducting DSC test. From the endothermic peak on the heating cycle near 5.5 °C the austenite start ($A_s$) and finish ($A_f$) transformation temperatures are determined to be -3.5 and 9 °C, respectively. The exothermic spike in the cooling cycle at around -0.12 °C which correspond austenite-to-martensite transformation has martensite start ($M_s$) and finish ($M_f$) transformation temperatures of 5.87 and 6.25 °C, respectively. Hence, at ambient temperatures, the austenite phase would be stable. Figure 4.13 presents a spectrogram of the DSC curve for the superelastic TiNi indentation sample. As well, all the transformation temperatures are given in Table 4.4.

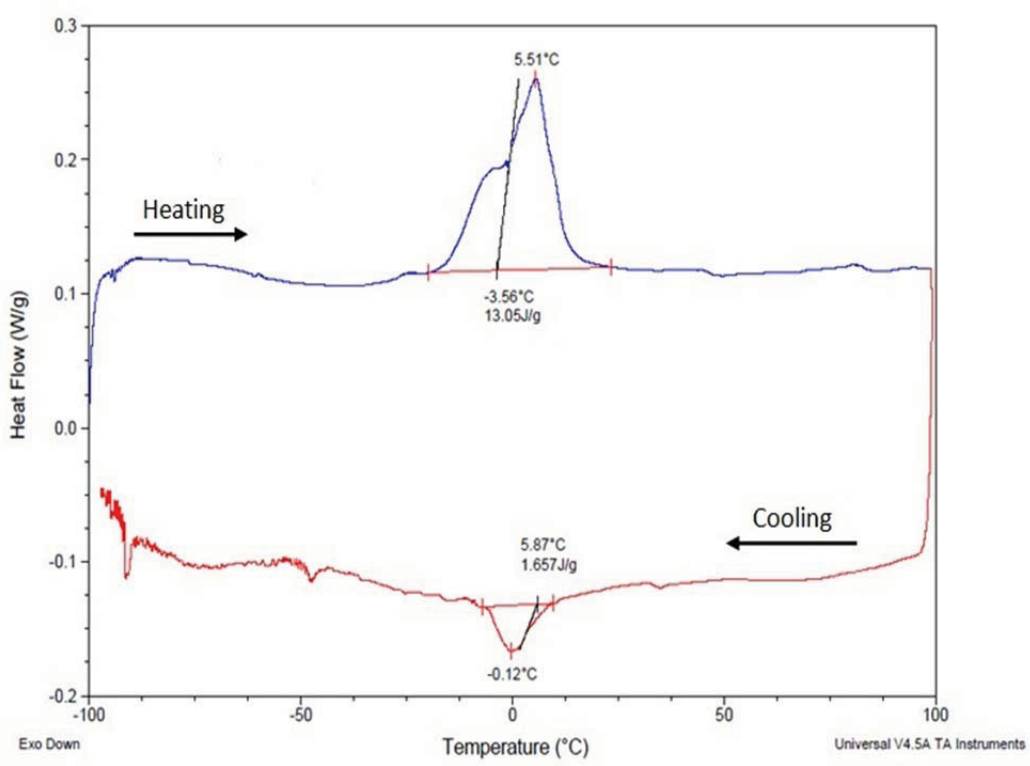


**Figure 4.13 - DSC spectrogram of superelastic TiNi indentation sample**

**Table 4.4 -Transformation temperatures of superelastic TiNi indentation**

| Temperatures ( ) / Materials | $M_f$ | $M_s$ | $A_s$ | $A_f$ |
|---|---|---|---|---|
| Superelastic TiNi | -6.11 | 5.87 | -3.56 | 7.46 |

Further confirmation of phases that exist at room temperature for indentation samples comes from the XRD pattern shown in Figure 4.14. The XRD pattern was identified as a mixture of martensite (with monoclinic crystal structure) and austenite (with cubic crystal structure) phases; however, the strongest peaks are austenite, which indicates the presence of the austenite phase at room temperature and, consequently, superelastic behaviour is expected.

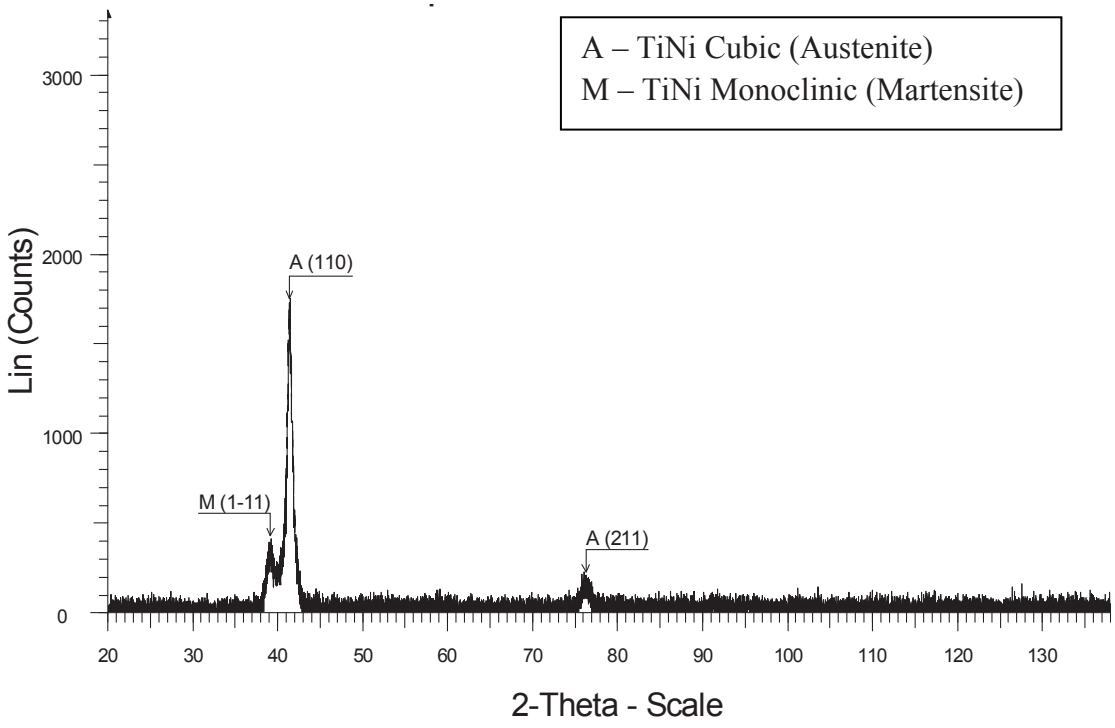


**Figure 4.14 - XRD pattern of superelastic TiNi**

An optical micrograph of a superelastic TiNi indentation sample depicting its microstructure is shown in Figure 4.15. Superelastic TiNi has a uniform equiaxed grain structure, with an average grain size of 30 μm.


**Figure 4.15 - Microstructure of as-received superelastic TiNi**

### 4.2.2 Spherical Indenter

Loading and unloading curves (load vs. depth) were plotted at various temperatures and strain rates. As it has been mentioned before, each test was repeated at least three times to ensure accuracy of the results and reproducibility of data. The error in measurements is no more than 5%. Representative curves at each condition were selected in order to compare indentation results; the following curves compare the loading and unloading behaviour of superelastic TiNi at constant strain rate and constant maximum load at different temperatures.

The curves in Figures 4.16 – 4.19 represent typical load vs. depth patterns. It is evident from the figures that deformations have fully recovered during unloading as a result of elastic and superelastic behaviour. It is also clear that loading and unloading follow the same path with no evidence of plastic deformation. For a given temperature and load application rate, the maximum load does not seem to have an effect on the trend and shape of load vs. depth curves except that higher maximum loads results in deeper indentation. This observation is consistent with well-established literature on indentation theory and contact mechanics [70, 71].

The load vs. depth curves in these figures, in general, show a rapid rise in indentation depth with increasing normal load followed by gradual increase in depth with rising load (represented by the change in the slope of load vs. depth curves). This can be attributed to ease of elastic deformation of material near the surface followed by high resistance to elastic deformation deep in the material and away from the surface. This effect is less pronounced at higher temperatures, for example, the change in slope of load vs. depth for indentation performed at 60 $^{o}$C is less evident than that at 25 $^{o}$C (Figure 4.16 (a)). This is because of lower resistance to elastic deformation of higher temperatures.

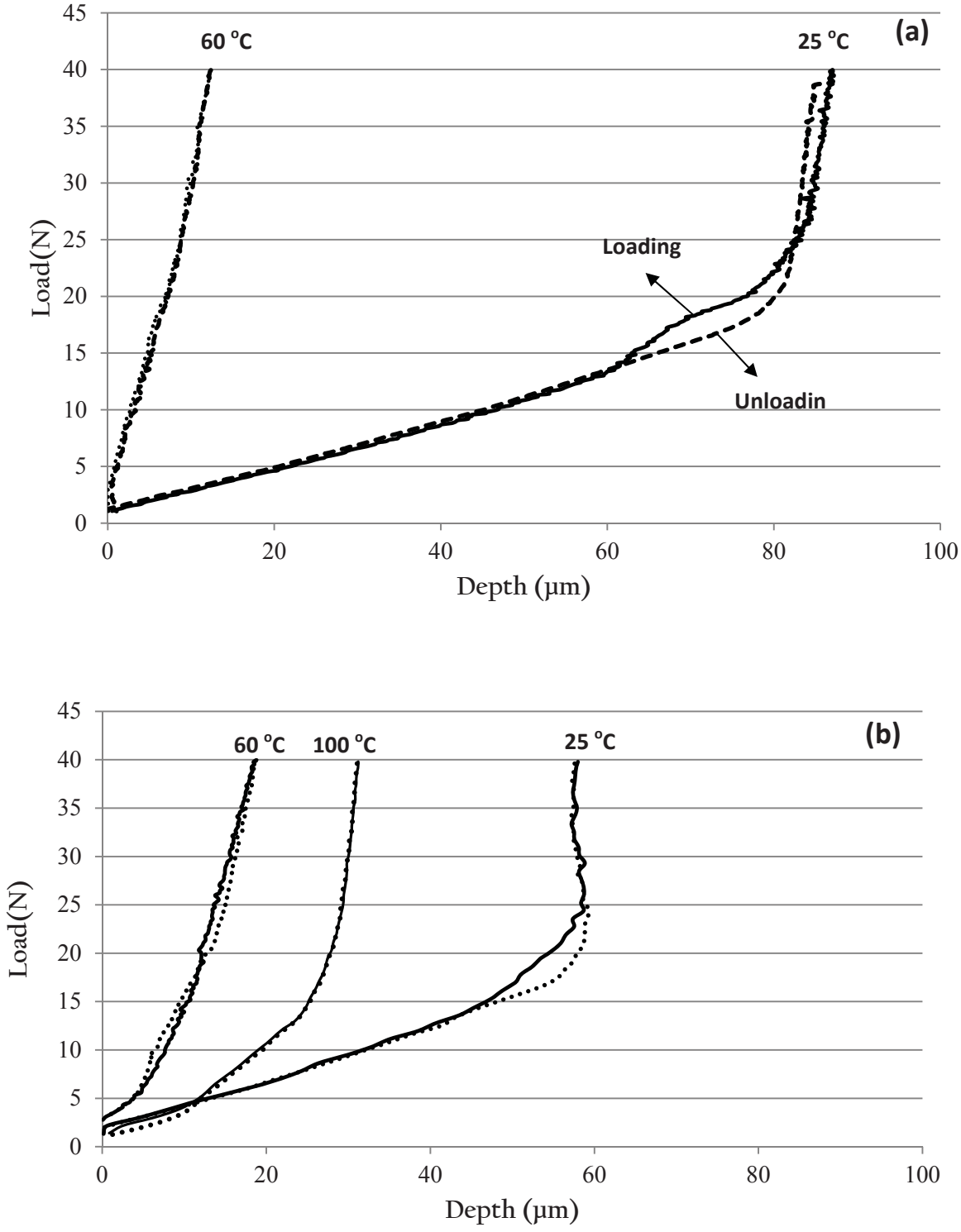


**Figure 4.16 - Loading - unloading curves of superelastic TiNi under maximum load of 40 N, various temperature and load application of (a) 1N.min$^{-1}$, (b) 10 N.min$^{-1}$**

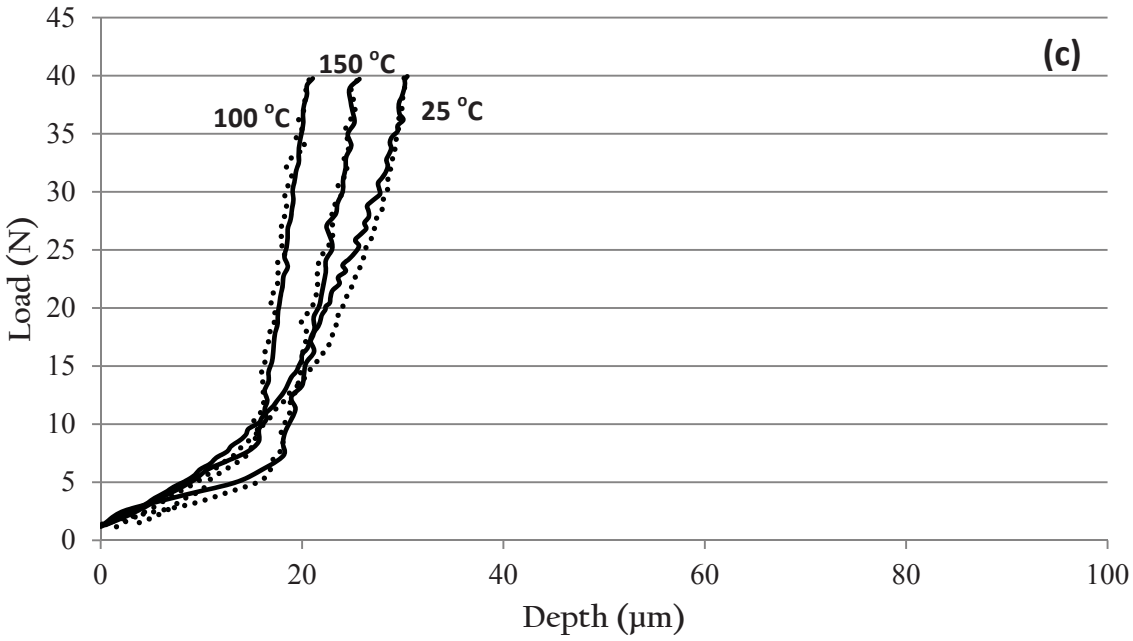


**Figure 4.16 - Continued, loading - unloading curves of superelastic TiNi under maximum load of 40 N, various temperature and load application of (c) 20 N.min$^{-1}$**

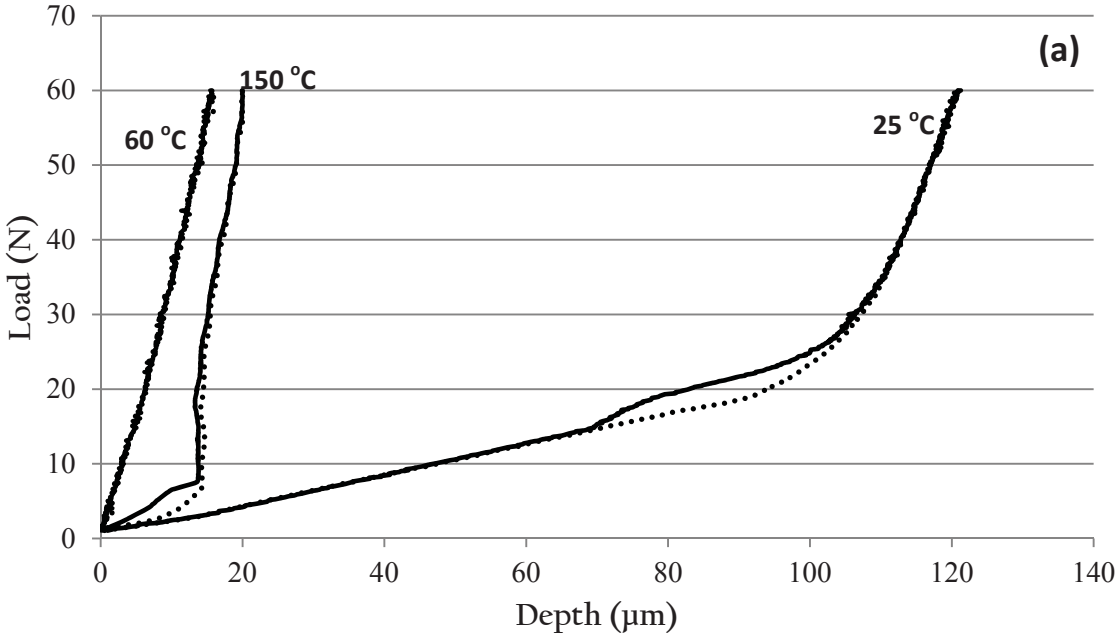


**Figure 4.17 - Loading - unloading curves of superelastic TiNi under maximum load of 60 N, various temperature and load application of (a) 1N.min$^{-1}$**

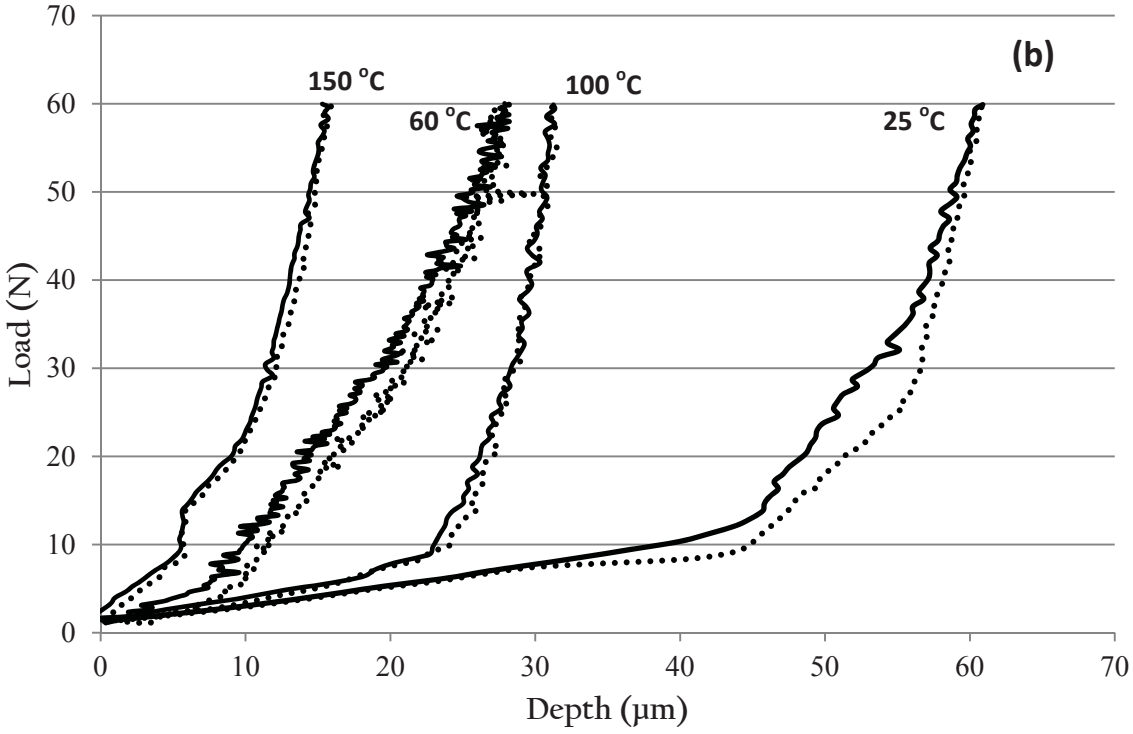


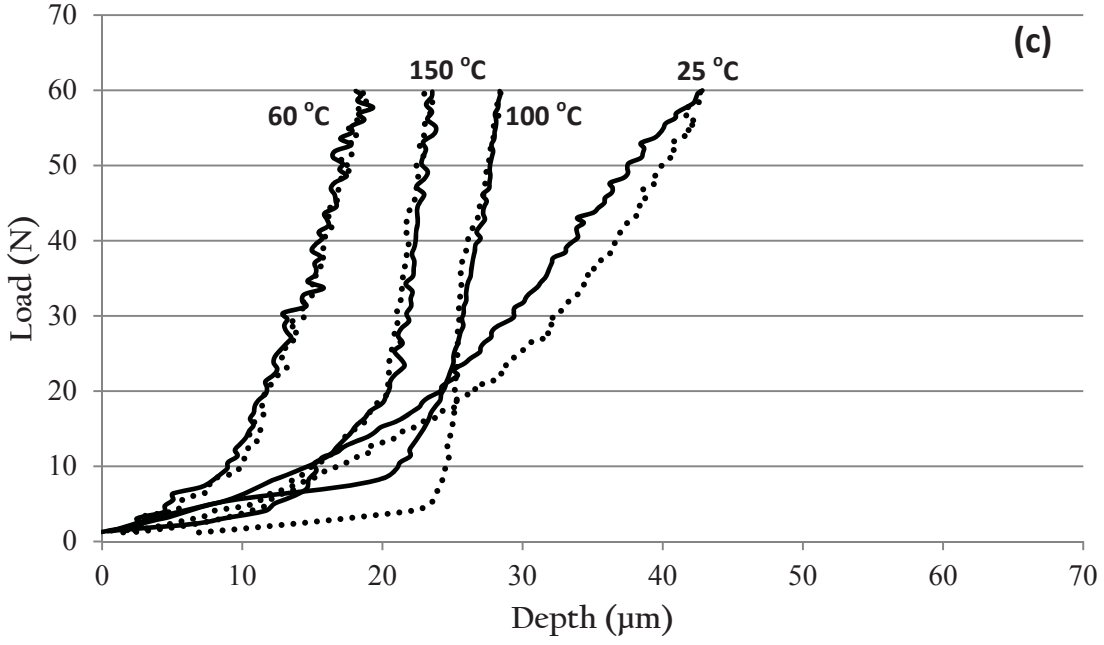


**Figure 4.17- Continued, Loading - unloading curves of superelastic TiNi under maximum load of 60 N, various temperature and load application of (b) 10N.min$^{-1}$ and (c) 20 N.min$^{-1}$**

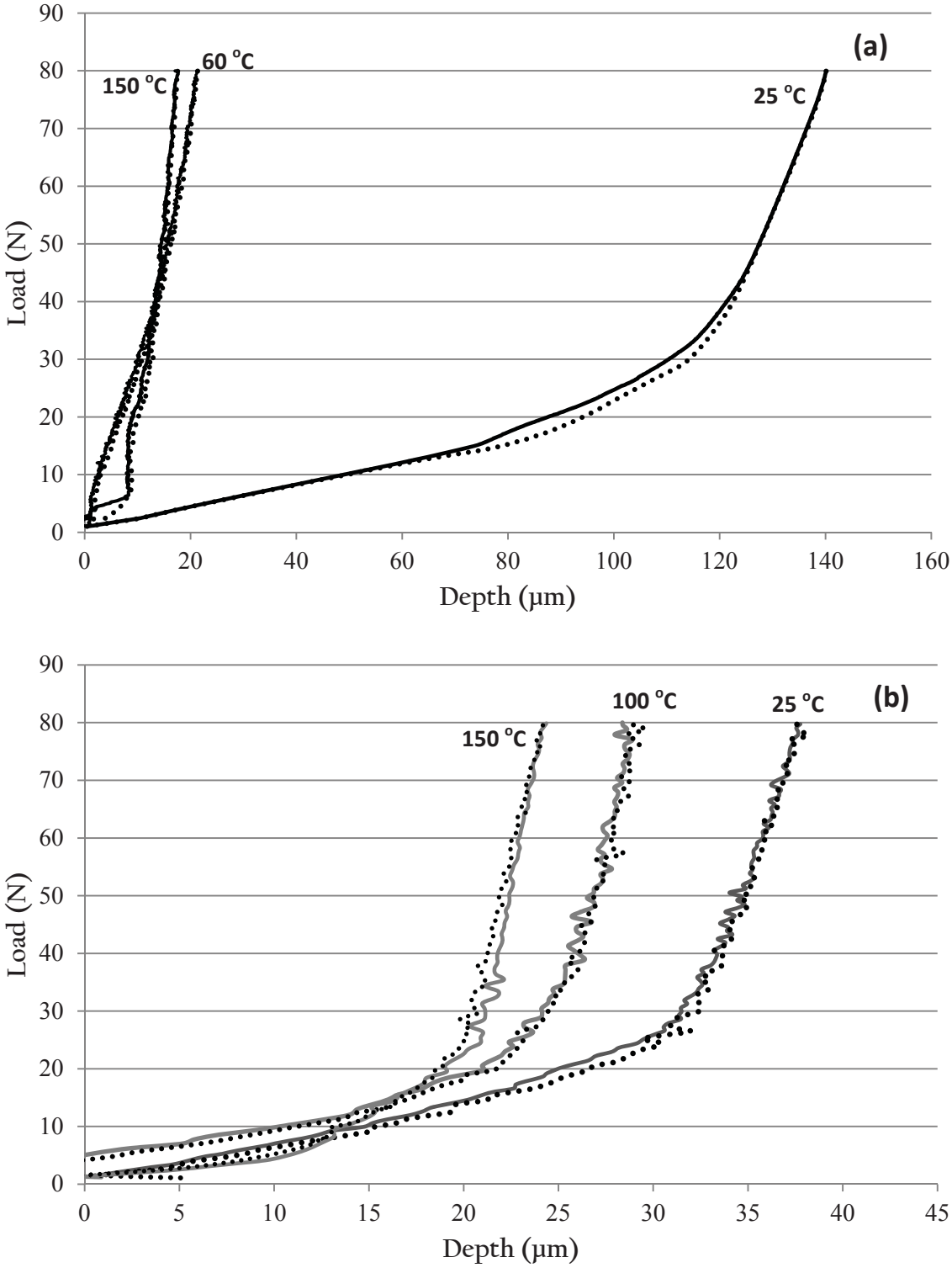


**Figure 4.18 - Loading - unloading curves of superelastic TiNi under maximum load of 80 N, various temperature and load application of (a) 1N.min$^{-1}$ and (b) 20 N.min$^{-1}$**

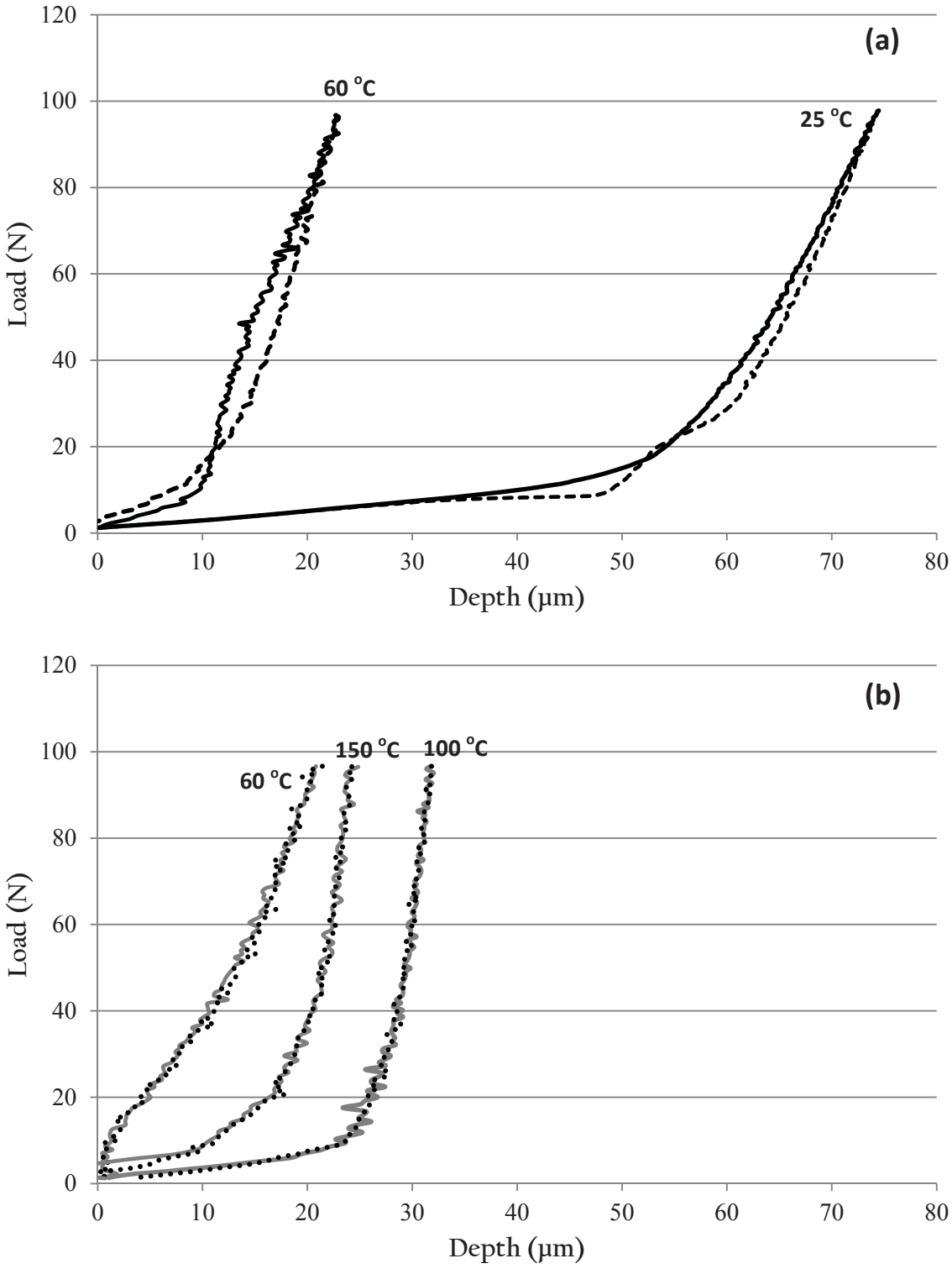


**Figure 4.19 - Loading - unloading curves of superelastic TiNi under maximum load of 80 N, various temperature and load application of (a) 10N.min$^{-1}$and (b) 20 N.min$^{-1}$**

In order to investigate the effects of temperature and strain rates on the deformation characteristics of superelastic TiNi under a spherical indenter, maximum load vs. maximum depth curves were plotted at all temperatures and strain rates. Maximum load and maximum depth (as representatives of the deformation of superelastic TiNi samples under localized compressive loads) was measured from the loading-unloading curves with the accuracy of ± 5 %.

Figure 4.20 shows a maximum load vs. maximum depth diagrams at the low strain rate for various temperatures. According to this diagram, the superelastic TiNi has undergone heaviest deformation at room temperature. Furthermore, there is a significant difference between deformation at room temperature and at high temperatures (60 and 150 $^{o}$C) at low strain rate. For example, room temperature deformation is seven folds that at 60 and 150 $^{o}$C. This behaviour is contrary to expectations in conventional materials, as heating is expected to induce more deformation.

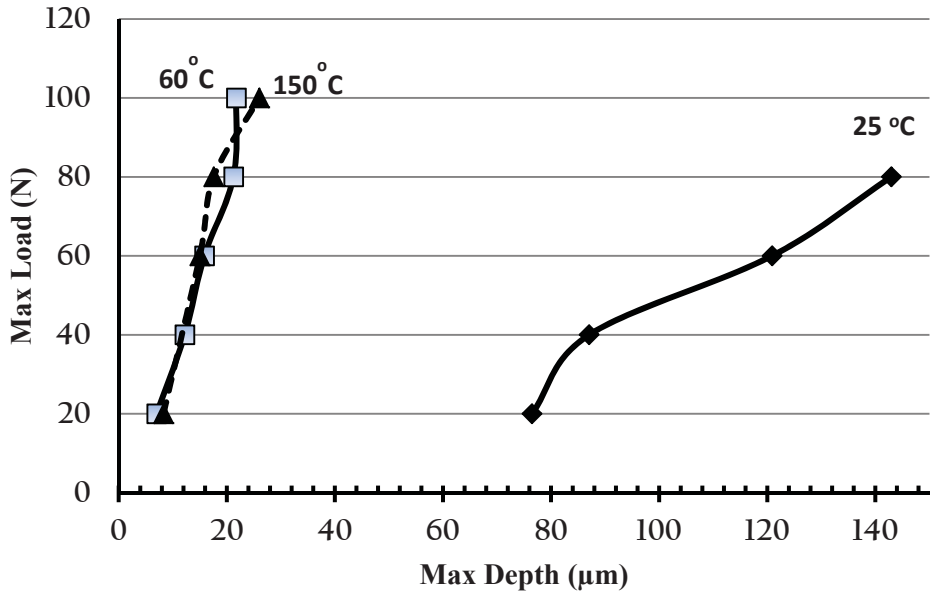


**Figure 4.20 - Max load vs. max depth of indentation tests at low strain rate (loading rate of 1 N.min$^{-1}$)**

A reduction in the deformation of superelastic TiNi at higher temperatures under loads can be attributed to one of two reasons. The first involves the increase in the required stress in starting martensitic transformations at a higher temperature, as austenite is thermodynamically more stable and higher stress is required to induce the austenite to martensite transformation. The second is that, the testing temperature is above the superelastic temperature limit ($M_d$) at which the austenite-to-martensite transformation will not take place. Above $M_d$, the austenite will deform plastically by slip, as the stress required for slip is lower than that for austenite-to-martensite transformation stress.

Thus, it can be deduced from the above discussion and Figure 4.20 that under indentation load superelasticity is only operative at 25 $^{o}$C. At 60 and 150 $^{o}$C transformation did not take place and deformation occurred in the austenite phase.

Similar results were obtained for indentations carried out at higher load application rate (i.e., strain rate) of 10 and 20 N.min$^{-1}$ as seen in Figures 4.21 and 4.22. However, the difference between deformation at room temperature and high temperature is gradually reduced by increasing the strain rate. The effect of strain rate is discussed further below.

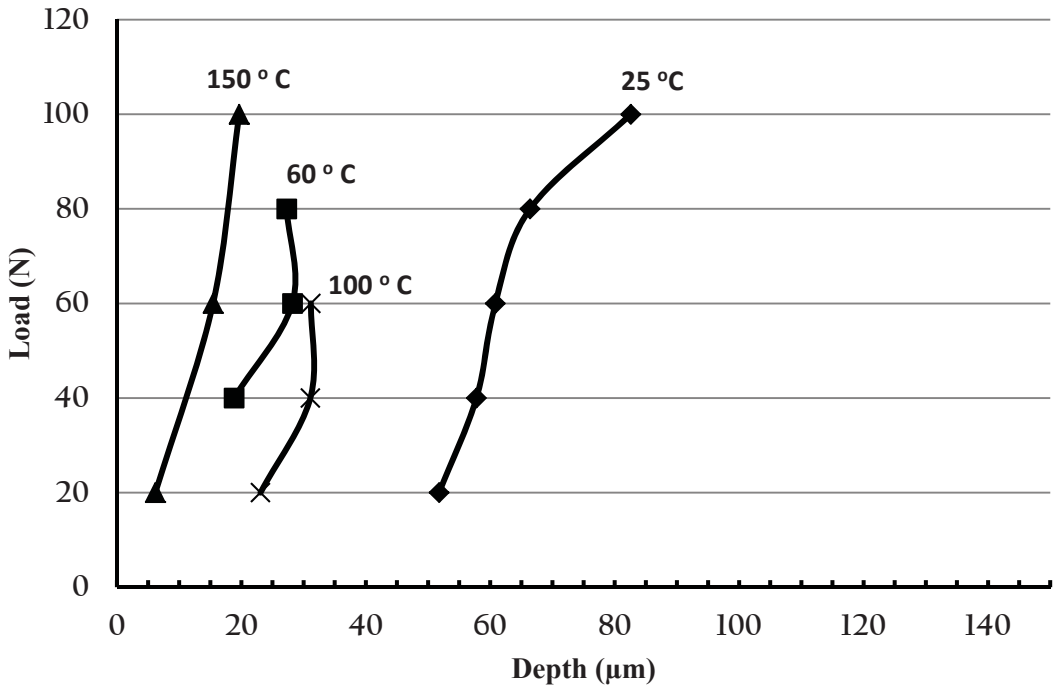


**Figure 4.21 - Max load vs. max depth of indentation tests at medium strain rate (load rate of 10 N.min$^{-1}$)**

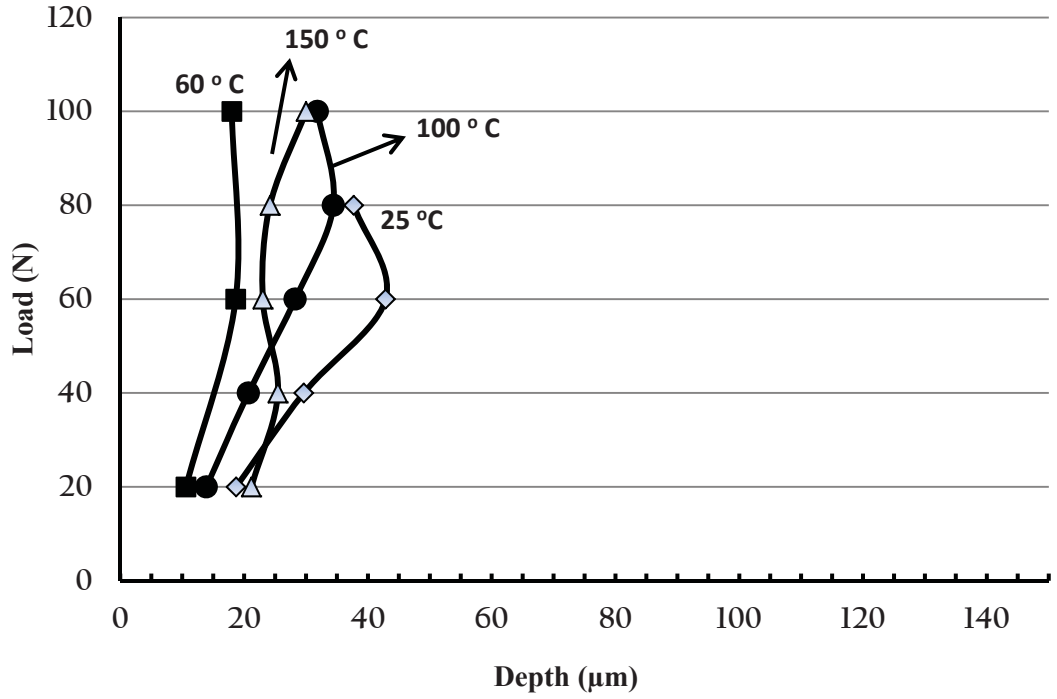


**Figure 4.22 - Max load vs. max depth of indentation tests at high strain rate (load rate of 20 N.min$^{-1}$)**

The effect of strain rate on the deformation behaviour of superelastic TiNi is shown in Figure 4.23. Upon increasing the load application rate from 1 to 20 $N.min^{-1}$, the maximum depth of indentation was significantly decreased. This suggests that at high strain rates, superelasticity diminishes. Similar behaviour has been observed by others [93,94 ] investigating tensile properties at high strain rates. They concluded that at high strain rates, heating of the sample as a result of the exothermic austenite to martensite transformation causes rapid heating, hence, causing austenite to stabilize. In the present work, no significant change in temperature was detected and further work is needed to investigate this phenomenon. This can have major implication in situations where high impact loads are common as in bearings in landing gears of aircrafts. At high impact loads superelasticity, hence, dent resistance drops causing permanent deformation of bearings.

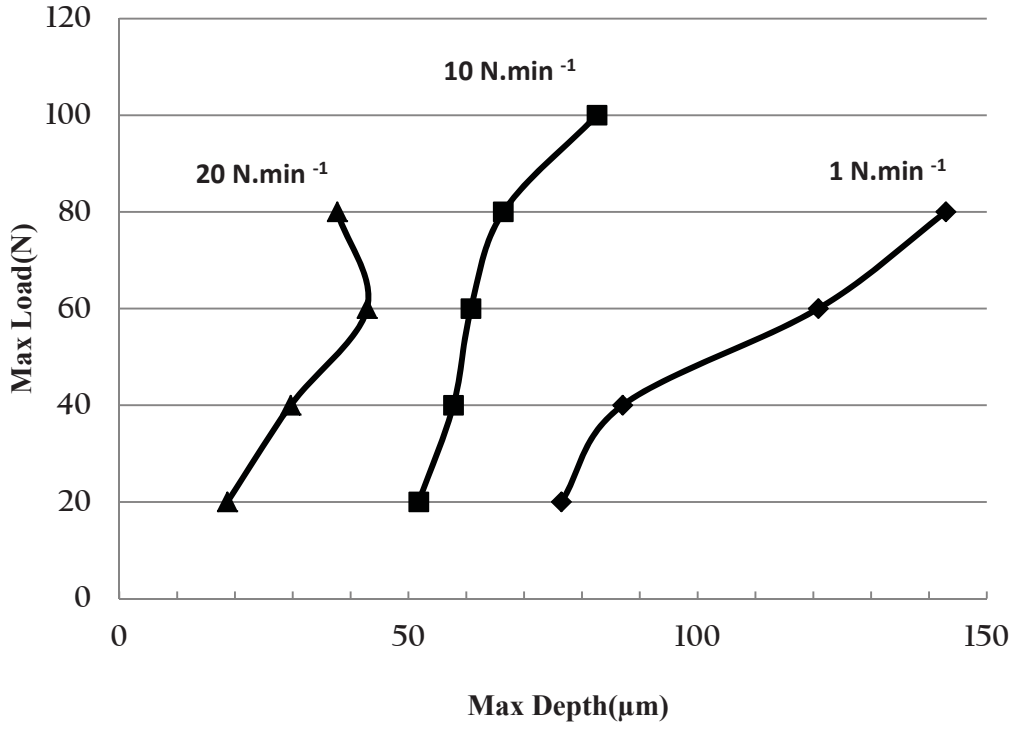


**Figure 4.23 - Max load vs. max depth diagram of superelastic TiNi at room temperature with different strain rates**

To confirm that the effect is due to superelastic behaviour of TiNi, identical experiments were performed on AISI 304 stainless steel which has similar mechanical properties to TiNi but not superelasticity. The results of indentation tests on steel show that the strain rate does not affect the deformation behaviour of steel, including the maximum indentation depth and residual strain as depicted in Figures 4.24 and 4.25.

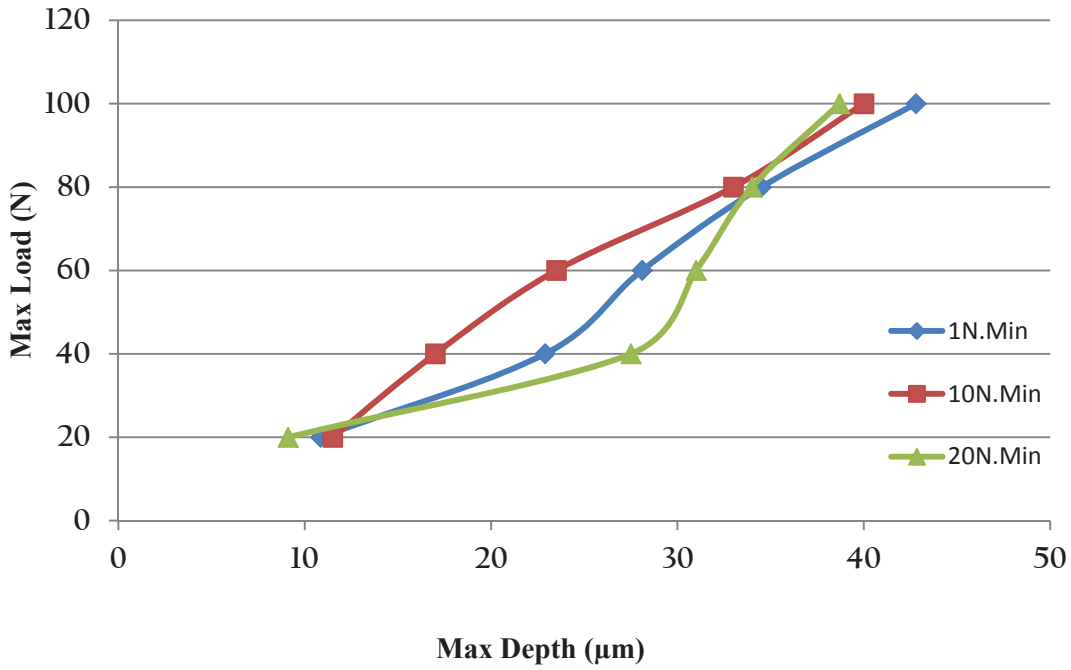


**Figure 4.24 - Indentation tests results of AISI 304 steel at room temperature and different strain rates**

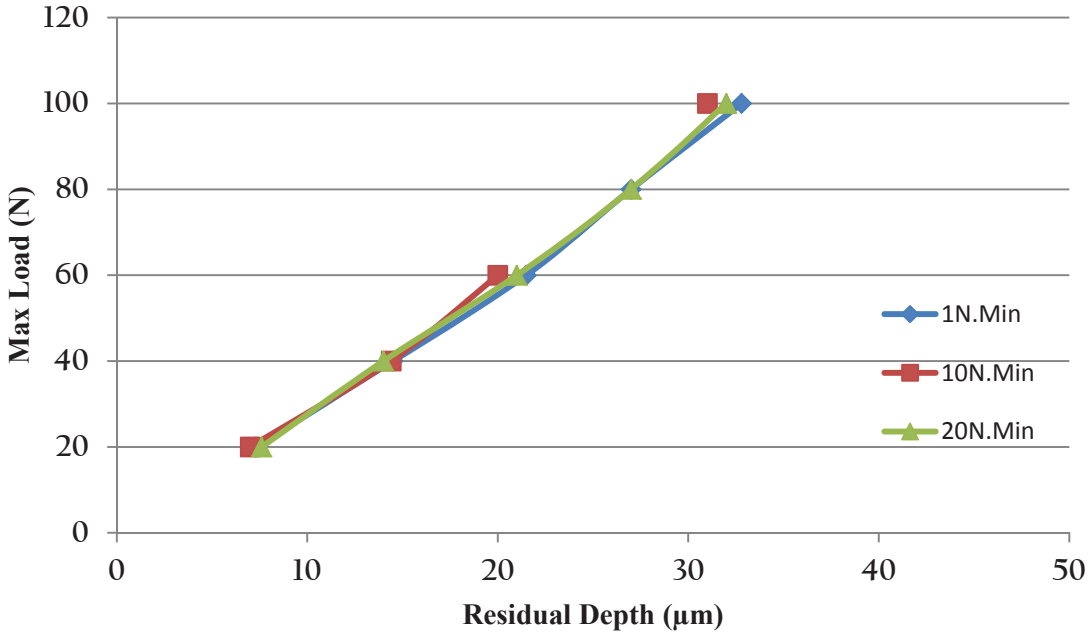


**Figure 4.25 - Residual strain after unloading cycle, different strain rates, room temperature AISI 304 steel**

#### 4.2.2.1 Stress – Strain Curves Obtained from Indentation Test

In order to compare the recoverable strain under localized indentation loads to simple tensile loads, load vs. depth curves are converted to stress-strain curves. The stress-strain curves for indentation tests were calculated using the following equations for stress and strain [95]:

$$\sigma_{ind} = \frac{P}{\pi a^2} \qquad Eq.4.1$$

$$\epsilon_{ind} = \frac{a}{R^*} \qquad Eq.4.2$$

Where $P$ is compressive load of indentation, $\pi a^2$ is the projected contact area between indenter and the specimen, $a$ is the contact radius. According to Hertz's theory, $R^*$ denotes the effective radius of the specimen and indenter system, and the contact radius is calculated from indenter depth (d), defined as follows:

$$\frac{1}{R^*} = \frac{1}{R_s} + \frac{1}{R_i} \qquad Eq.4.3$$

$$a = \sqrt{2Rd} \qquad Eq.4.4$$

in which $R_s$ and $R_i$ are the radius of the sample and indenter, respectively. In this experiment, all the indentation samples are flat, which makes $R_s = \infty$ and then $R^* = R_i$. The following figures show the stress-strain curves of indentation tests at different temperatures and strain rates.

Using the above equations and indentation data, stress-strain curves are plotted in Figure 4.26. The curves show initial high stress which is due to the initial small contact area between indenter and the work piece, as asperities from both surface meet. This followed by a plateau associated with austenite to martensite transformation and superelastic behaviour, similar to that observed in stress-strain curves generated in tensile tests. However, the amount of recoverable strain seems to be about double that achieved under tensile loading. This higher recoverable strain under indentation was observed by others [78]. The authors suggested that the hydrostatic pressure under indentation load results in lower transformation stress, due to larger deformation zone, hence, more recoverable strain is achieved. It is also observed that the transformation stress rises with higher load application rate.

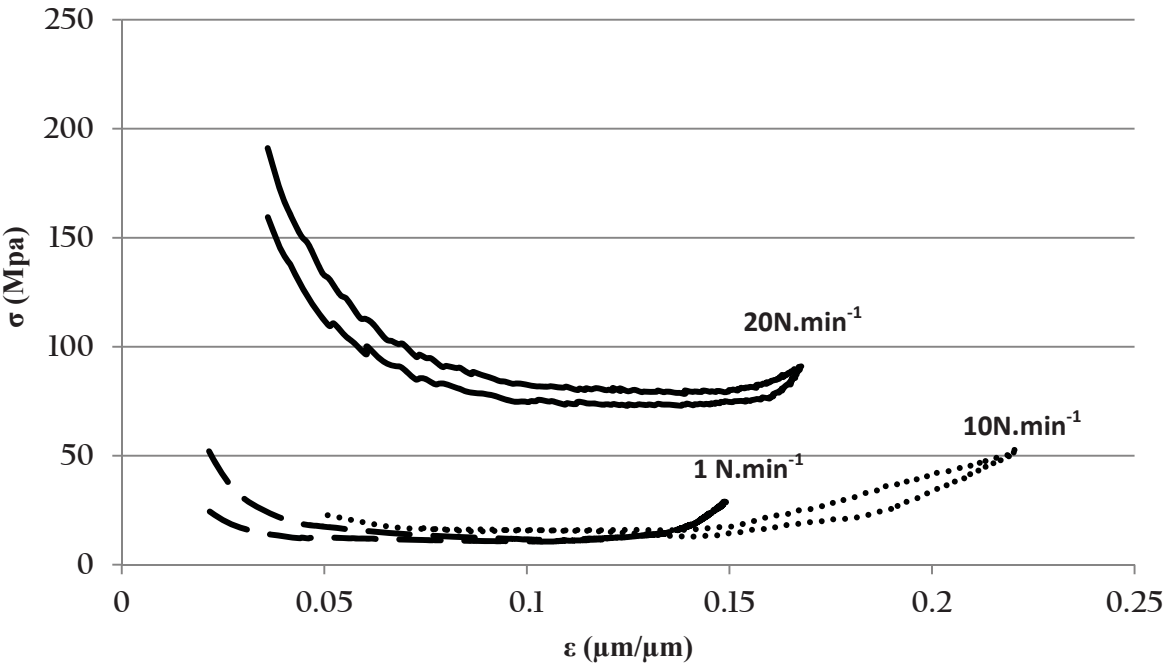


**Figure 4.26 - Stress-strain curve from indentation tests at 25 $^{o}$C for superelastic TiNi**

### 4.2.3 Sharp Indenter

The stress distribution is complex and the stress level is higher under a sharp indenter than under a spherical indenter. The stress under the tip of sharp indenter is very high due to the extremely small area of contact; this leads to slip-plasticity in the material. Dislocations that are produced due to slip-plasticity in shape memory alloy can deteriorate shape memory and superelastic effects. The presence of dislocations and plastic deformation hinder the reversible martensitic transformation in SMA.

The following graphs show the loading and unloading cycles of superelastic TiNi indentation test results under sharp indenter (4.27 (a)), spherical indenter (4.27 (b)) and AISI 304 stainless steel under sharp indenter (4.27 (c)). All graphs depict the indentation results at room temperature but at different strain rates. The effect of indenter tip geometry on the characteristics of superelastic TiNi is noticeable from Figures 4.24 (a) and (b). It can be clearly perceived that the sharp indenter can produce residual strain after unloading due to a higher stress concentration. In contrast, all the generated strain

by spherical indenter is fully recovered after unloading at slow and medium strain rates as a result of superelasticity.

The deformation behaviour of AISI 304 steel is different from superelastic TiNi. While the recovery is between 10 and 20% of the total indentation depth in steel, it is around 80 to 90% for superelastic TiNi under sharp indenter. Therefore, recoverable deformation energy and the ratio of recoverable energy to the total deformation energy (η, the areas enclosed under the unloading curve to that under the loading curve) for superelastic TiNi alloy are high in comparison with conventional steel. Also, η is near unity for superelastic TiNi under the spherical indenter, which indicates superelastic TiNi has high capability for absorbing energy and decreased potential for damage during impact. This phenomenon can enhance the tribological behaviour of superelastic TiNi alloys, such as, wear and dent resistance.

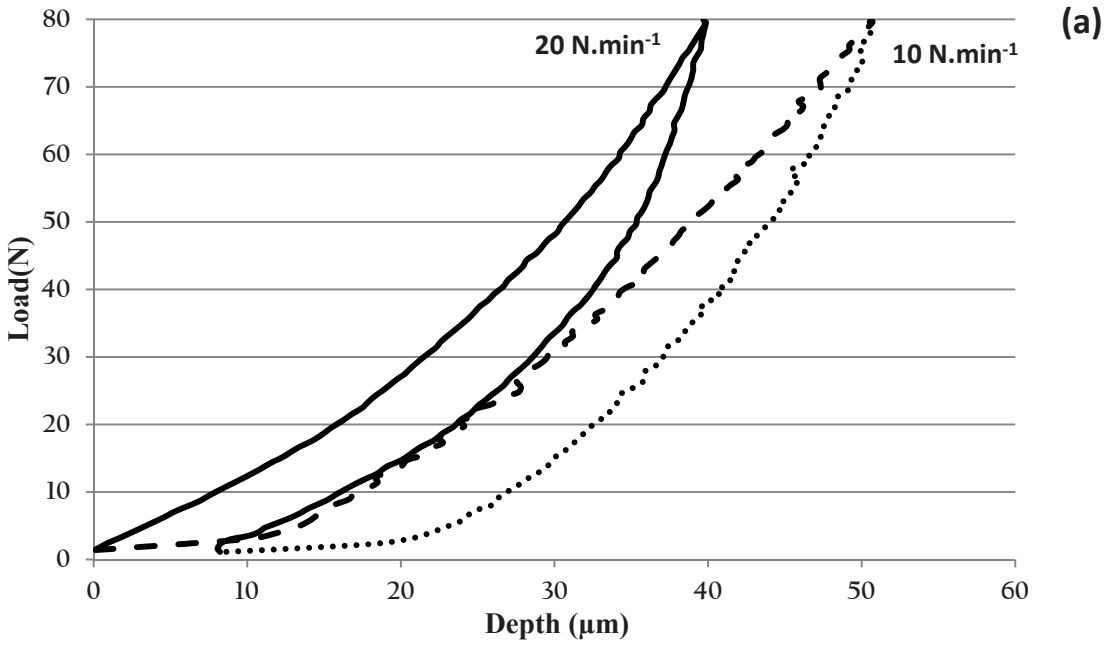


**Figure 4.27 - (a) - Loading and unloading cycle of superelastic TiNi after indentation test under sharp indenter**

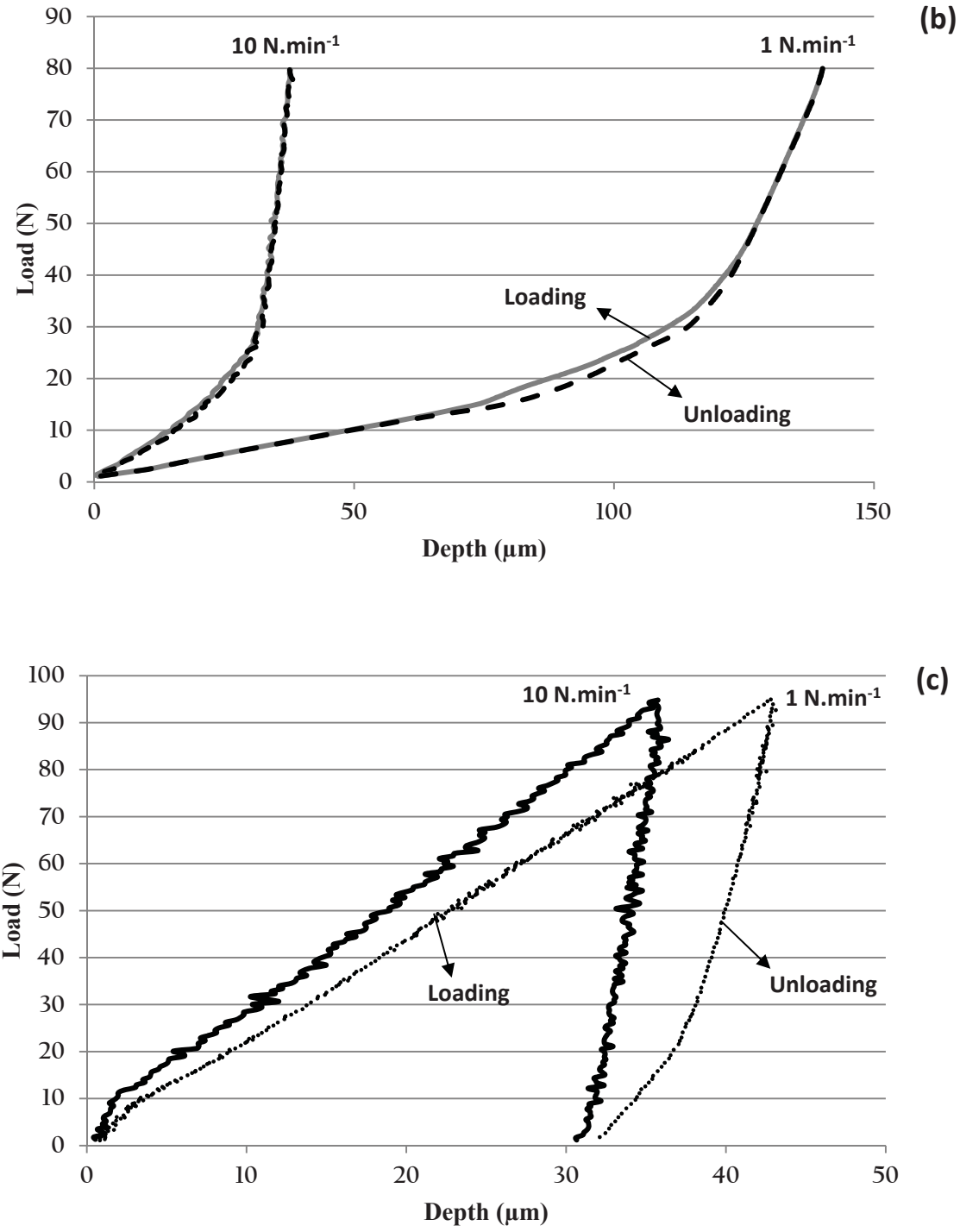


**Figure 4.27 - Continued, loading and unloading cycle of (b) superelastic TiNi, spherical indenter, and (c) AISI 304 steel, sharp indenter**

Hence, superelastic TiNi is an excellent candidate for applications where components are subjected to high compressive stresses, such as bearings. In contrast, the magnitude of η is so small for AISI 304 steel; it suffers high denting damage (plastic deformation) under localized compressive loads.

Loading and unloading data was generated for sharp indenter during testing at various temperatures, strain rates and maximum loads. The following curves compare the load vs. depth curves at constant strain rates and maximum loads and different testing temperatures.

Figures 4.28 – 4.31 represent a typical load vs. depth profiles, similar to those obtained for a spherical indenter. However, the unloading portion of the curves show residual strain (plastic strain) unrecovered after completely removing the load. The residual strain seems to exist even for the lowest maximum load of 40 N. This is attributed to high stress just below the tip of the indenter, which exceeds the yield strength of the material.

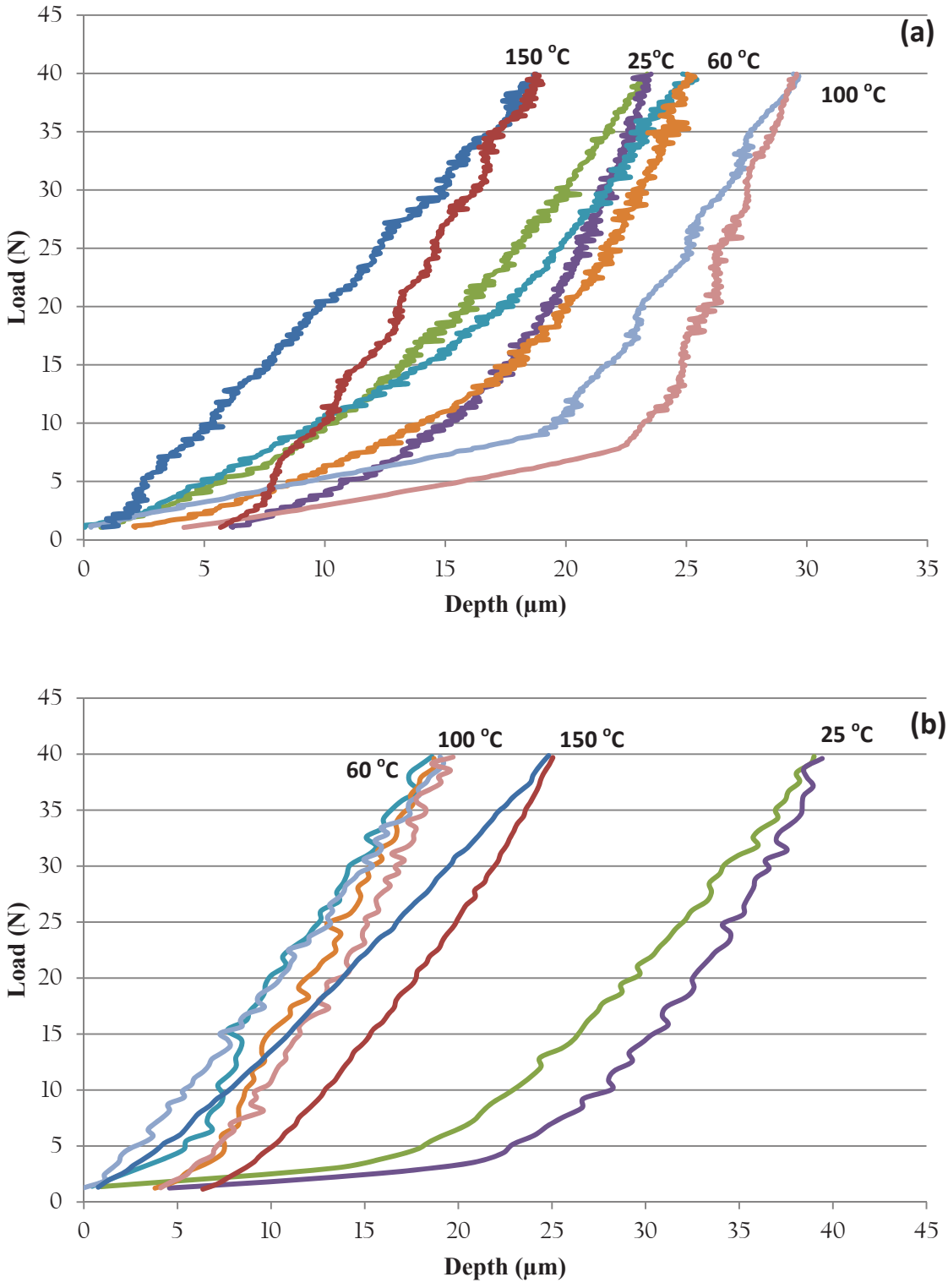


**Figure 4.28 - Loading - unloading curves of superelastic TiNi under maximum load of 40 N, various temperatures and load application of (a) 1N.min$^{-1}$, (b) 10 N.min$^{-1}$**

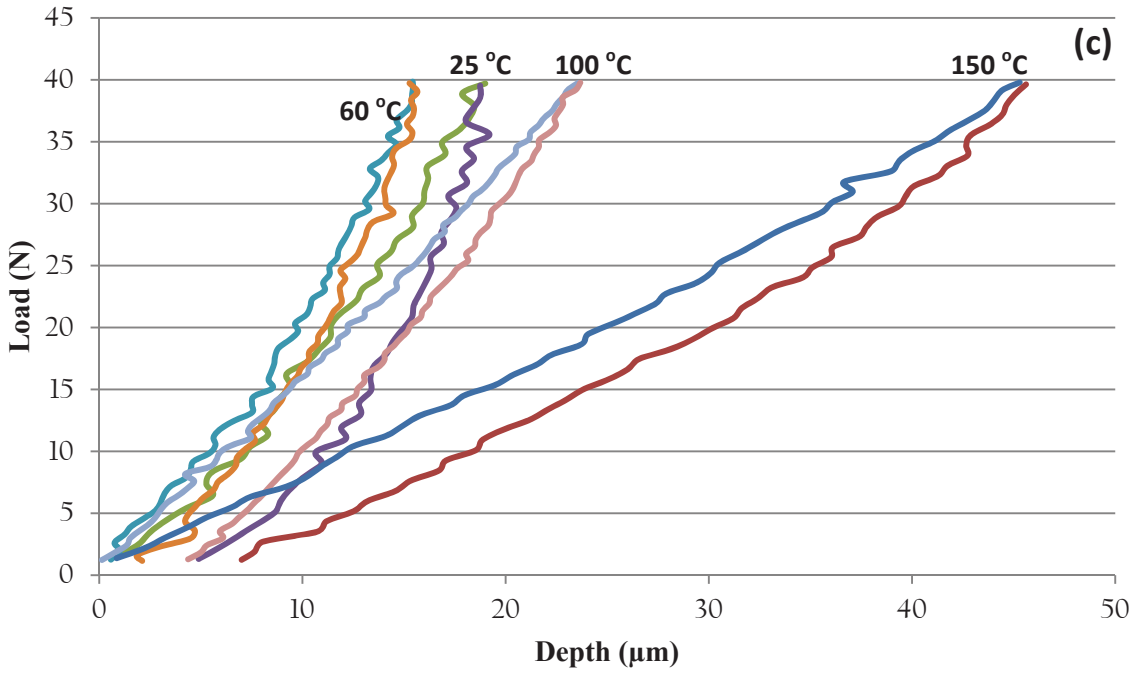


**Figure 4.28 - Continued, loading - unloading curves of superelastic TiNi under maximum load of 40 N, various temperatures and load application of (c) 20N.min$^{-1}$**

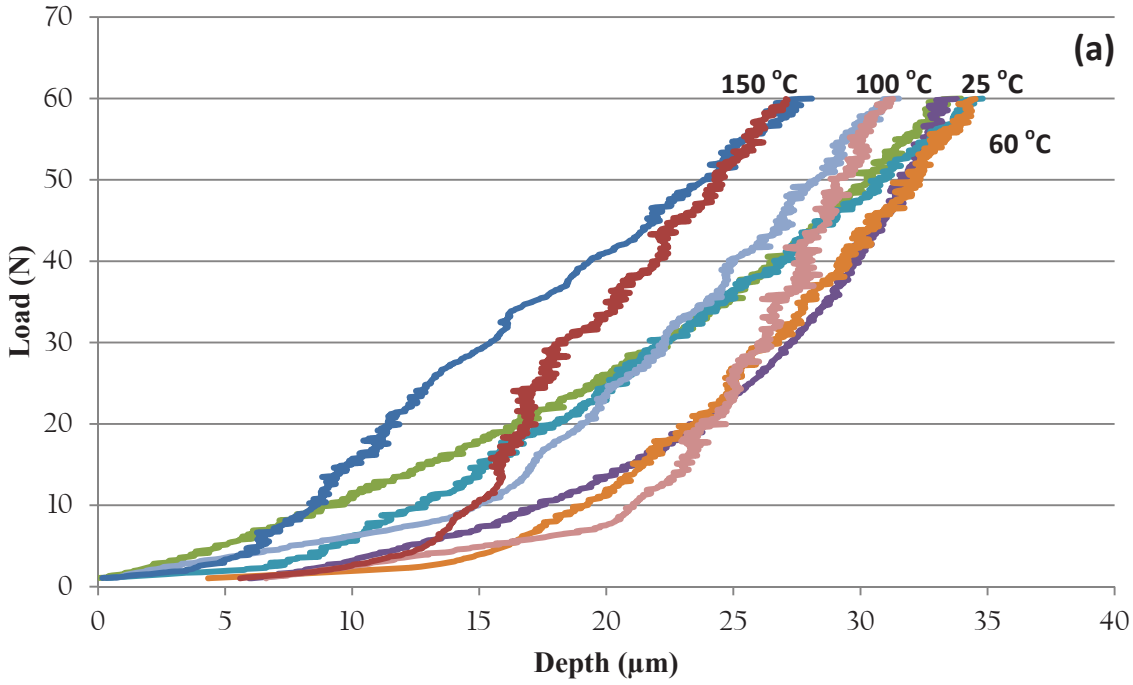


**Figure 4.29 - Loading - unloading curves of superelastic TiNi under maximum load of 60 N, various temperatures and load application of (a) 1N.min$^{-1}$**

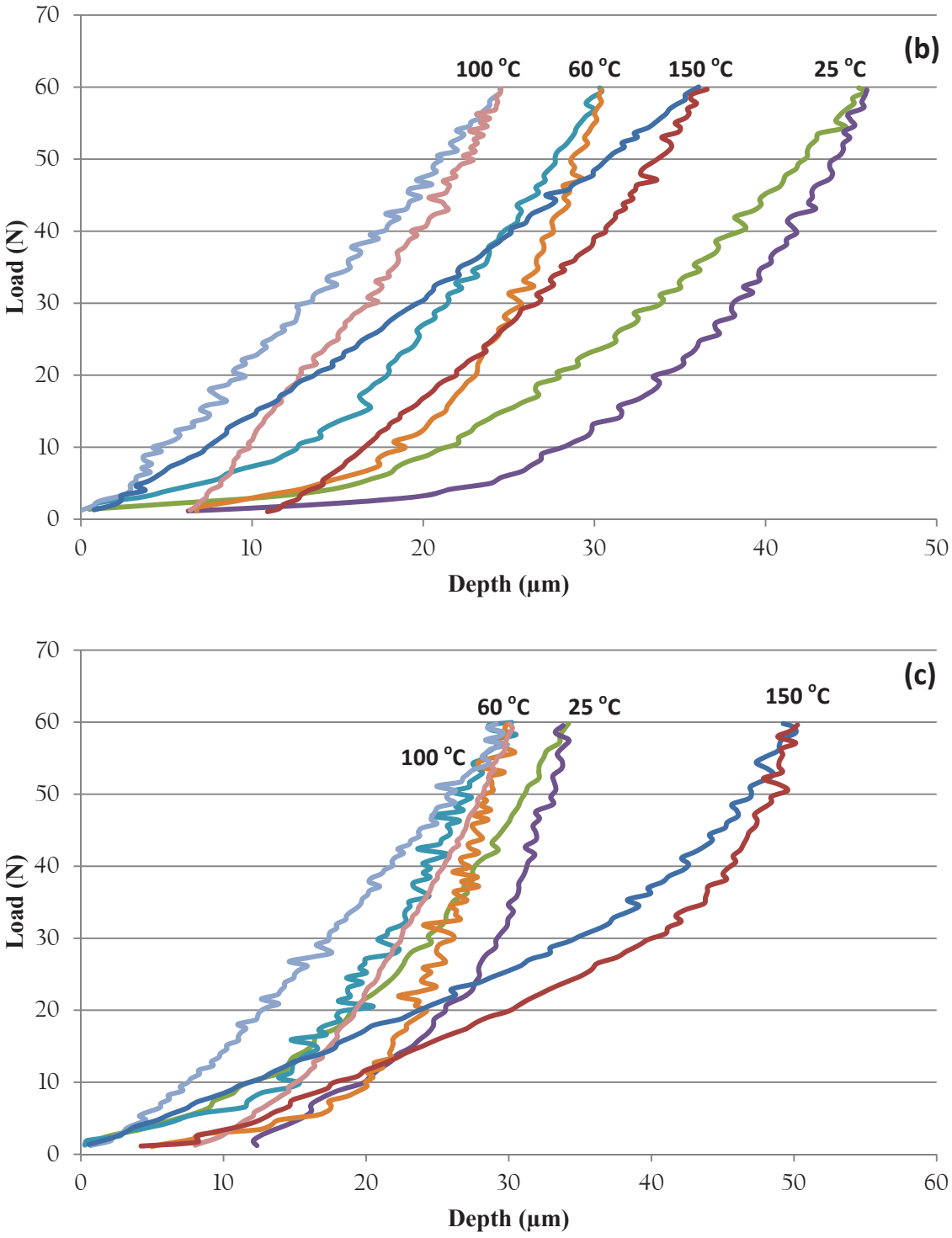


**Figure 4.29 - Continued, loading - unloading curves of superelastic TiNi under maximum load of 60 N, various temperatures and load application of (b) 10N.min$^{-1}$ and (c) 20 N.min$^{-1}$**

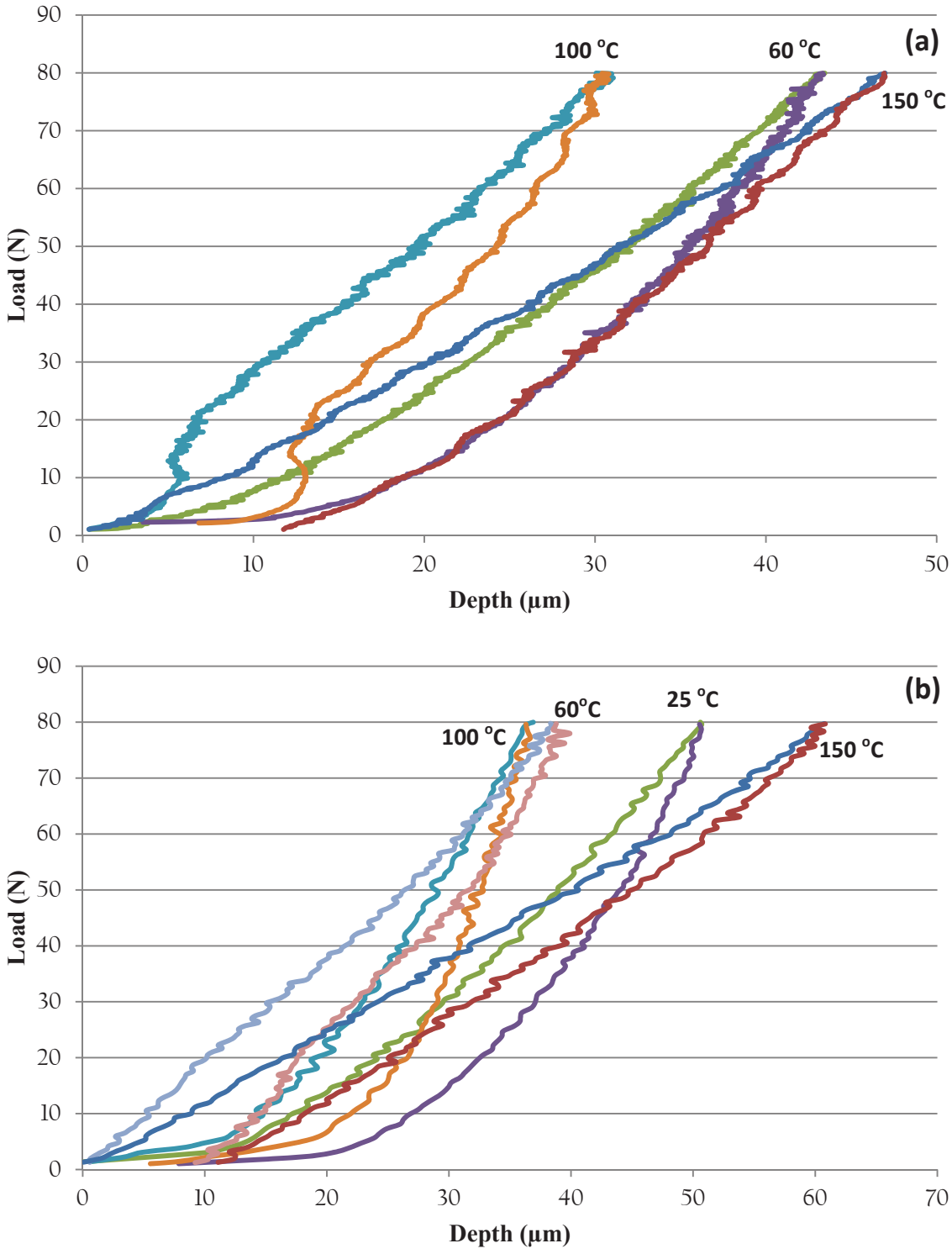


**Figure 4.30 - Loading - unloading curves of superelastic TiNi under maximum load of 80 N, various temperatures and load application of (a) 1N.min$^{-1}$ and (b)10 N.min$^{-1}$**

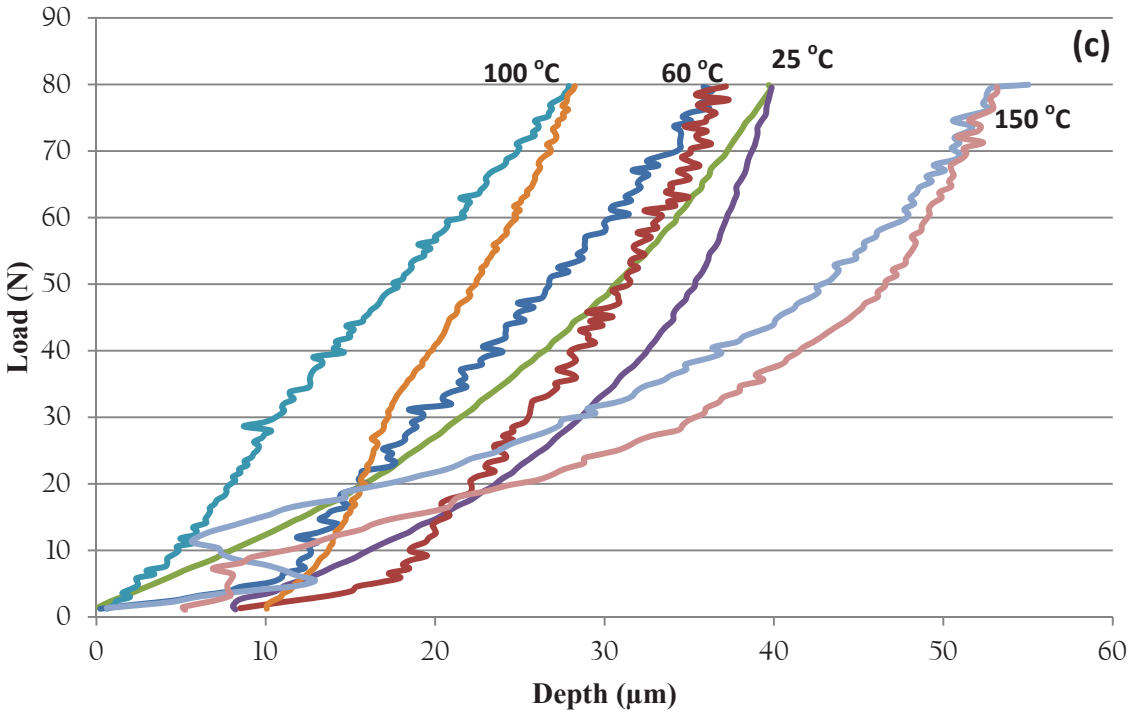


**Figure 4.30 - Continued, loading - unloading curves of superelastic TiNi under maximum load of 80 N, various temperatures and load application of (c) 20 N.min$^{-1}$**

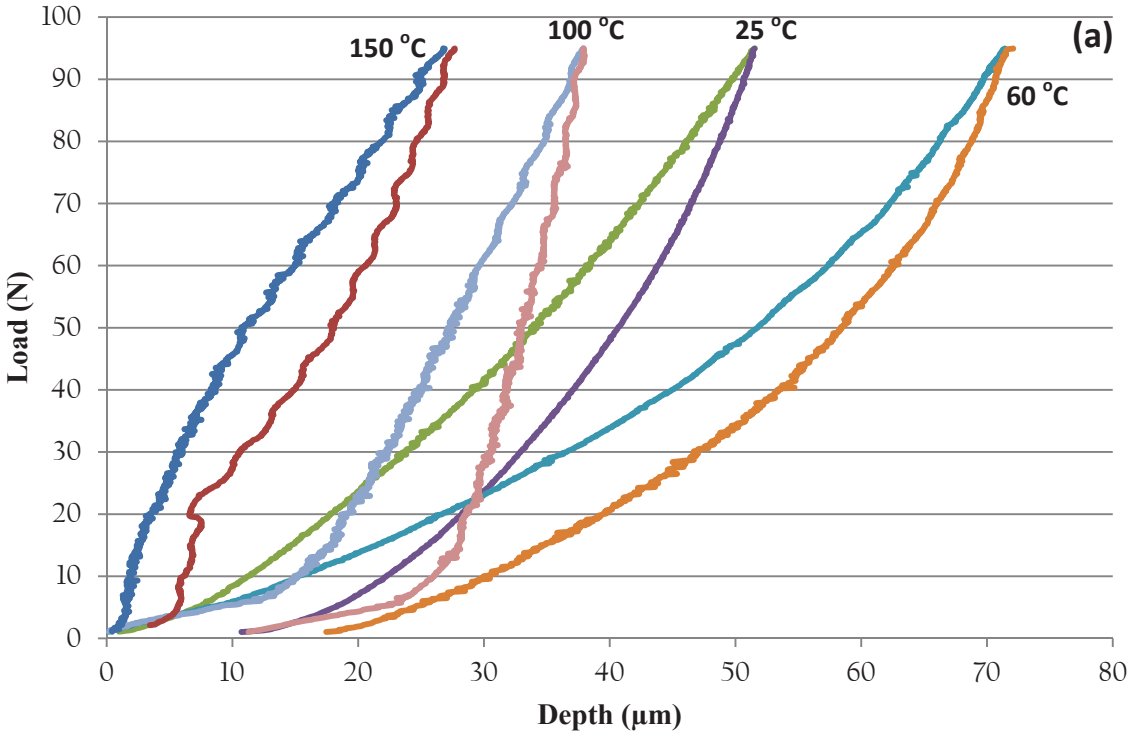


**Figure 4.31 - Loading - unloading curves of superelastic TiNi under maximum load of 100 N, various temperatures and load application of (a) 1 N.min$^{-1}$**

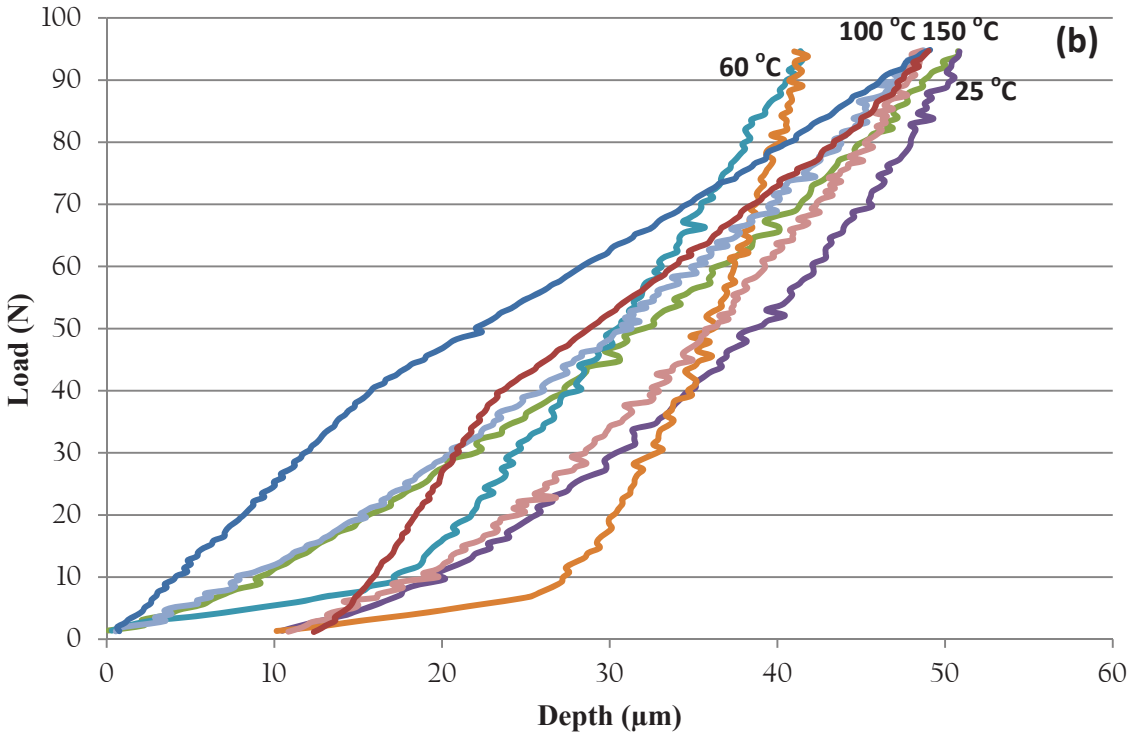


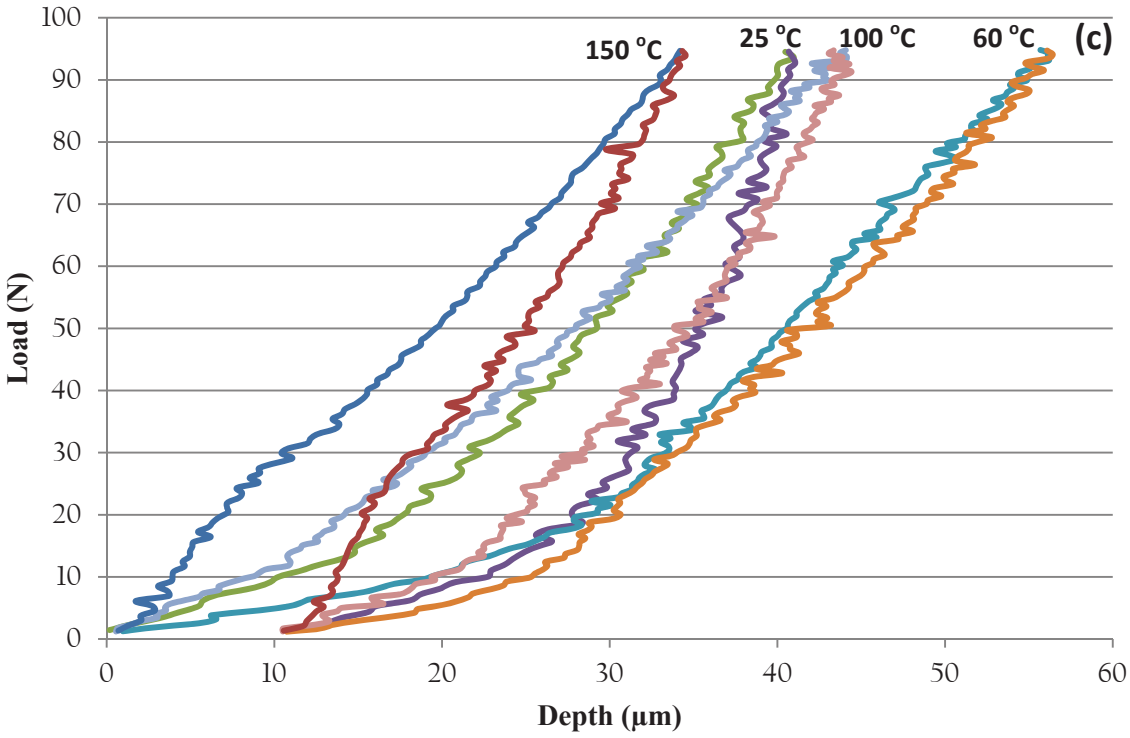


**Figure 4.31 - Continued, loading - unloading curves of superelastic TiNi under maximum load of 100 N, various temperatures and load application of (b) 10N.min$^{-1}$ and (c) 20 N.min$^{-1}$**

Figure 4.26 shows the maximum load vs. maximum indentation depth of superelastic TiNi under a sharp indenter at various temperatures and strain rates generated from load vs. depth plots in Figures 4.28 – 4.31. It can be clearly seen that temperature and strain rate effects on the deformation behaviour of superelastic TiNi is not easily resolvable under sharp indenter in comparison with a spherical indenter. It is difficult to establish a clear understanding of the deformation mechanisms of superelastic TiNi under sharp indenter. The reason for this is that there are several processes and effects occurring simultaneously, namely, elastic-plastic deformation, work hardening, reversible austenite to martensite transformation and martensite stabilization [10]. Also, with increasing the indentation load, the plastic zone in material enlarges, hence, reduced superelastic effect. All the above mechanisms operate in a complex manner to yield the measured superelastic strain. On the other hand, it can be seen that, the maximum depth slightly decreases as the temperature increases, especially at lower loads. Also, increasing the strain rate leads to a minor decrease in the maximum depth, a finding which is similar to the results for spherical indenters.

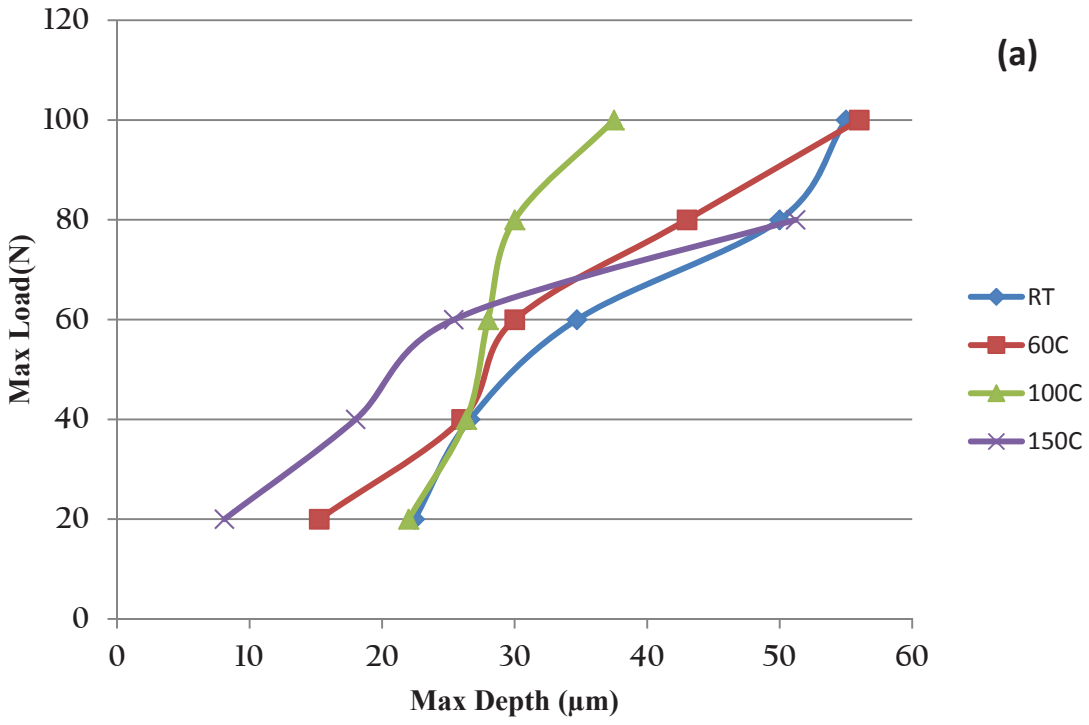


**Figure 4.32 - Max load vs. max depth, sharp indenter, (a) low strain rate (1N.min$^{-1}$)**

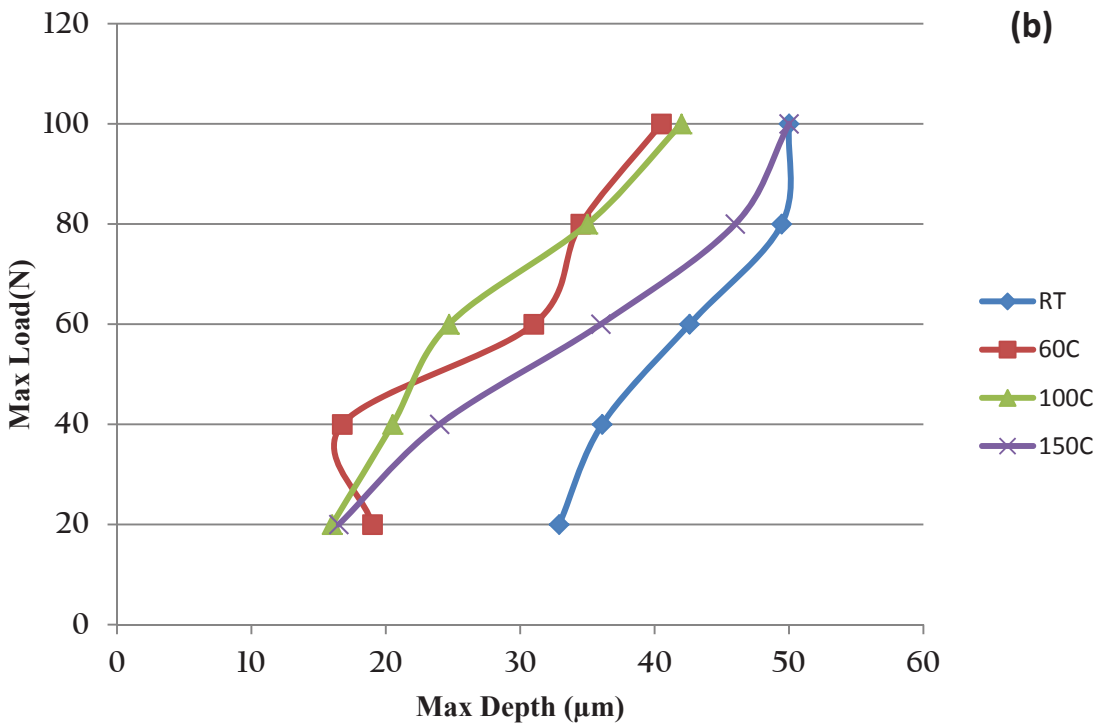


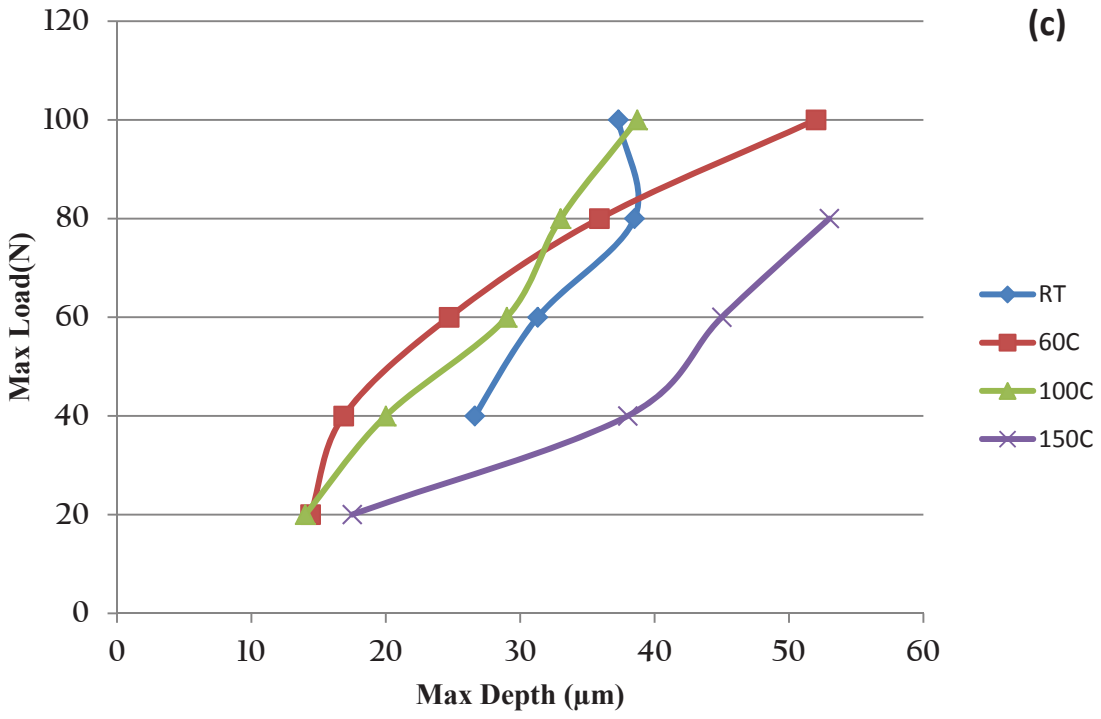


**Figure 4.32 - Continued, max load vs. max depth, sharp indenter, (b) medium strain rate ($10N.min^{-1}$) and (c) high strain rate ($20N.min^{-1}$)**

# CHAPTER 5 CONCLUSIONS

In the present project, deformation characteristics of both superelastic and shape memory TiNi under tensile and localized compressive loads were studied. The effects of load, strain rate, temperature and indenter geometry on the reversible martensitic phase transformation and deformation mechanisms were investigated. The following main conclusions have emerged.

i. It has been found that testing temperature has a significant effect on austenite to martensite transformation stress for superelastic TiNi. Stress – strain curve of superelastic TiNi was investigated through series of tensile tests at three different temperatures. It is noticed that the required stress for starting the transformation from austenite to stress induced martensite is increased significantly upon increasing temperature. The transformation stress at 85℃ is twice that at 25 $^{o}$C. This phenomenon can postpone the martensitic transformation to higher stress level in real life applications; hence, less deformation is expected at higher temperature within the same loading range.

ii. Cyclic loading and unloading tensile tests have been performed on superelastic and shape memory TiNi alloys. Both forward and reverse transformation stresses decreased with the number of cycles; a reduction of about 4% from the first cycle to third cycle in superelastic TiNi is observed, which can have implication in dynamic mechanical systems as the expected transition stress changes with cycles of operation. The formation of small amount of localized slip during cyclic loading facilitates the martensitic transformation which leads to lower stress plateau in the stress- strain curve.

iii. Above 85 °C ($M_d$), the superelastic TiNi behaves like conventional materials. Austenite deforms by slip instead of transition to martensite. Consequently, it can be subjected to plastic deformation, hence, early fracture while the superelastic TiNi component is in the service.

iv. There is a significant increase in stress as a result of heating loaded superelastic TiNi, which may lead to total fracture. This observation can pose great implications in practical situations i.e. overheating in service to above the martensite to austenite transformation temperature leads to sudden increase in stress level and could potentially lead to total failure of the superelastic TiNi component.

v. It has been found from indentation tests, using a spherical indenter, that increasing the temperature and strain rate diminishes the martensitic transformation in superelastic TiNi. Hence, the deformation (maximum indentation depth) of the sample is considerably higher at low temperature and slow strain rate.

vi. Superelasticity is less sensitive to temperature and strain rate changes under a sharp indenter due to high stress concentration and plastic deformation beneath the indenter tip. Also, due to slip-plasticity under sharp indenter the generated strain does not fully recover; on the other hand, in the case of spherical indenter, the generated strain completely recovers after unloading.

vii. The magnitude of recovery is between 10 to 20% for AISI 304 steel under sharp indenter, while it is approximately 80 to 90 % for superelastic TiNi. Thus, low damage under localized compressive loads for superelastic TiNi as compared to AISI304 stainless steel make it a good candidate for applications where dent resistance is important, such as in bearings.

In the present study, deformation of TiNi alloys under tensile and localized compressive loads as a function of temperature and strain rate have been investigated. However, a fair amount of work is still needed to fully establish the fundamental principles governing the deformation behaviour of TiNi alloys, especially under localized compressive loads. A number of recommendations for future work are listed below:

i. Carry out in-situ microscopy and XRD test for superelastic TiNi alloy to observe the conditions of phase transformation under compressive loads.

ii. Perform ball-on-disc and scratch testing at different strain rates in order to observe the direct effects of strain rates on wear resistance of superelastic TiNi alloys.

# REFERENCES

[1] D. C. Lagoudas, Shape Memory Alloys: Modeling and Engineering Application, Springer Science, (2008).

[2] C.M. Wayman, Some applications of shape-memory alloys. J Met. Vol. 6 (1980), pp.129–137.

[3] S. Miyazaki, Y. Omhi, K.Otsuka, Y. Suzuki, Characteristics of deformation and transformation pseudoelasticity in Ti–Ni alloys. J Phys. Vol. 43 (1982), pp. 255–266.

[4] E.J. Perkins. Shape Memory Effects in Alloys. Plenum Press, New York,(1975).

[5] T.W. Duering, K.N. Melton, C.M. Wayman, Engineering aspects of shape memory alloys. Butterworth-Heinemann Ltd. (1990).

[6] I. Schmidt, L.C. Brinson, R. Lammering, Micro and macromechanical observation of polycrystalline NiTi using in situ optical microscopy. J Phys IV France Vol. 112 (2003), pp. 655–658.

[7] E. Hornbogen, V. Mertinger, D. Wurzel, Microstructure and tensile properties of two binary NiTi-alloys, Scr Mater Vol. 44 (2001), pp.171–178.

[8] M.C. Carroll, C. Somsen, G. Eggeler, Multiple-step martensitic transformations in Ni-rich NiTi shape memory alloys. Scr Mater Vol. 50 (2004), pp.187–192.

[9] D.Y. Li. Development of novel tribo composites with TiNi shape memory alloy matrix. Wear, Vol. 255 (2003), pp. 617–628.

[10] C. Zhang, Z.N. Farhat, Sliding wear of superelastic TiNi alloy. Wear, Vol. 267(2009), pp. 394–400.

[11] L. Tan, R.A. Dodd, W.C. Crone, Corrosion and wear-corrosion behaviour of NiTi modified by plasma source ion implantation. Biomaterials, Vol. 24 (2003), pp. 3931–3939.

[12] K. Otsuka, X. Ren, Recent developments in the research of shape memory alloys. Intermetallics Vol. 7 (1999), pp. 511–28.

[13] S.K. Wu, H.C. Lin, Recent development of TiNi-based shape memory alloys in Taiwan. Mater Chem PhysVol. 64 (2000), pp.81–92.

[14] J.V. Humbeeck, Non-medical applications of shape-memory alloys. Mater Sci Eng A Vol. 273 – 275 (1999), pp.134–148.

[15] T. Duerig, A. Pelton, D. Stockel. An overview of nitinol medical applications. Mater Sci Eng A Vol. 273-275 (1999), pp.149–160.

[16] S. Kang, K. Yoon, J. Kim, T. Nam, G. Tae-Hyun, V. Gjunter. In vivo result of porous TiNi shape memory alloy: bone response and growth. Mater Trans. Vol 43 (2002), pp. 1045–1048.

[17] H.C. Lin, H.M. Liao, J.L. He, K.C. Chen, and K.M. Lin, Wear characteristics of TiNi shape memory alloys. Metall Mater Trans A, Vol. 28A (1997), pp. 1871-1877.

[18] D.Y. Li, A new type of wear-resistant material: pseudo-elastic TiNi alloy. Wear, Vol. 221 (1998), pp. 116-123.

[19] L.M. Wian, Q.P. Sun and X.D. Xiao, Role of phase transition in the unusual microwear behaviour of superelastic TiNi shape memory alloy. Wear, Vol. 260 (2006), pp. 509-522.

[20] R. Vogel and H.J. Wallbaum, The system FeNi-NiTi-FeTi. Archivfuer das EisenbuettenWesen, Vol.12 (1938), pp. 296-304.

[21]P. Duwezand J.L. Talor, The structure of intermediate phase in alloys of titanium with iron, cobalt and nickel. Trans AIME, Vol. 188 (1950), pp.1173-1176.

[22] D.M. Poole, Hume-Rothery, The equilibrium diagram of the system nickel- titanium J Inst Met Vol. 83 (1954), pp. 473-480.

[23] G. R. Purdy and J. G. Parr, The Study of the Titanium-Nickel System between Ti2Ni and TiNi, Trans. AIME, Vol. 221 (1961), pp. 636-639.

[24] K. Otsuka and X. Ren, Physical metallurgy of Ti-Ni-based shape memory alloys. Prog Mater Sci., Vol. 50 (2005), pp. 511-678.

[25] M. Marcinkowski, A. Sastri, D. Koskimaki, Martensitic behaviour in equi-atomic Ni-Ti alloy.PhilosMag ,Vol. 18 (1968), pp. 945-958.

[26] M. Nishida, C. Wayman, R. Kainuma, T. Honma, Further electron microscopy studies of the $Ti_{11}$ $Ni_{14}$ phase in an aged Ti -52at%Ni shape memory alloy, Scripta MetallVol. 20 (1986), pp. 899- 906.

[27] T. Saburi, K. Otsuka, C. Wayman, Shape Memory Materials, Cambridge University Press, 49 (1998).

[28] T. Saburi, S. Nenno, T. Fukuda, Further electron microscopy studies of the $Ti_{11}$ $Ni_{14}$ phase in an aged Ti – 52 at %Ni shape memory alloy, J Less-Comm Metals, Vol. 125 (1986), pp. 157- 163.

[29] W. Tang, Thermodynamic study of the low-temperature phase B19' and the martensitic transformation in near-equiatomic Ti-Ni Shape Memory Alloys, Metall Trans Vol. 28 (1997), pp. 537- 544.

[31] J.A. Krumhansl and R.J. Gooding, Structural phase transition with little phonon softening and first-order character, Phys. Rev,Vol.39 (1989), pp. 3047-3053.

[32] J.A. Krumhansl, Landau models for structural phase transitions: Are soft modes needed?, Sol.Stat.Comm.,Vol.84 (1992), pp. 251-254.

[33] G. Olson, M. Cohen, Thermo elastic behaviour in martensitic transformations, Scripta Metall ,Vol. 9 (1975), pp. 1247-1257.

[34] Y.Liu,G. Tan, Effect of deformation by stress-induced martensitic transformation on the transformation behaviour of NiTi, Intermetallics, Vol. 8 (2000), pp. 67- 75.

[35] Y. Xu, K. Otsuka,N. Toyama, H. Yoshida, H. Nagai, T. Kishi, Additive nature of recovery strains in heavily cold-worked shape memory alloys, Scripta Mater, Vol. 48 (2003), pp. 803-808.

[36] Y. Murakami, Y. Nakajima and K. Otsuka, Effect of quenched-in vacancies on the martensitic transformation, Scripta Metall, Vol.34 (l996), pp. 955-962.

[37] K. Bhattacharya, Self-accommodation in martensite, Arch. Rational Mech. Anal, Vol. 120 (1992), pp.201-244.

[38] R. Lahoz, J.A. Puértolas, Training and two-way shape memory in NiTi alloys: influence on thermal parameters, J. Alloy. Compd.,Vol. 381 (2004), pp. 130–136.

[39] C. Lexcellent, S. Leclercq, B. Gabry, G. Bourbon, The two way shape memory effect of shape memory alloys: an experimental study and a phenomenological model, Int. J. Plasticity Vol. 16 (2000), pp. 1155-1168.

[40] A.Vitiello, G. Giorleo and R.E. Morace, Analysis of thermomechanical behaviour of Nitinol wires with high strain rates, Smart Matter. Struct Vol. 14 (2005), pp. 215 – 221.

[41] T. Lim and D. McDowell, Mechanical behaviour of an Ni-Ti alloy under axial-torsional proportional and non-proportional loading, J Eng Mater Technol Vol. 121 (1999), pp. 9-18.

[42]Y. Liu, Y. Li, K.T. Ramesh and J.V. Humbeeck, High strain rate deformation of martensitic NiTi shape memory alloy, Scripta Mater. Vol. 41 (1999), pp. 89-95.

[43] R. Adharapurapu, F. Jiang, S. Kenneth, T. George, Response of NiTi shape memory alloy at high strain rate: A systematic investigation of temperature effects on tension–compression asymmetry, Acta MaterialiaVol. 54 (2006), pp. 4609-4620.

[44] R. Plietsch and K. Ehrlich, Strength differential effect in pseudoelastic NiTi shape memory alloys, Acta MaterialiaVolume 45, Issue 6, June 1997, Pages 2417-2424

[45] L. Orega and D. Favier, stress-induced martensitic transformation of NiTi alloy in isothermal shear, tension and compression, Acta mater. Vol. 46 (1998), pp. 5579-5591.

[46] ASTM International, Standard Test Method for Tension Testing of Nickel-Titanium Superelastic Materials (2006).

[47] S.P. Belyaev, N.N. Resnina , A.E. Volkov, Influence of irreversible plastic deformation on the martensitic transformation and shape memory effect in TiNi alloy, Mater.Sci. Eng. A, Vol. 438–440 (2006), pp. 627–629.

[48] P.G. Lindquist and C.M. Wayman, Engineering aspects of Shape Memory Alloys, Butterworth-Heinemann, London, 58(1990).

[49] T. Saburi, T. Takagi, S. Nenno, K. Koshino, in: M. Doyama, S. Somlya, R. P. H. Chang (Eds.), Shape Memory Materials, MRS International Meeting on Advanced Materials, Vol. 9(1989) , pp. 147–152.

[50] D.Y. Li, A new type of wear-resistant material: pseudo-elastic TiNi alloy, Wear Vol. 221 (1998), pp. 116–123.

[51] H. Funakubo , Shape Memory Alloys, Gordon and Breach Science Publishers (1987).

[52] P. G. Lidquist, C. M. Wayman, Shape memory and transformation behaviour of martensitic Ti-Pd-Ni and Ti-Pt-Ni alloys, in: T. W. Duerig, K. N. Melton, D. St¨ockel, C. M. Wayman (Eds.), Engineering Aspects of Shape Memory Alloys, Butterworth-Heinemann, London, 1990, pp.58–68.

[53] P. E. Thoma, J. J. Boehm, Effect of composition on the amount of second phase and transformation temperatures of NixTi90-xHf10 shape memory alloys, Mater.Sci. Eng. A Vol. 273-275 (1999), pp. 385–389.

[54] C.M. Wayman, I. Cornelis and K. Shimizu, Shape recovery temperature range in Cu--Al-Ni and Cu-Zn marmem alloys, ScriptaMetall, Vol.6 (l972), pp. 377-381.

[55] S. Miyazaki, Y. Igo and K. Otsuka, Effect of thermal cycling on the transformation temperatures of Ti---Ni alloys, Acta Metall. Vol.34 (l986), pp. 2045-2051.

[56] T. Saburi and S, Nenno, Proc. Int. Conf. on Martensitic Transformations, JIM, Sendai, (l986) 671.

[57] S. Miyazaki, T. Imai, Y. Igo and K. Otsuka, Effect of cyclic deformation on the pseudoelasticity characteristics of TiNi alloys. Metall. Trans., Vol.17A (l986), pp. 115-120.

[58] R. Rapacioli and M. Ahlers, The influence of short-range disorder on te martensitic transformation in Cu---Zn and Cu---Zn---Al alloys Acta Metall., Vol.27 (l979), pp.777-784.

[59] D.A. Miller, D.C. Lagoudas, Influence of cold work and heat treatment on the shape memory effect and plastic strain development of NiTi, Mater.Sci. Eng.A Vol. 308 (2001), pp. 161–175.

[60] E.M. Mitwally, M. Farag, Effect of cold work and annealing on the structure and characteristics of NiTi alloy, Mater. Sci. Eng. A, Vol.519, (2009), pp 155-166.

[61] P. Sittnera,b, Y. Liub, V. Novaka, On the origin of Lu¨ ders-like deformation of NiTi shape memory alloys, J. Mech. Phys. Solids, Vol. 53 (2005), pp. 1719–1746.

[62] H. Hosodaa, S. Miyazaki, K. Inoue, T. Fukui, K. Mizuuchi and et al., Cold rolling of B2 intermetallics, J. Alloy.Comp.Vol. 302 (2000), pp. 266–273.

[63] H.C. Lin and S.K. Wu, Determination of heat of transformation in a cold-rolled martensitic TiNi alloy, Metall. Trans. A Vol. 24 (1993), pp. 293–299.

[64] H.C. Lin and S.K. Wu, The tensile behaviour of a cold-rolled and reverse-transformed equiatomic TiNi alloy, Acta Metall. Mater. Vol. 42 (1994), pp. 1623–1630.

[65] L. Orgeasand D. Favier, Stress-induced martensitic transformation of a NiTi alloy in isothermal shear, tension and compression, Acta Mater,Vol. 46 (1998), pp.5579-5591.

[66]H. Sehitoglu I. Karaman, R. Anderson, X. Zhang, K. Gall, and et al., Compressive response of NiTi single crystals, Acta Mater., Vol. 48 (2000), pp. 3311-3326.

[67] K. Gall and H.Sehitoglu, The role of texture in tension–compression asymmetry in polycrystalline NiTi, Int. J. Plasticity, Vol. 15 (1999), pp.69-92.

[68] X.G. Ma, K. Komvopoulos, Pseudoelasticity of shape-memory titanium–nickel films subjected to dynamic nanoindentation, Appl. Phys. Lett. Vol. 84(2004), pp. 4274–4276.

[69]W. Yan, Q. Sun, X. Feng, L. Qian, Analysis of spherical indentation of superelastic shape memory alloys, Int. J. Solids and Struct. Vol. 44 (2007), pp. 1–17.

[70] W. Ni, Y.T. Cheng, D.S. Grummon, Microscopic shape memory and superelastic effects under complex loading conditions, Surf. Coat. Tech., Vol. 177-178 (2004), pp. 512-517.

[71] Y.T. Cheng and D.S. Grummon, Micro and nano mechanical testing of materials and devices, Springer US (2008).

[72] Y.T. Cheng1, W. Ni1, Y. Zhang1, and D.S. Grummon, Microscopic shape memory and superelastic effects and their novel tribological applications, IUTAM symposium on Mechanical Behaviour and Micro-Mechanics of Nanostructured Materials, Springer, (2007),pp.211–217.

[73] M. Arciniegas, Y. Gaillard , J. Pen˜a, J.M. Manero, F.J. Gil, Thermoelastic phase transformation in TiNi alloys under cyclic instrumented indentation, IntermetallicsVol. 17 (2009),pp. 784–791.

[74] Y.J. Zhang, Y.T. Cheng, D.S. Grummon, Understanding indentation-induced two-way shape memory effect, Appl. Phys. Lett. Vol. 89 (2006), pp. 04191.

[75] Y. Zhang, Y.T. Chen, D.S. Grummom, Novel tribological systems using shape memory alloys and thin films, Surf. Coat. Tec h.Vol. 202 (2007), pp. 998–1002.

[76] R. Liu and D.Y. Li, Indentation behaviour of pseudoelastic TiNi alloy, Scripta Mater. Vol. 41(1999), pp. 691–696.

[77] A.J. Wood, S. Sanjabi, Y.Q. Fu, Z.H. Barber, T.W. Clyne, Nanoindentation of binary and ternary Ni–Ti-based shape memory alloy thin films, Surf. Coat. Tech. Vol. 202 (2008), pp. 3115–3120.

[78] Y. Zhang , Y.T. Cheng, D.S. Grummon, Indentation stress dependence of the temperature range of microscopic superelastic behaviour of nickel-titanium thin films, J Appl. Phys. Vol. 98 (2005), 033505.

[79] W. Yan, Q. Sun, X.Q. Feng, L. Qian, Analysis of spherical indentation of superelastic shape memory alloys, Int. J Solids Struct. Vol. 44 (2007), pp. 1–17.

[80] W.M. Huang, J.F. Su, M.H. Hong , B. Yang, Pile-up and sink-in in micro-indentation of a NiTi shape-memory alloy, Scripta Mater.Vol. 53 (2005), pp.1055–1057.

[81] H. Z. Ye, R. Liu, D. Y. Li and R. L. Eadie, Wear and friction of a new wear-resistant material: TiNi-based composites. Composites Science and Technology,Vol.617(2001), pp 987-994.

[82] J. Singh, A.T Alpas, Dry sliding wear mechanisms in a Ti50Ni47Fe3 intermetallic alloy. Wear Vol. 181-183 (1995), pp. 302-311.

[83] D.Y. Li, Development of novel tribo composites with TiNi shape memory alloy matrix. Wear, Vol. 255 (2003), pp. 617-628.

[84] D.Y. Li, Wear behaviour of TiNi shape memory alloys, scripta Mater. Vol. 34(1996), pp. 195-200.

[85] H.W. Wang, W.Z. Wu, F.T. Wang, D.Z. Yang, Dry sliding wear of Cu-based shape memory alloy. Acta Metall. Sinica Vol. 27 (1991), pp. A444 -A449.

[86] T. Sasada, M. Oike, N. Emori, The effect of abrasive grain size on the transition between abrasive and adhesive wear, Wear, Vol.97(1984), pp 291-302.

[87] M. Arciniegas , J. Casals, J.M. Manero, J. Pe˜na, F.J. Gil, Study of hardness and wear behaviour of NiTi shape memory alloys, J. Alloy. Compd.Vol. 460 (2008), pp. 213–219.

[88] D.Y. Li, A new type of wear-resistant material: pseudo-elastic TiNi alloy, Wear Vol. 221 (1998), pp. 116–123.

[89] H. Tobushi, H. Iwanaga, H. Tanaka and et al., Stress–strain–temperature relationships of TiNi shape memory alloy suitable for thermo-mechanical cycling, JSME Int. J. Vol. 35 (1992), pp. 271–277.

[90]S. Miyazaki, S.W. Duerig, K. N. Melton, D. Stockel, and C. M. Wayman, Thermal and stress cycling effects and fatigue properties of Ni–Ti alloys, engineering aspects of shape memory alloys, Butterworth–Heinemann, London, (1990), pp. 394 – 413.

[91] S. Miyazaki, T. Imai, Y. Igo, K. Otsuka, Effect of cyclic deformation on the pseudoelasticity characteristics of Ti–Ni alloys, Metall. Trans. A, Vol. 17A (1986), pp. 115–120.

[92] S.K. Wu, H.C. Lin, S.H. Chena, Phenomenological analysis of martensitic transformation in cold-rolled TiNi-base shape memory alloys, Mater ChemPhysVol. 68 (2001), pp. 149–56.

[93] H. Tobushi, Y. Shimeno, T. Hachisuka, K. Tanaka, Influence of strain rate on superelastic properties of TiNi shape memory alloy, Mech Mater Vol. 30 (1998), pp. 141-150.

[94] G.N. Dayananda, M. SubbaRao, Effect of strain rate on properties of superelastic NiTi thin wires, Mater. Sci. Eng. A Vol. 486 (2008), pp. 96-103.

[95] K. L. Johnson, Contact mechanics, (1985), Cambridge University Press.

# Appendix A: Raw Data

Indentation tests results of AISI 304 steel under sharp indenter at room temperature

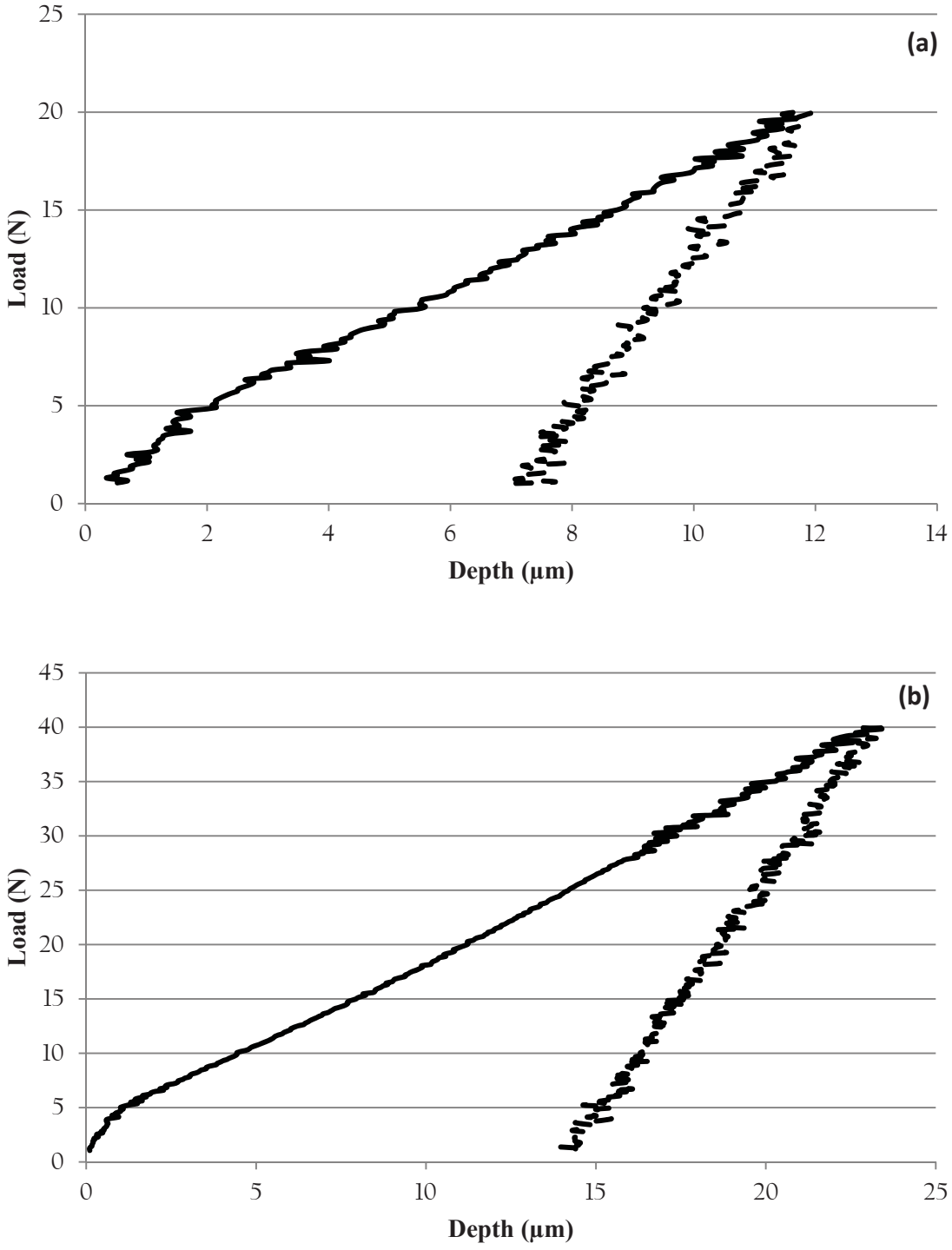


**Figure A.1 - Loading – unloading curves of AISI 304 steel, load application of 1 $N.min^{-1}$ under maximum load of (a) 20 N and (b) 40 N**

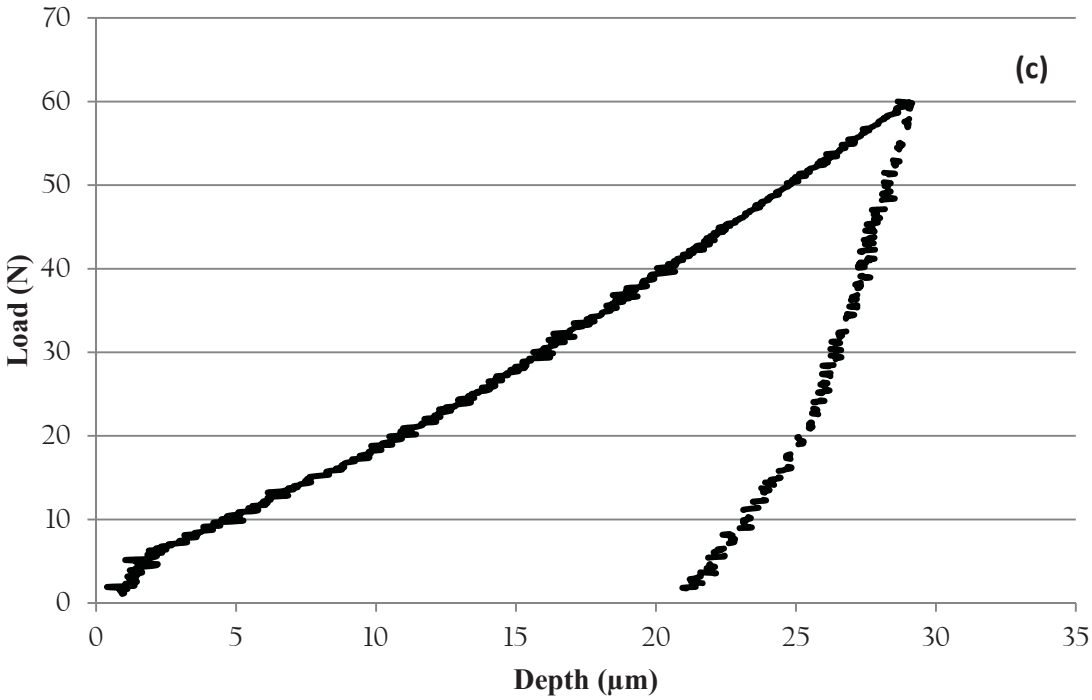


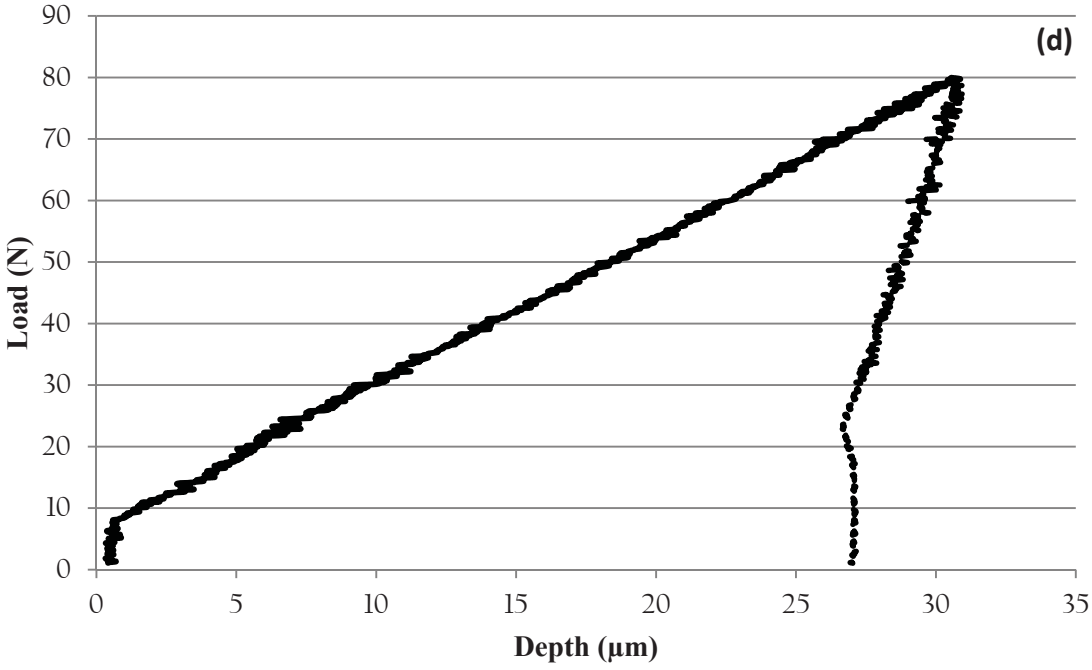


**Figure A.1 - Continued, Loading – unloading curves of AISI 304 steel, load application of 1 N.min$^{-1}$ under maximum load of (c) 60 N and (d) 80 N**

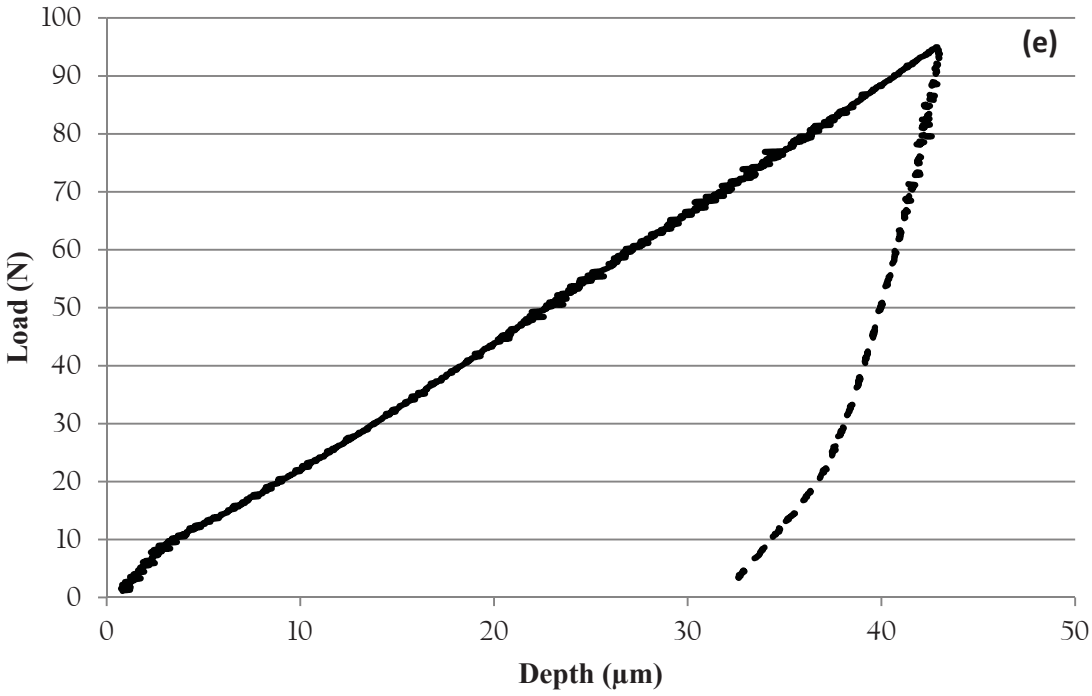


**Figure A.1 - Continued, Loading – unloading curves of AISI 304 steel, load application of 1 N.min$^{-1}$ under maximum load of (e) 100 N**

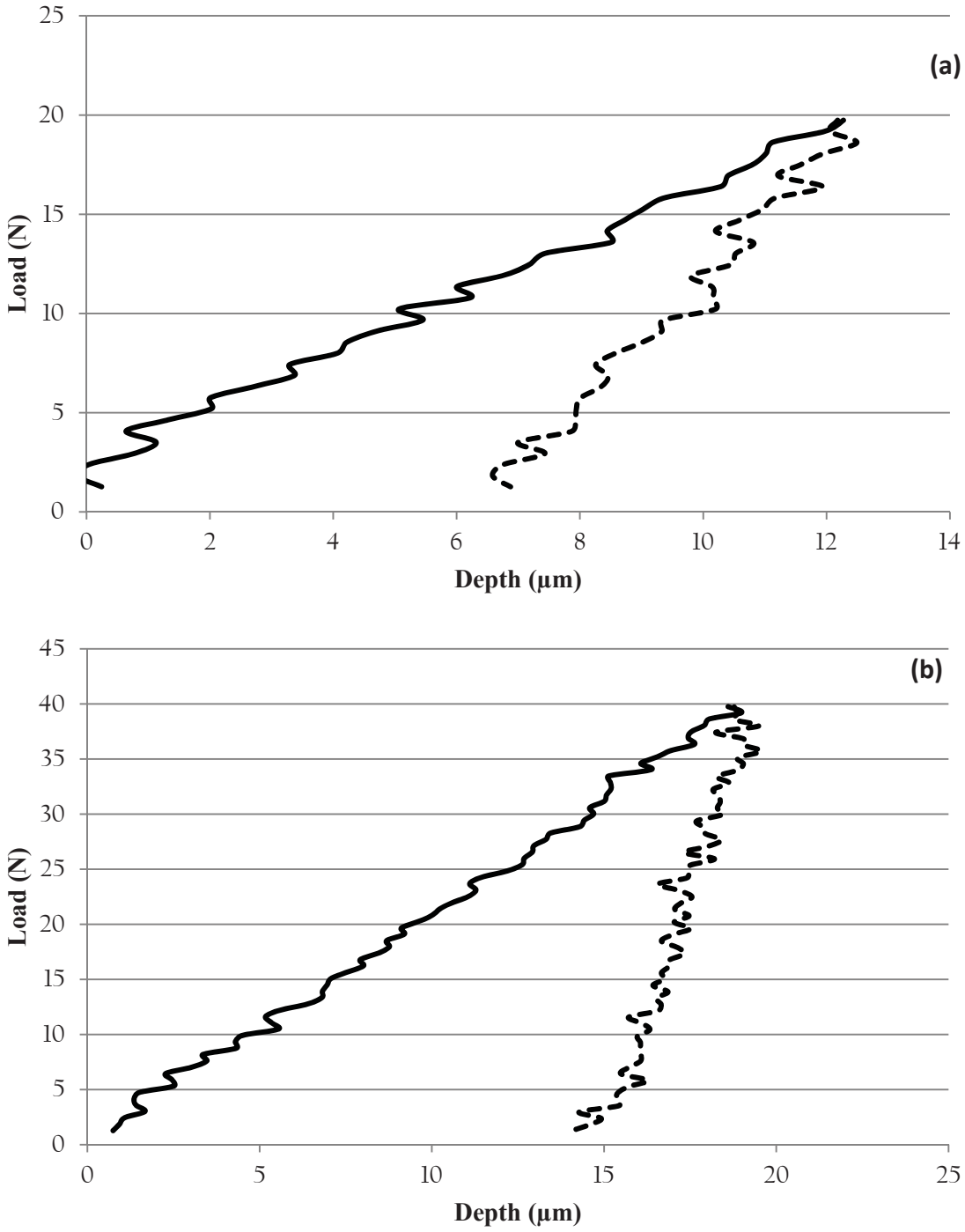


**Figure A.2 - Loading – unloading curves of AISI 304 steel, load application of 10 $N.min^{-1}$ under maximum load of (a) 20 N and (b) 40 N**

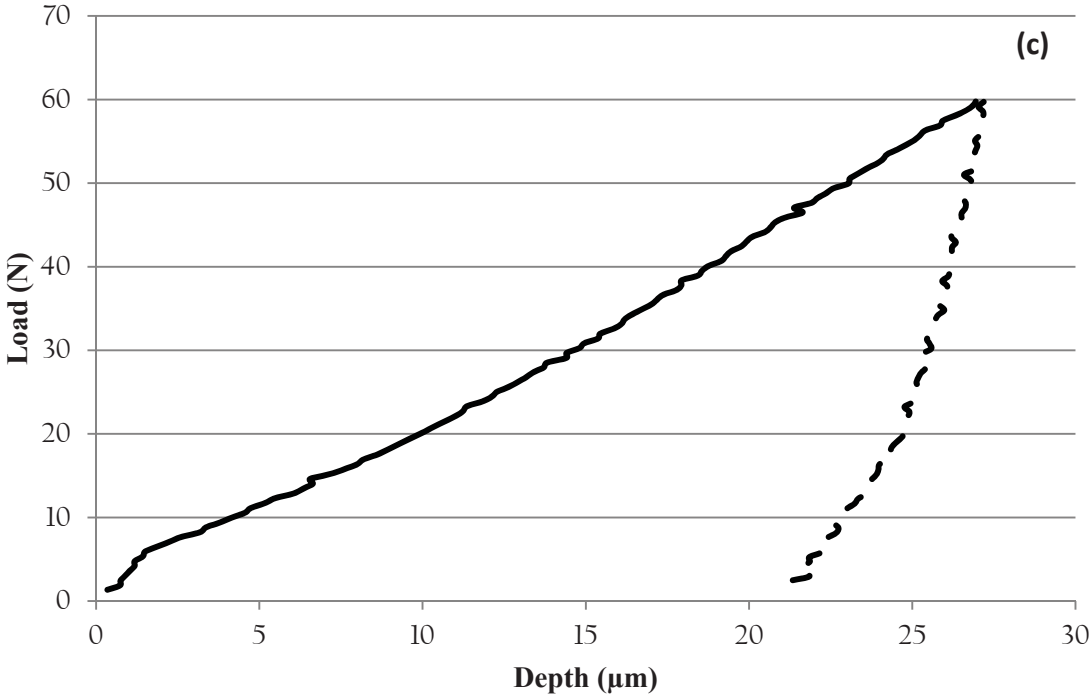


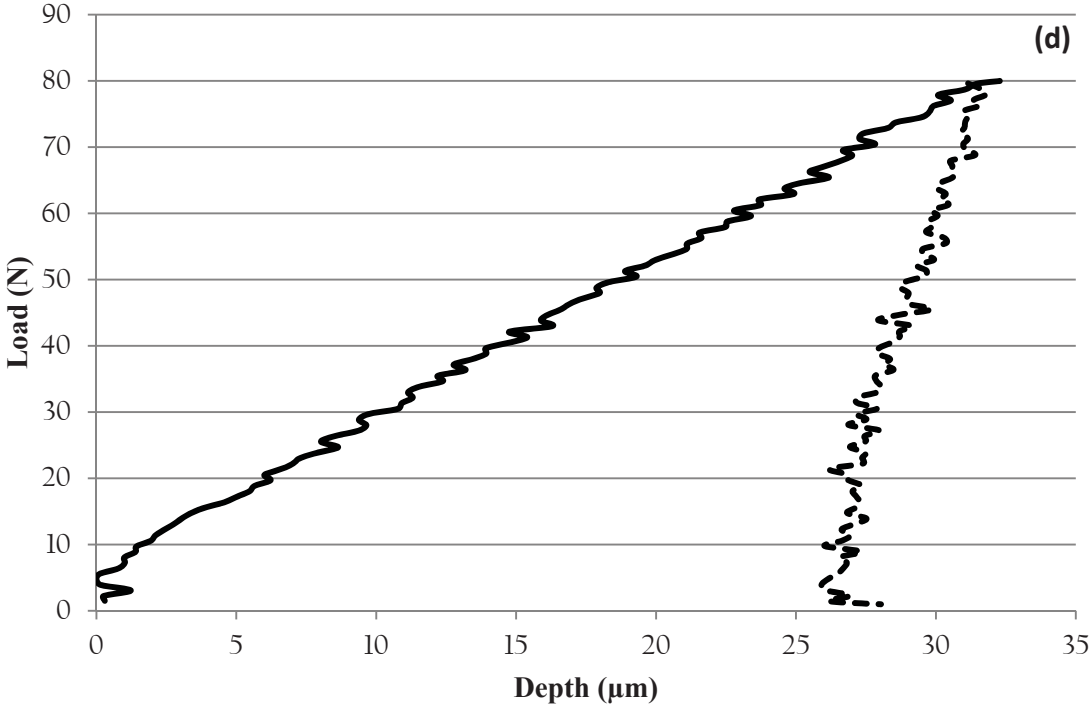


**Figure A.2 - Continued, Loading – unloading curves of AISI 304 steel, load application of 10 N.min$^{-1}$ under maximum load of (c) 60 N and (d) 80 N**

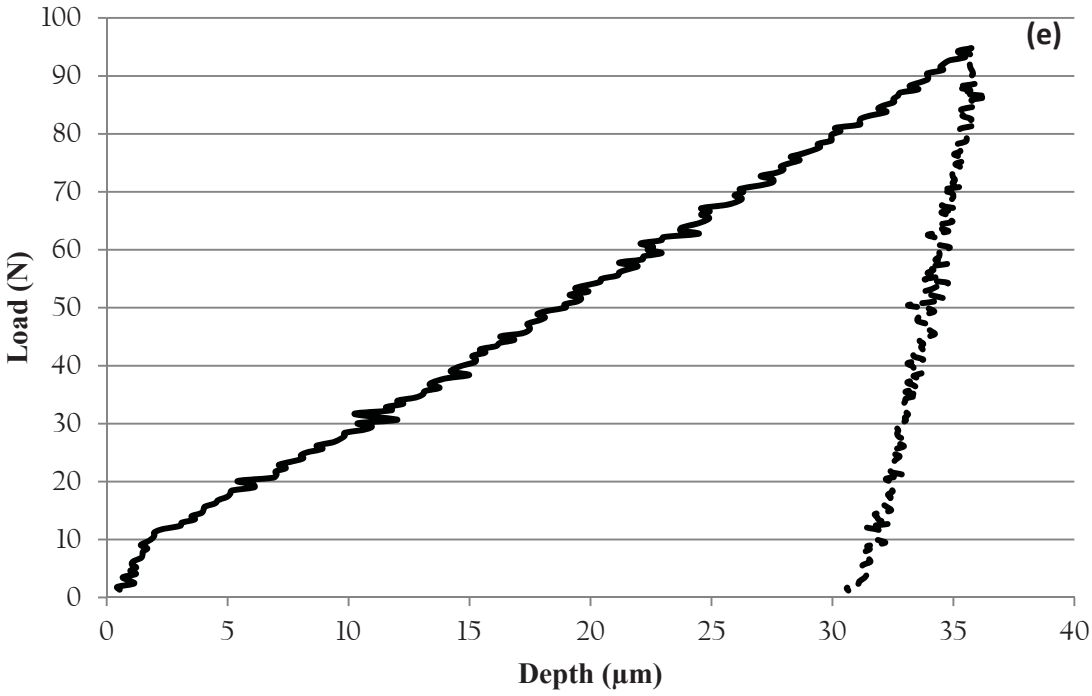


**Figure A.2 - Continued, Loading – unloading curves of AISI 304 steel, load application of 10 N.min$^{-1}$ under maximum load of (e) 100 N**

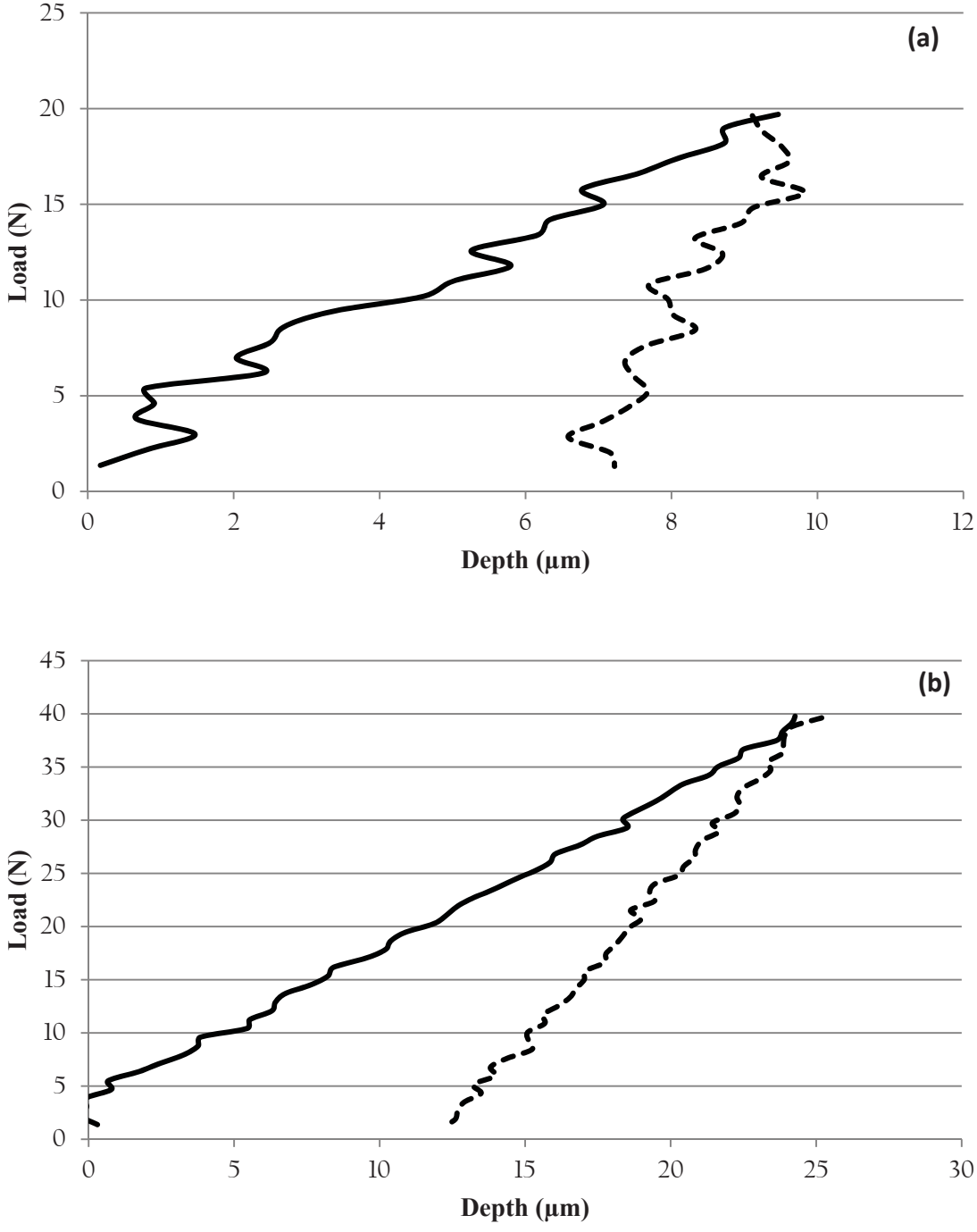


**Figure A.3 - Loading – unloading curves of AISI 304 steel, load application of 20 $N.min^{-1}$ under maximum load of (a) 20 N and (b) 40 N**

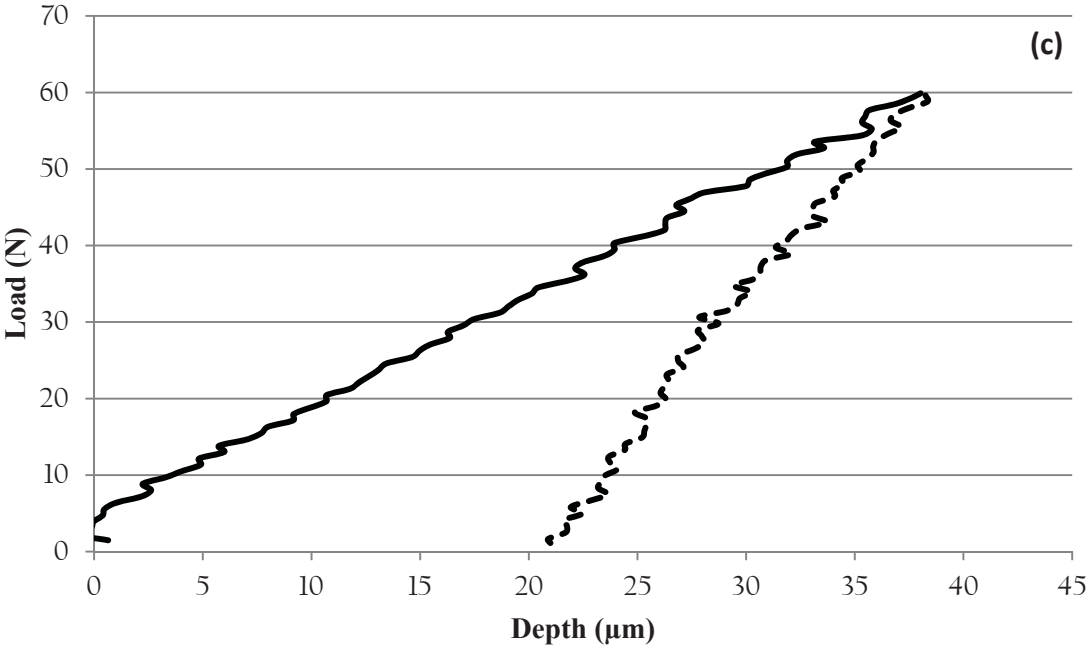


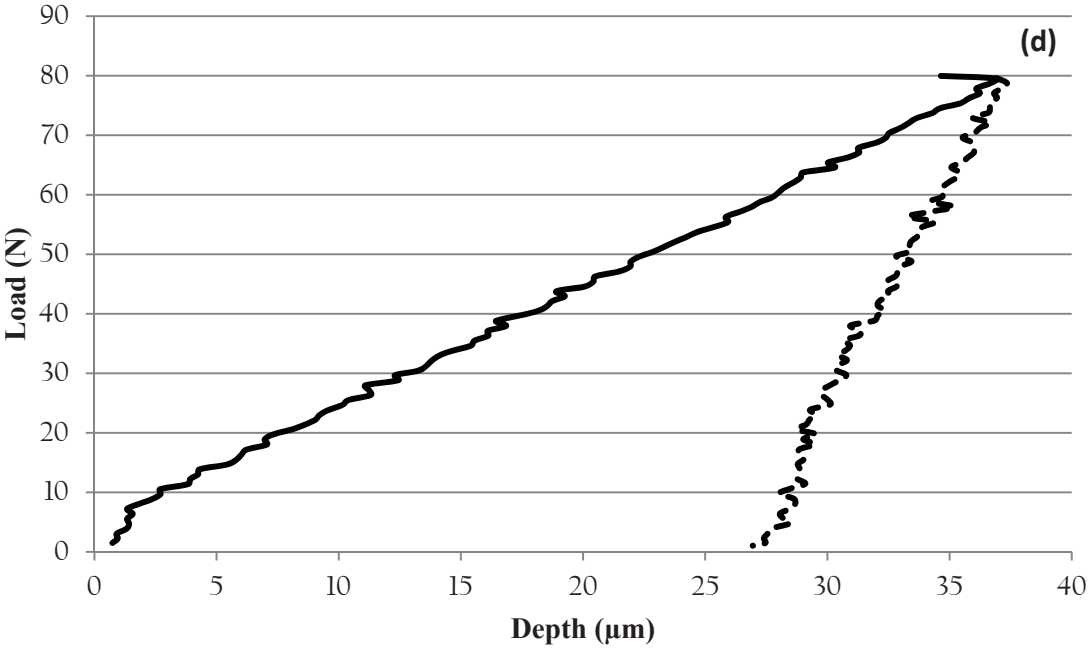


**Figure A.3 - Continued, Loading – unloading curves of AISI 304 steel, load application of 20 N.min$^{-1}$ under maximum load of (c) 60 N and (d) 80 N**

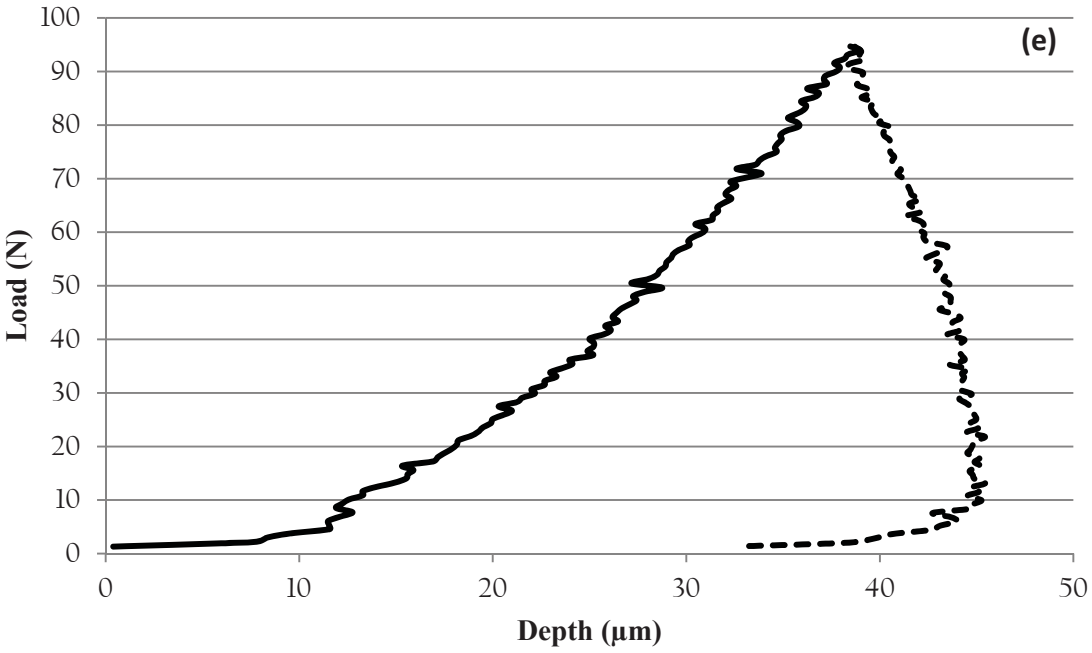


**Figure A.3 - Continued, Loading – unloading curves of AISI 304 steel, load application of 20 N.min$^{-1}$ under maximum load of (e) 100 N**